

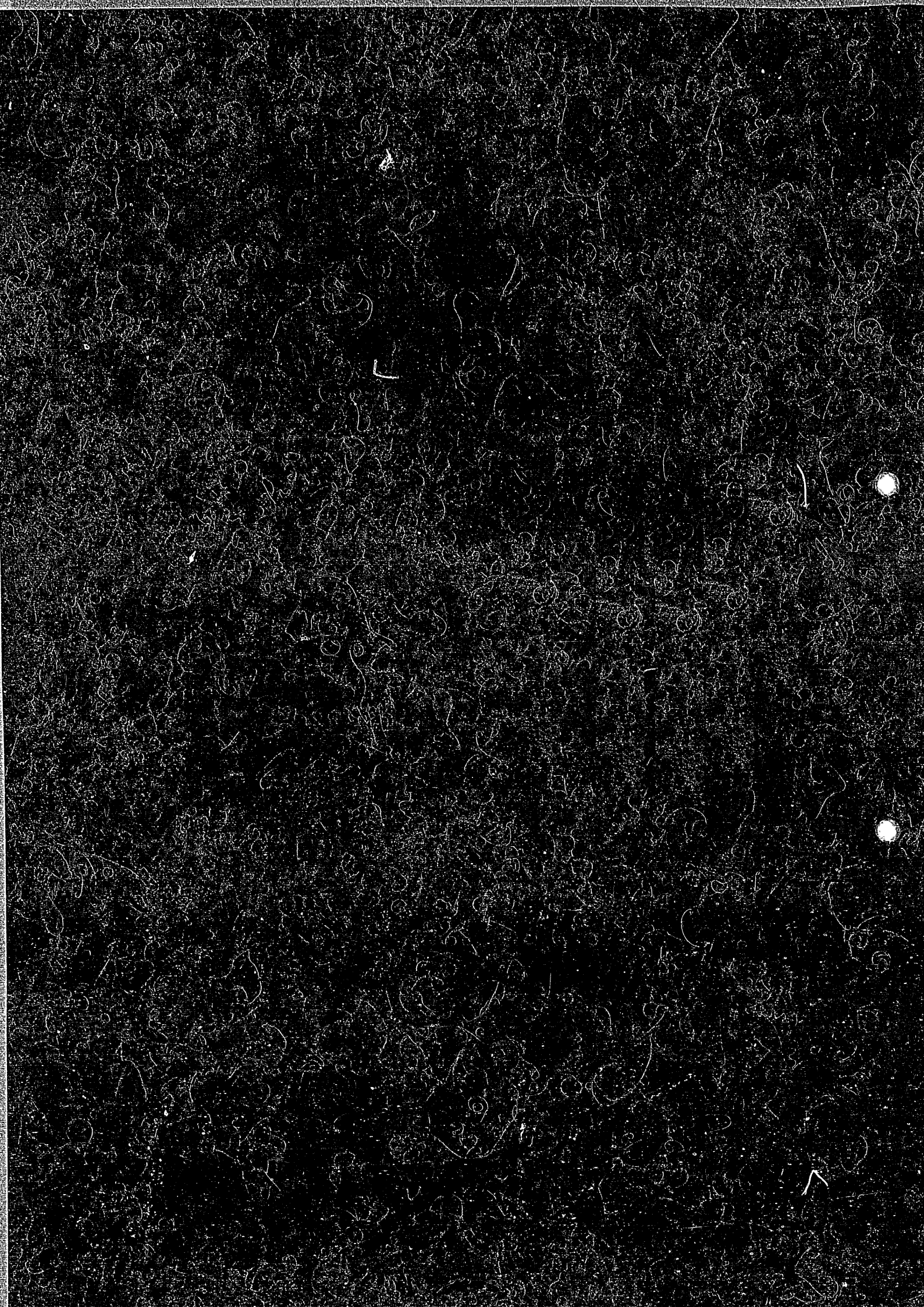
IPPJ-AM-53

DATA BASE ON THE HIGH HEAT FLUX BEHAVIOUR OF METALS
AND CARBON MATERIALS FOR PLASMA FACING COMPONENTS
EXPERIMENTS AT THE 10 MW NEUTRAL BEAM INJECTION
TEST STAND OF THE IPP NAGOYA

H.BOLT, C.D.GROSSMANN, A.MIYAHARA
T.KURODA AND Y.OKA

INSTITUTE OF PLASMA PHYSICS
NAGOYA UNIVERSITY

NAGOYA, JAPAN



**DATA BASE ON THE HIGH HEAT FLUX BEHAVIOUR OF METALS
AND CARBON MATERIALS FOR PLASMA FACING COMPONENTS
– EXPERIMENTS AT THE 10 MW NEUTRAL BEAM INJECTION
TEST STAND OF THE IPP NAGOYA**

H. Bolt¹⁾, C. D. Croessmann²⁾, A. Miyahara, T. Kuroda and Y. Oka

Institute of Plasma Physics, Nagoya University
Chikusa-ku, Nagoya 464, Japan

August 1987

- 1) on leave from Institute of Reactor Materials, Nuclear Research Center,
Juelich, FRG, Association EURATOM – KFA
- 2) Sandia National Laboratories Albuquerque, NM, USA

This document is prepared as a preprint of compilation of atomic data for fusion research sponsored fully or partly by the IPP/Nagoya University. This is intended for future publication in a journal or will be included in a data book after some evaluations or rearrangements of its contents. This document should not be referred without the agreement of the authors. Enquiries about copyright and reproduction should be addressed to Research Information Center, IPP/Nagoya University, Nagoya, Japan.

Abstract

Disruption events in tokamak devices are regarded as one of the main issues governing material and design considerations for in-vessel components. During disruptions heat loads in the order of 100 to 5000 MW/m^2 for durations of about 100 μs to several ten ms can cause severe damage to plasma facing components and possibly may lead to their failure.

To determine the response of materials to high heat fluxes an experimental program was carried out on metals and carbon materials using the 10 MW Neutral Beam Injection Test Stand of the IPP Nagoya. Stainless steel, aluminium, copper, and molybdenum samples, 13 grades of fine grain graphites, and pyrolytic carbon samples were subjected to hydrogen beam exposure with power densities of 15 to 120 MW/m^2 and pulse durations of 50 to 950 ms. Resulting damage and threshold values for the occurrence of damage were determined and documented. Main damage observed on samples are melting, erosion, and crack formation. The high heat flux resistance of the materials tested is compared comprehensively with each other. Processes leading to material damage are discussed and in the case of damage on graphite models of erosion and cracking processes are given. The implication of the experimental results for material selection and design of first wall components under the high heat flux aspect is discussed.

Contents

1.	Introduction	1
2.	Tokamak disruptions and disruption damage on first wall components	3
3.	High heat flux experiments	4
3.1	Requirements for high heat flux experiments	4
3.2	Operation of the 10 MW Neutral Beam Injection Test Stand for Material Experiments.....	6
4.	Response of metals to high heat fluxes	7
4.1	Present state of experimental research on the high heat flux behaviour of metals	7
4.2	High heat flux experiments on metals	10
4.2.1	Materials selection and experimental procedure	10
4.2.2	Results of the experiments on metals	12
4.3	Discussion of the experimental results on metals.....	14
5.	Response of graphites to high heat fluxes	21
5.1	Present state of experimental research on the high heat flux behaviour of graphites	21
5.2	Experiments on graphite	23
5.2.1	Materials selection and experimental procedure	23
5.2.2	Results of the comparative experiments on graphite materials ...	25
5.2.3	Behaviour of graphite materials under stress concentration	32
5.3	Discussion of the experimental results on graphites	35
5.3.1	Erosion	35
5.3.2	Cracking	38
6.	Response of pyrolytic carbon and brazed pyrolytic carbon - copper compounds to high heat fluxes	45
7.	Implication of the experimental results for the application of first wall materials and components	50
8.	Summary	55

1. Introduction

In present day tokamak experiments the plasma operation frequently is terminated by disruptions. During such a disruption the energy content of the plasma is deposited on the first wall which directly faces the plasma. Under these off-normal conditions components of the first wall are subjected to heat loads which can exceed the normal operation heat loads by several orders of magnitude. The short duration of such events in the order of milliseconds causes extremely rapid heating of such components, and as a result of this temperature excursion, deformation, melting, vaporization, cracking and other damage can occur. Depending on the kind and degree of damage caused by a disruption components may fail which can severely influence the further operation of the entire fusion device.

As a full controllability of disruption events during tokamak operation appears to be impossible in -at least- a mid-term time scale also first wall structures of next generation devices have to be designed to withstand disruption heat loads.

For an understanding of the high heat flux behaviour of candidate materials for first wall components of fusion devices which presently are in operation and those which are under construction or being planned laboratory high heat flux experiments have to be carried out. From an understanding of the underlying failure processes and a comparison of the heat flux stability of material candidates guidelines for material selection and component design can be derived which better cope with the disruption issue.

In the following study a broad range of metal and carbon materials were subjected to high heat fluxes and their structural response to the resulting temperature excursions was determined. Special emphasis has been given to the testing of graphite materials as graphite components are presently installed in by far the most of the present day tokamak devices and graphite is regarded as prime candidate for the "Compact Ignition Tokamak (CIT)" as well as for the next generation projects like the "Next European Torus (NET)" or the "Fusion Experimental Reactor (FER)" /1/. Carbon - carbon composite materials (C-C composites) which are now subject of rising interest because of their high thermal shock stability have also been tested. The results on these materials have been documented previously /2/.

The device used for the high heat flux experiments has been the 10 MW Neutral Beam Injection Test Stand of the IPP Nagoya. Material samples were exposed to hydrogen beam pulses of high power density and very homogeneous distribution of the heat flux over the sample surface.

The objectives of this study are:

- To determine damage and damage thresholds of materials under high heat fluxes.
- To better understand the underlying processes which lead to damage and failure of materials under high heat fluxes.
- To derive and to recommend consequences and guidelines for the application of these materials as in-vessel components.

2. Tokamak disruptions and disruption damage on first wall components

According to the literature /3-5/ the occurrence of disruptions can be explained by the magnetohydrodynamic (MHD) theory as follows:

Disruptions in tokamaks are being developed, when the plasma column is near the threshold of MHD-stability. Under this condition any inaccurate handling of the plasma can cause a disruption. This may happen e.g. by non-optimized fuelling, an increase of the impurity influx, additional power input by neutral beam injection or radiofrequency heating of the plasma, or an excess of the density limits of the plasma. In these cases magnetic islands within the plasma grow and eventually overlap, the magnetic field lines become ergodic, and rapid energy and particle transport along these ergodic field lines in radial direction of the plasma column occurs. Thus the plasma rapidly expands radially and as a result large fluxes of plasma particles are dumped onto first wall components, mainly the protruding ones. This thermal quench of the plasma energy occurs within a very short time, between 20 and 200 μ s in most present day devices /6,7/ and an expected 1 to 2 ms for next generation devices /8,9/. Following this thermal quench the decay of the magnetic energy lasts longer, in the order of less than 1 ms to about 40 ms /10,11/.

During the course of a disruption components of the first wall, especially the ones which are most protruding into the plasma on the inboard side of the vessel, are subjected to severe heat fluxes. Table 1 lists conditions of severe disruptions in present day devices and those anticipated for future devices together with the peak heat fluxes to which first wall components are subjected /12/.

The resulting damage to first wall components from disruptions in operating tokamaks is documented in /13-17/ for stainless steel limiters in FT, PLT, ISX-A, and TEXTOR. Damage observed is deformation, surface melting, splashing of metal and by this partial loss of the melt layer, crack formation in the resolidified melt, roughening of the surface in resolidified areas, and depletion of alloy constituents due to preferential evaporation. Several TiC-coated molybdenum tiles in JT-60 suffered melting which is attributed to disruption heat fluxes /11,18/. Tiles of the TiC-coated graphite limiter in Doublet III suffered cracking and fracture under the incident heat fluxes /19-21/. Also from TFTR damage and failure of graphite tiles due to disruptions is reported /22/. Until now no damage on graphite tiles that could be attributed to disruptions is found in JET /23,24/.

3. High heat flux experiments

3.1 Requirements for high heat flux experiments

In order to gain knowledge on the behaviour of first wall materials and components under disruption conditions laboratory tests in which materials are subjected to high heat fluxes have to be carried out. For a most realistic approach to this aim devices for high heat flux experiments should fulfill the following requirements:

- High power densities have to be provided (at least several ten MW/m^2).
- Short pulses have to be possible which means that the rise time of the power density has to be short.

- A homogeneous distribution of the power density over large areas (several 10 cm^2) is important to avoid size effects by using large size samples and full size first wall components.
- The energy should be deposited in a very thin surface layer for a realistic simulation of surface heat loads ($10 \text{ }\mu\text{m}$ or less).
- The heat flux exposure should take place in vacuum.

Table 2 lists major devices together with their main machine parameters which are used or intended to be used for high heat flux experiments on fusion candidate materials /1,25,26/. Most of the devices are electron beam facilities which have the advantage of high availability and uncomplicated operation. The main disadvantages of electron beam test stands are the limitation of the power output and the electron beam characteristics. This means that due to the small diameter of the electron beam the power density distribution is very inhomogeneous. For the application of surface heat loads on larger areas the electron beam has to be scanned with very high frequencies to avoid transient heating phenomena caused by the moving beam. However even then the limited power of electron beam devices can produce high heat loads only on surfaces of a few cm^2 .

The applicability of lasers for high heat flux experiments is restricted because of their limited power which allows only the irradiation of small areas and uncertainties in beam - surface interactions.

The principle in the use of Neutral Beam Injection Test Stands for high heat flux experiments is to expose material samples to a beam which consists of hydrogen atoms and ions of high kinetic energy. These test

stands have the advantages of high power densities and a very broad distribution of the power density within the beam. Thus large sample surfaces or even full size first wall components can be subjected to heat loads. The disadvantage in the use of Neutral Beam Injection Test Stands lies in their complicated operation, because much machine time is consumed for conditioning before and during the experiments.

3.2 Operation of the 10 MW Neutral Beam Injection Test Stand for Materials Experiments

A detailed description of the test stand operation and the beam calibration procedure has been given in a previous publication [2]. For the performance of high heat flux experiments on candidate first wall materials and full size first wall components the 10 MW Neutral Beam Injection Test Stand at the IPP Nagoya [27-29] had been modified. Figure 1 gives a schematic of the test stand. A lock system with drive mechanism mounted on top of the test stand allows the insertion of test pieces into the test stand vessel for beam exposure without breaking the vacuum of the vessel (about 10^{-4} Pa) (Fig. 2).

The ion source of the test stand produces hydrogen beams of up to 120 keV, 75 A and 1 s pulse duration with a gaussian shaped profile of the beam power density. The elongation factor of the oval shaped beam in vertical direction is roughly 2 and depends on the beam condition applied in experiments. For material tests the deflection coils of the Neutral Beam Test Stand are not in operation thus ions and neutrals are striking the material test pieces at a distance of about 5 m from the ion source. The repetition rate of the test stand is three to five minutes depending on the power supply mode. When operated without

exposing test pieces to the beam, the beam is dumped into a calorimeter which provides data for the calibration of high heat flux experiments.

After the beam conditions for high heat flux experiments - as indicated by the calorimeter values - were satisfied, the test pieces were positioned in the beam line so that during the next pulse the beam could hit the samples with beam conditions similar to the previously calibrated pulse onto the calorimeter and a variation of the beam power of less than 5%. Figure 3 gives a calibration curve of the beam power density distribution of a pulse as it has been applied in the experiments.

4. Response of metals to high heat fluxes

4.1 Present state of experimental research on the high heat flux behaviour of metals

Compared to other candidate first wall materials detailed research on the high heat flux behaviour of metals has been undertaken in a large number of studies. In most of these studies electron beam facilities with electron energies of 5 keV to 150 keV were used for the experiments /17,25,26,30-54/. The irradiation times in these experiments varied from 0.5 ms /45/ to a few s /53,54/. The samples were either irradiated with a stationary beam which was focussed in order to obtain high power densities or defocussed for the irradiation of a larger sample area (in the order of 1 cm dia.), or with a scanned focussed electron beam allowing the irradiation of larger areas (in the order of 1 to 10 cm²)

with homogeneous heat loads. For this last mode of operation very high scan speeds are necessary to avoid transient heating phenomena caused by the focussed electron beam. Other studies on metals use hydrogen beams with energies and power densities of 26 keV, 43 MW/m² /55/, 30 keV, 20 MW/m² /56-60/, and 120 keV, 100 MW/m² /61-63/. With regard to the materials tested, a broad range of metals, ceramics, and carbon materials is compared in /17,32,33,37-39/.

By far most of the investigations were performed on various grades of stainless steel and Ni-base alloys. Detailed studies on these materials are documented in /25,30,31,34,36,41-45,47-49,51/. Structural changes of stainless steel below the melting threshold are twin formation (slip) and grain growth /34,36,45/. Melting thresholds were determined for characteristic irradiation times and power densities /25,34,36-38,41-43, 45,47-49/. The experimental thresholds for melting are in fair agreement with thresholds calculated from physical properties data by way of one- or two dimensional calculations /25,34,41-43,48,49/. Above this threshold melt layer formation, vaporization of metal, preferential evaporation of alloy constituents and the formation of cracks are observed. Studies treating these effects quantitatively are /25,30,31, 34,36,41-44,47-50/. It is found that the melt depth under high heat flux impact tends to exceed the theoretically calculated values. The detected weight losses due to vaporization are explained by various theoretical models including vapor shielding effects or enhanced vaporization from the melted phase. Studies which include metallographic examinations of the irradiated samples report the occurrence of hot-cracks in the resolidified melt layer /17,30,31,34,45-47/.

Among other metals major work was performed on refractory metals frequently with emphasis laid on molybdenum /26,30,34,35,37,38,40-43,48, 52-58,61,62/. Detailed comparisons between different refractory metals with respect to melting thresholds, vaporization losses, and cracking were performed by /34,35,40,43/. Advantages of refractory metals like a high melting threshold compared to stainless steel and lower vapor pressures which lead to reduced vaporization losses than for stainless steel are met by unfavourable crack behaviour, especially with materials passing the ductile brittle transformation temperature (DBTT) in the experiments. Molybdenum as a material candidate received particular attention in several experimental studies related to the JT-60 tokamak project where until recently molybdenum with a thin TiC coating was applied as first wall material /26,52-54,56-58/. Several of these studies were performed on coated molybdenum (mainly with TiC) where failure of the samples under high heat fluxes usually occurred as a failure of the substrate by melting.

Studies on copper under high heat flux impact are included in /25,30,37, 38,42,43,48/. The very high thermal conductivity of this material causes high thresholds of power density and heat flux duration despite the low melting point of copper. Resolidified zones of samples heated above the threshold for melting do not show any cracks.

Aluminium has also been investigated in several studies /25,30,41,43, 49/. Thresholds for melting of Al were observed to be comparable to those of stainless steel with respect to power density and heat flux duration.

4.2 High heat flux experiments on metals

4.2.1 Materials selection and experimental procedure

The behaviour of metals under high heat fluxes was tested on stainless steel, aluminium, copper, and molybdenum. Stainless steel alloys used in the experiments were 1.4311 (CRONIFER 1810) with a composition of 10% Ni, 18% Cr, 0.03% C, 1% Si, 2% Mn, 0.2% N, bal. Fe and SUS 304 with a composition of 10% Ni, 18% Cr, 0.08% C, 1% Si, 2% Mn, bal. Fe /64,65/.

Stainless steel was selected for the experiments because most of the existing tokamaks are built with stainless steel or nickel-base alloy walls or liners and still in these tokamaks major portions of the plasma facing wall consist of these alloys. As in a previous study /34/ no significant difference in the high heat flux behaviour between stainless steel 1.4311 and the nickel-base alloy INCONEL 600 has been found, stainless steel was selected for the experiments. Aluminium has been chosen because the low activation properties under neutron irradiation made it an attractive material for short pulse reacting plasma device concepts /66-70/. The high thermal conductivity of copper and the excellent performance as high heat flux material for beam dump structures /71,72/ were reasons for the selection of this material. As molybdenum is one of the candidate materials for collector plates of divertors in future devices and as it has been applied as plasma facing material e.g. in JT-60 and Doublet IIa /73/, also this material has been subjected to high heat flux experiments.

For the attachment of the samples to a 15 mm thick copper backing plate

which served as sample holder threaded holes of small depth were machined into the back side of the samples. The samples then could be fixed to the sample holder by bolts.

A number of initial experiments on stainless steel were performed on large targets consisting of several stainless steel pieces with a surface area of 50 mm x 50 mm each (Figs. 4, 5). All other experiments on metals were carried out with smaller samples of 30 mm x 30 mm surface area and 10 mm thickness as no difference in the structural response of the materials to high heat fluxes between large size and small size samples was detected. The surfaces which were to be exposed to the heat flux were ground and the samples cleaned by alcohol in an ultrasonic bath before the experiments. In general two types of experiments were performed on metal materials:

- For the detection of melting thresholds a sample was subjected to subsequent pulses of rising power density at a preset pulse length. After each pulse the sample surface was checked visually for the occurrence of melting. Before the next experiment the sample was allowed to cool down to a temperature below 100⁰C (measured by thermocouple in a part of the experiments). One experiment on molybdenum was carried out on a sample with elevated temperature which lead to a reduced melting threshold in terms of power density (no. 20, Table 3). Once initial melting on the sample surface occurred, the sample was exchanged.

- In order to determine the development and behaviour of the melt layer under homogeneous heat fluxes on large areas, experiments were carried

out with heat fluxes well above the melting thresholds of the materials.

4.2.2 Results of the experiments on metals

A list of the experiments and experimental parameters is given in Table 3. The experimental results are summarized in Table 4.

Stainless steel (Fig. 4 - 7): Stainless steel samples were irradiated with pulse lengths from 50 ms to 951 ms (see Table 3). A number of experiments has been carried out with large targets of 1.4311 (Table 3, no. 1 - 4, Figs. 4, 5).

Figure 4 gives an example where initial melting on a small spot of about 15 mm diameter occurred under a short pulse of 50 ms duration. At longer pulse lengths (e.g. 951 ms, Fig. 5) very small variations in the power density can already result in significant changes of the surface structure by melting large amounts of material.

The structure of the melt layer is similar on all tested stainless steel samples. Even during initial melting the melt immediately contracts to form a ripple structure on the surface before resolidifying again (Fig. 4). More clearly this effect can be found on samples where the melt layer had more time to undergo structural changes before resolidifying (Fig. 5). Figure 6 shows a crater-like depression in the melt layer of a sample which was caused by melt layer motion. This effect of ripple formation is frequently reported to occur on the surface of stainless steel first wall components, especially limiters, which underwent severe thermal excursions during disruptions /13-16,31/.

In the resolidified melt zones cracks were observed on all samples (e.g. Fig. 7 a and b). Cracks propagate intergranular through the dendritic structure of the resolidified melt and frequently expand over the whole depth of the melt zone sometimes penetrating into the not-melted base material for lengths of a few grains. A quantitative evaluation of the cracking on stainless steel 1.4311 and INCONEL 600 materials is documented in /34/.

Aluminium (Figs. 8, 9): Above the threshold for melting a homogeneous and smooth melt layer formed on all aluminium samples (e.g. Fig. 8 a). Obviously by the surface tension due to temperature gradients of the melt only weak force is exerted on the liquid so that no formation of ripples occurs. The resolidified surface shows many cracks which have a strong similarity to those observed on stainless steel (Figs. 8 b, c, 9). On the surfaces large numbers of "hole-like" voids of 10 to 20 μm diameter are found which are supposed to have been formed by gaseous inclusions in the melted material (Fig. 8 c).

Copper (Fig. 10): Compared to stainless steel and aluminium which have similar melting thresholds, the threshold for copper is far higher as a result of the high thermal conductivity of this material. Similar to the behaviour of the melted layers on aluminium copper shows no sign of melt movement so that the surfaces of all tested samples have a smooth appearance (e.g. Fig. 10 a). Also under high magnification the resolidified surfaces appear very homogeneous (Fig. 10 b). No cracks could be detected on the copper samples.

Molybdenum (Fig. 11): As a result of the high melting point of

molybdenum (2620°C) this material has a very high melting threshold. The melt layer appearance on the samples is similar to that on stainless steel with the formation of a rippled surface structure due to strong forces caused by gradients of the surface tension in the melt layer. Figure 11 b shows a depression of the surface in an area where the melt was partially removed. The resolidified melt (Fig. 11 c) is of coarse grain structure. In some areas the melt was completely removed leaving the base material bare to the surface (Fig. 11 d). The melt removed from the area of the depression (upper half, left side, Fig. 11 d) resolidified by forming a coarse grain structure (lower half, right side of Fig. 11 d). On the samples no cracks were observed after the experiments. This result is consistent with the results of other studies using broad hydrogen beams for the irradiation of molybdenum samples where no crack occurrence was observed /56-58/. In the frame of an experimental study using a stationary electron beam crack formation was detected on molybdenum /34/. The cracks were initiated in the heat affected area and propagated far into the unaffected material. It is assumed that these cracks are mainly a result of stress concentration which occurs during the heating of a comparatively small spot on the otherwise cold sample surface as under homogeneous heating conditions by broad hydrogen beams this damage has not been observed.

4.3 Discussion of the experimental results on metals

The results of the experiments on melting thresholds of metals are given in Figure 12. This figure compares thresholds which were determined analytically with the experimental data. The analytical thresholds were determined using the following equations /74-77/:

The basic differential equation for heat conduction in solid materials is given as:

$$\frac{\partial}{\partial x} \left(k \frac{\partial T}{\partial x} \right) + \frac{\partial}{\partial y} \left(k \frac{\partial T}{\partial y} \right) + \frac{\partial}{\partial z} \left(k \frac{\partial T}{\partial z} \right) + F_o - \rho c \frac{\partial T}{\partial t} = 0 \quad (1)$$

with T: temperature
k: thermal conductivity
 F_o : heat flux
 ρ : density
c: specific heat
t: time
x,y,z: spatial coordinates

A solution of eq. (1) introducing boundary conditions yields the temperature $T(x, y, z, t)$ of a material under a surface heat load $F_o(x = f(y, z), t)$ during the time t. Under assumptions of a semi-infinite solid and a one-dimensional geometry with a constant heat flux P/A on the surface $x = 0$ and the starting temperature $T(x, t) = T(0, 0)$, eq. (1) can be rewritten as

$$\frac{\partial^2 T(x, t)}{\partial x^2} + \frac{P}{Ak} - \frac{\rho c}{k} \frac{\partial T(x, t)}{\partial t} = 0 \quad (2)$$

with: P/A : heat load per unit area

Neglecting energy losses by radiation and evaporation eq. (2) can be solved to:

$$T_{(x,t)} = T_{(0,0)} + F_0 \sqrt{t} \frac{2}{\sqrt{\pi \rho c k}} \left\{ e^{-[(x/2 \sqrt{t}) \sqrt{\rho c/k}]^2} - 2 (x/2 \sqrt{t}) \sqrt{\rho c/k} \int_{(x/2 \sqrt{t}) \sqrt{\rho c/k}}^{\infty} e^{-\zeta^2} d\zeta \right\} \quad (3)$$

Thus for the surface temperature $T(0, t)$ eq. (3) simplifies to

$$T_{(0,t)} = T_{(0,0)} + \frac{P}{A} \sqrt{t} \frac{2}{\sqrt{\pi \rho c k}} \quad (4)$$

With eq. (4) the theoretical melting threshold for a heat flux P/A_T at a given pulse duration t is given as

$$\frac{P}{A_T} = (T_M - T_{(0,0)}) \frac{\sqrt{\pi \rho c k}}{2\sqrt{t}} \quad (5)$$

with: T_M : melting temperature of the material

Eq. (5) can be used for an evaluation of the high heat flux experiments when the following requirements are satisfied:

- The distribution of the power density has to be very homogeneous over the sample surface to allow the assumption of one-dimensional heat conduction. The broad power density distribution of the hydrogen beam used in the experiments (Fig. 3) provides a very homogeneous heat flux over a sample surface of 30 mm x 30 mm.
- The pulse length t of the heat flux has to be shorter than the thermal

diffusion time which is a function of the sample thickness d :

$$t < \frac{d^2 \rho c_p}{4k} \quad (6)$$

When calculated with material properties at room temperature /78-81/ the maximum pulse length on a sample of 10 mm thickness is 0.74 s for copper, 0.76 s for aluminium, 1.51 s for molybdenum, and 24.3 s for stainless steel. The pulse lengths throughout the experiments were shorter than these limits (see Table 3). In this calculation the room temperature properties of materials were used as the thermal diffusion time is independent of the heat load.

- As the thermal properties of the tested materials are temperature dependent, for a calculation of the melting threshold average values over the temperature range occurring have to be used. With this method errors in the heat flux threshold for initial melting can be kept below 20 % /82,83/.

Figure 12 shows that thresholds calculated in this way and experimental thresholds are in fair agreement with each other within the error margin of 20 % for the analytical solution and an assumed error margin of 10 % for the calibration of the beam power density. Only one experimental value on molybdenum considerably deviates from the analytical threshold. In this case the experiment was carried out on a pre-heated sample of uncertain initial temperature (cf. 4.2.1).

A comparison of the heat flux resistance of the tested metals (Fig. 12)

shows that the sensitivity of aluminium and stainless steel to high heat fluxes is very similar with each other. In the case of aluminium the low melting point and in the case of stainless steel the low thermal conductivity cause early melting under moderate heat fluxes. The high thermal conductivity of copper leads to a melting threshold which exceeds those of aluminium and stainless steel by a factor of about 2.5. The threshold of molybdenum is slightly higher than that of copper due to the very high melting point of this material.

Especially on stainless steel and aluminium, the materials with a comparatively low tolerance to high heat fluxes, heat loads exceeding the melting threshold have to be avoided as cracks which occur in the resolidified areas may deeply propagate into the unaffected material under cyclic stresses to which first wall components are subjected during operation. Thus the lifetime of such components might be drastically reduced.

The surface structures of the resolidified melt on the samples vary considerably with the materials tested. On stainless steel and molybdenum the resolidified melt has a structure with depressions and ridges (Fig. 4, 5, 11 a) which indicates that a strong motion of the melted layer occurred. On aluminium and copper the resolidified surfaces remained smooth indicating weak melt layer motion (Fig. 8 a, 10 a). In disruption simulation experiments mainly two forces contribute to the motion of a melt layer:

- a) Surface tension gradients in the melt generated by temperature gradients between the melt surface and the solid-liquid interface.

Due to these surface tension gradients the melt can undergo lateral motions. The resulting flow of the liquid can create depressions of the melted surface as well as ridging of the liquid surface in other areas. During recrystallization this distortion of the liquid surface is frozen in creating a roughened rippled surface /84,85/.

- b) Gradients of the melt temperature, especially in lateral direction, lead to strong gradients of the vapor pressure of the melt as the vapor pressure exponentially rises with the temperature of the material. The local differences in vapor pressure may thus exert a force on the melt which leads to a local redistribution of the melted material. In electron beam and laser welding under very high power densities this process is of extreme influence on the geometry of the weld crater and known as "deep welding effect" /86,87/.

In laboratory high heat flux experiments always both processes (a and b) interact with each other. The kind of experimental device usually determines which of both processes outweighs the other in finally shaping the resolidified melt zone:

1. Electron beam facilities operated with a stationary beam of small diameter (<10 mm) usually lead to melt layer structures with a single depression located close to the beam center /30,34,47/. It is assumed that a strong lateral variation of the melt vapor pressure occurs because of a rather narrow gaussian-like profile of the beam power density distribution of the electron beam. Thus the higher vapor pressures in the beam center may mainly contribute to the motion of the melt forming "craters" with a single depression.

2. Electron beam facilities operated in scanned mode can produce fairly homogeneous heat loads over areas of a few cm^2 . Thus the effect of vapor pressure differences on the melt layer formation is reduced /25,43,49/.
3. NBI test stand facilities are providing very broad beam profiles with very small gradients in the power density distribution. Here mainly gradients of the surface tension are the driving force in forming the surface structure of a melt layer. Figure 6 shows a depression in the melt layer of a sample which occurred as a result of melt layer motion.

Additionally it has to be mentioned that strong motions of the melt layer during high heat flux events can result in enhanced vaporization processes under "differential vapor recoil" mechanisms which can approach a 20-fold increase of the liquid evaporation rate compared to evaporation from a motionless liquid surface /88-90/. This may also provide an explanation for the difficulties which occur in numerical modelling of evaporation losses during high heat flux events and discrepancies between numerical and experimental results /41-43,48,49/.

Regarding tokamak processes two effects might occur with respect to melt layer instability and plasma-wall interaction: Electromagnetic forces ($\vec{J} \times \vec{B}$) which are exerted on the melt may cause the loss of the melt layer as the liquid metal can be wiped away by this force. By such an effect or by motion and redistribution of the melt the component thickness can be reduced considerably as the melt layer does not shield the underlying solid material against further heat flux incidence which can lead to

accelerated melting of the solid phase. Another effect which might result from the changes of the surface structure by melting and resolidification is an increase in the impurity flux from the wall to the plasma during plasma-wall interaction. As for a smooth wall the incidence of plasma particles on the surface is glancing the incidence conditions for plasma particles on rough surfaces vary from glancing incidence to nearly perpendicular incidence depending on the location /91/. Particles and thus also heat fluxes onto locations where structural ridges are in contact with the plasma are significantly higher than on locations with glancing particle incidence. As a result of the higher particle and heat loads onto ridged locations the impurity emission into the plasma is enhanced in areas where the wall surface is structured by melting and resolidification processes.

5. Response of graphites to high heat fluxes

5.1 Present state of experimental research on the high heat flux behaviour of graphites

Several studies on the high heat flux behaviour of graphites were performed by use of electron beam facilities /26,37,43,48,53,92-100/. A part of these studies was performed on graphite materials with carbide coatings /37,53,99,100/. As the electron beam facilities at which these experiments were carried out are identical with those used for studies on the high heat flux behaviour of metals (c.f. 4.1), also the beam energies (5 to 150 keV) and the range of pulse durations (20 ms to a few s) were similar. In addition to these electron beam experiments one

brief study on two graphites was carried out at the NBI test stand of the Institute of Plasma Physics of Nagoya University /101/. Broad studies overviewing a wide range of graphites and other carbon materials with respect to crack behaviour and erosion are documented in /93-95/. The present state of high heat flux research on graphite materials has been comprehensively summarized in /1/. A general baseline on the high heat flux behaviour of graphites may be drawn as follows:

erosion: The sensitivity of graphite to erosion under high heat fluxes varies within a factor of 5. Significant erosion occurs along the line: 11 MW/m², 20 s /26/; 22 MW/m², 5 s /26/; 50 MW/m², 1 s /95/; 100 MW/m², 0.1 s /95/; 600 MW/m², 0.02 s /48/. Above these values the weight losses increase drastically with erosion of carbon particles contributing to the weight loss as well as material vaporization.

crack formation: The formation of cracks was found to be highly dependent on the material and on the specimen geometry which might lead to stress concentration under heat load followed by cracking. No systematic effort has been undertaken to explain cracking modes and the material influences on crack initiation and crack propagation.

5.2 Experiments on graphite

5.2.1 Materials selection and experimental procedure

For these experiments 13 grades of fine grain graphite of US-, Japanese, and European origin have been selected. Either components of the selected grades are already applied in operating devices or the grade appeared to be promising from the viewpoint of mechanical, thermophysical or microstructural properties. Selected were:

- isotropic graphites of high mechanical strength:

AXF-5Q, ZXF-5Q, ISO 880, T6-P, MT 200 K

- isotropic graphites:

CL 5890 PT, EK 98, FE 219, ETP-10, IG 110

- anisotropic graphites,

slight anisotropy: ATJ (not impregnated)

CGW (impregnated)

strong anisotropy: YPD

A list of the graphite manufacturers is given in Table 5. The thermophysical and mechanical properties of the tested graphites are listed in Table 6.

The graphite samples were machined from larger blocks by dry sawing, milling and drilling of the shape, the slit and the hole for the attachment to the sample holder (Fig. 13). Except for the small size samples of a screening test the samples had a surface area of 50 mm x 50 mm and a thickness of 20 or 30 mm (EK 98). Additionally for samples used

in experiments described in 5.2.3 a hole of 6 mm diameter had been drilled centrally into the sample front surface. The surface which was to be exposed to the beam was ground. Some samples had polished surfaces.

All samples were cleaned in an ultrasonic bath with ethanol for three times five minutes each time. After each cleaning period the ethanol was exchanged. The baking of the samples was performed at a temperature of 300°C for 20 h under a vacuum of 10^{-4} Pa. After the baking the samples were stored under a vacuum of less than 10 Pa until the experiment.

For the experiments on graphite a sample holder without cooling system was built. On the 15 mm thick copper backing plate of the sample holder four graphite samples were attached in a vertical line. The samples were fixed to the backing plate by bolts to be screwed to metal counterparts which were inserted in a slit machined in the graphite samples (Fig. 13).

During experiments on graphite the ion source terminated operation after pulse lengths of 145 to 353 ms. This termination of the ion source operation is due to arcing between the extraction grids of the ion source which seems to be caused by contamination of the grids. It is likely that the contamination during the experiments occurs in the form of deposition of hydrocarbons which reduces the field resistance against arcing or by deposition of small carbon particles which cause deformation of the electrical field between the grids.

After an experiment and the break down of the ion source caused by grid

contamination extensive reconditioning of the ion source was needed to remove the contamination from the extraction grids and to reach experimental conditions again.

After beam exposure samples were examined visually and by SEM and the weight loss was measured by means of a microbalance. Aims of the observations were the clarification of the erosion process on graphite materials under high heat flux conditions and the determination of the resistance to thermal shocks under disruption conditions.

5.2.2 Results of the comparative experiments on graphite materials

The parameters of the experiments which were performed on graphite are listed in Table 7 and a summary of the experimental results on these materials is given in Table 8.

Screening test:

For a first orientation a screening test with 14 samples of nine different grades of graphite (AXF-5Q, ISO 880, T6-P, MT 200 K, CL 5890 PT, EK 98, ETP-10, IG 110, and YPD) was done by means of small samples which were clamped together and exposed to hydrogen beam pulses at the same time. The samples had a surface of 5 mm x 10 mm and were all placed in the beam center (Fig. 14). They were subjected to three pulses at power densities and pulse lengths of 94 MW/m², 227 ms; 94 MW/m², 170 ms; and 102 MW/m², 195 ms.

After the experiment the YPD sample (II) shows far less signs of erosion

compared to the other samples (Fig. 14). AXF-5Q and ISO 880 show a very homogeneous erosion structure. Other graphites (T6-P, MT 200 K, CL 5890 PT, EK 98, ETP-10, and IG 110) display a more irregular erosion structure with surface voids of several 10 μm . The appearance is similar to microcracks but the penetration depth of these voids is very small. It is more likely that just a few binder bridges between grains have failed. The surfaces of T6-P, IG 110, EK 98 and MTK show several voids of about 50 μm diameter where obviously particles have been emitted from the surface. Cracks only occurred on the surfaces of AXF-5Q and ISO 880.

Full size samples:

On 13 graphite grades experiments were performed with samples of a surface area of 50 mm x 50 mm as listed in Table 7. After the experiments changes on the samples and sample surfaces were observed as discoloration, erosion of surface areas, surface cracking (Fig. 15) and fracture (Fig. 16). SEM micrographs of the sample surfaces and micrographs of ceramographic cross sections of samples after single pulse beam exposure are given in Figures 17 to 32 for each tested graphite grade. The results can be described as follows:

AXF-5Q (Figs. 17): The erosion structure observed on samples of this grade appears to be very homogeneous. Erosion preferentially occurs around grains which leads to a fine structured surface as the grain size of AXF-5Q is about 4 μm .

Cracking of the sample surface already occurs under a moderate heat load of 93 MW/m^2 and 176 ms. The cracks appear on the surface in a net-like structure of high density as the spacing between cracks is only in the

order of a few mm. In the surface plane crack propagation is either straight or slightly curved in areas close to neighboring cracks as there the surface stress distribution changes. Cross sections show that the cracks do not propagate deeply into the bulk material and do not exceed depths of 1.6 mm from the heat loaded surface. Crack initiation at the surface appears to have been perpendicular to the surface plane whereafter cracks frequently propagate in curved fashion.

Microscopically these cracks propagate fairly straight and do not dissipate into larger numbers of smaller cracks.

ZXF-5Q (Figs. 15, 18): The appearance of the erosion structure is even more homogeneous than that of AXF-5Q due to the extremely fine grain (<1 μ m) of ZXF-5Q. Also on this material strong surface cracking is found (Fig. 15). Compared to AXF-5Q the sensitivity to crack formation seems to be slightly higher. Despite a higher crack density on the surface the appearance of cracks is very similar to that of cracks on AXF-5Q. The maximum depth of crack penetration from the surface to the bulk material is 1.6 mm.

ISO 880 (Figs. 19, 20): The -compared to AXF-5Q- slightly larger grain size of ISO 880 leads to a slightly less homogeneous erosion structure. Binder areas around grains are preferentially eroded leaving the spherical grains bare to the heat flux. Part of the binder bridges between grains have failed so that some grains are only in loose contact with the substrate.

ISO 880 appears to be highly sensitive to surface cracking under heat flux incidence. The cracking pattern is the same as that of AXF-5Q only

with the density of the cracks in the surface plane being significantly higher. The maximum penetration of cracks into the bulk material is 1.4 mm and after initiation in direction perpendicular to the heated surface the cracks propagate in curves (Fig. 20). Also -like AXF-5Q- in the bulk the cracks do not branch into several smaller cracks but propagate microscopically fairly straight through the material.

T6-P (Figs. 21): The erosion of this material is fairly homogeneous with the binder phase being preferentially eroded around grains. Crack occurrence is less than on the before mentioned graphite grades. The penetration depth into the bulk material is very small with a maximum depth of 1.0 mm. Also the cross sections show that after initiation the further propagation is fairly straight without pronounced curves as frequently observed on AXF-5Q, ZXF-5Q, and ISO 880.

MT 200 K (Figs. 22, 23): Microscopically showing a less homogeneous erosion structure than the other materials described, on the surface of MT 200 K several voids with diameters of less than 100 μm are found. These voids are left by carbon particles, typically clusters of a few grains which were emitted from the surface. The emission of such particles seems to be caused by the preferential erosion attack to the binder phase of the material leaving the structure of the graphite grains fairly unharmed. Subsequently around grains or clusters of grains binder bridges that have failed by microfracture can be observed. Thus the adherence of such grains or grain clusters to the graphite substrate is weakened and the emission of such particles can occur (cf. 5.3.1).

Cracks on the surface of MT 200 K are less straight in their propagation

than the cracks observed on the materials described before. It appears as if these cracks follow inhomogeneities of the material which cause an irregular cracking pattern (Fig. 22). In cross sections (Fig. 23) the maximum penetration depth of cracks into the bulk material is found to be 1.2 mm although crack propagation is not curved like with AXF-5Q or ISO 880. Microscopically cracks in the bulk propagate in a "zig-zag" like mode which resembles to the crack propagation mode found on the sample surface.

CL 5890 PT (Figs. 24, 25): Erosion on CL 5890 PT surfaces is slightly more homogeneous than on MT 200 K. Also the failure of binder bridges around grains or grain clusters is observed less frequently. Several cracks are found on CL 5890 PT surfaces after the experiments with a maximum penetration depth into the bulk of 1.4 mm. Although macroscopically the cracks are not curved the microscopic propagation of the cracks seems to follow the structure of the material with grains and voids (Fig. 25).

EK 98 (Figs. 26): The erosion structure of EK 98 appears to differ from those described before as with this material grains and binder are eroded simultaneously. Thus the failure of binder bridges around grains is observed less frequently on EK 98.

Already under moderate heat fluxes of 70 MW/m^2 for 290 ms cracks occurred on EK 98. Crack propagation on the surfaces is very irregular with smaller cracks dispersing from larger cracks into the neighbouring material. From cross sections it is found that cracks propagated into the material in straight and in curved mode with a maximum propagation

depth of 1.8 mm. Like on the material surface also in the bulk the cracks frequently disperse into several smaller cracks until they are stopped.

FE 219 (Fig. 27): The comparatively large grain size of the material leads to an inhomogeneous erosion structure as the binder phase around the grains is preferentially eroded. Also on the surfaces of grains traces of erosion attack can be found (Fig. 27). Locations where particles were emitted from the surface due to a lack of adhesion can be found frequently (compare with MT 200 K). On the surface of one sample a microcrack was found with very irregular propagation pattern, similar to the one observed on EK 98 surfaces.

ETP-10 (Fig. 28): The erosion pattern on ETP-10 surfaces is very similar to that of MT 200 K. Frequently voids of up to 200 μm length are observed which seem to be caused by failure of binder bridges under erosion attack and surface stresses. Cracks were not observed on ETP-10.

IG 110 (Fig. 29): The erosion structure on IG 110 appears to be inhomogeneous with strong preferential erosion of the binder phase between grains as a comparison of slightly eroded areas with heavily eroded areas shows (Fig. 29). Cracks were not observed on IG 110.

ATJ (Fig. 30): The surface structure of heavily eroded areas on ATJ appears very inhomogeneous. Erosion on this material seems to cause a loosening of the surface structure which allows the emission of particles as large numbers of surface voids indicate. Grains of larger size (about 20 to 30 μm) are frequently found to be only loosely

attached to the surface as the binder around them has failed. Cracks were not observed on ATJ.

CGW (Fig. 31): The appearance of the CGW surface after the experiment is identical with the appearance of ATJ surfaces described above. Cracks were not observed on CGW.

YPD (Fig. 32 (II)): Under heat load incidence parallel with the grain orientation (//) the material shows a fairly homogeneous erosion structure resembling the structure of CL 5890 PT. On YPD the binder phase around grains is preferentially eroded. Grain surfaces show traces of erosion attack. In general no difference in the erosion pattern could be detected between beam incidence parallel with the grain orientation (//) and beam incidence perpendicular to the grain orientation (\perp) although extreme differences in the sensitivity to heat fluxes in terms of erosion were observed as YPD is highly anisotropic in its thermal properties (see Table 6, 7). The high thermal conductivity of YPD in (//)-direction caused a lower surface temperature under heat flux incidence in this direction and thus significantly lower erosion. As a result of this the ion source contamination during the experiments on YPD (//) was reduced leading to pulse lengths above 300 ms. Compared to this the low thermal conductivity of YPD in (\perp) direction caused higher surface temperatures on the sample and thus a stronger erosion. Rapid contamination of the ion source led to pulse lengths of about 200 ms (see Table 7). In the experiments one sample of YPD (//) fractured under a heat flux of 96 MW/m^2 and 309 ms pulse length.

5.2.3 Behaviour of graphite materials under stress concentration

Experiments under this aspect were carried out to clarify processes of crack initiation and crack propagation in graphites and to determine the influence of the surface geometry on the functional integrity of graphite first wall components under high heat fluxes. For these experiments samples of shape and geometry like the ones used in 5.2.2 (see Fig. 13) were modified by drilling of a 6 mm diameter hole into the center of the front surface (Fig. 33). Similar design schemes are frequently found with graphite first wall components for tokamak applications (e.g. TFTR, JT-60, and (intended) TEXTOR). Usually such holes in the front surface are needed for the attachment of graphite components to backing structures from the front side. It is expected that during high heat fluxes on such surfaces thermal stresses concentrate tangentially around the edge of the holes.

For comparability of the results of these experiments with the results of the experiments performed on "intact" samples (c.f. 5.2.2) five graphite grades were selected which also had been tested in the previous series. The experimental parameters are listed in Table 7.

AXF-5Q (Figs. 33, 34): From the macroscopic picture (Fig. 33) it can be seen that several large cracks were initiated at the edge of the hole and propagated radially to the sample edges. Depending on the stress field on the sample surface some of the cracks are curved and form branches in areas of high surface stresses. Figure 34 shows micrographs of one of these cracks initiated at the edge of the hole. Obviously the failure was induced by tangential compressive stresses which occurred

along the edge of the hole under the applied heat load. A view along the crack into the depth of the hole (Fig. 34 c) shows deep propagation of the crack into the bulk material. Examinations reveal propagation depths of up to 10 mm which is far higher than the propagation depths recorded on AXF-5Q samples without hole (c.f. 5.2.2, max. crack propagation depth 1.6 mm). The actual site of crack initiation is shown in Figure 34 b. Failure of the material seems to be induced by compressive stresses in the surface layer as the graphite in this area failed irregularly leading to outbreaks of larger particles. The further propagation of the crack into the depth of the material is supposed to have been caused by tensile stresses in the "cold" material zone. Thus the pattern of further crack propagation is more straight compared to the more irregular "initiation" pattern (Fig. 34 b).

CL 5890 PT (Fig. 35): Compared to AXF-5Q crack formation on CL 5890 PT samples was slightly less intense. Cracks initiated at the hole edge propagated radially from the hole with some cracks reaching the sample edge. The crack propagation mode on CL 5890 PT is less straight than on AXF-5Q which seems to be caused by small local inhomogeneities in the material structure. The site of crack initiation (Fig. 35 b) is very inhomogeneous in appearance with the crack forming a "zig-zag" pattern. Ranging deeper into the depth of the material (Fig. 35 c) the mode of crack propagation is similar to the one observed in the cross section of a CL 5890 PT sample without hole (Fig. 25). Like with AXF-5Q cracks initiated at the edge of the hole range deeply into the material (about 10 mm).

ETP-10 (Fig. 36): Compared to AXF-5Q and CL 5890 PT less cracks by

number and penetration depth were initiated at the hole edge of ETP-10. The basic initiation and surface propagation pattern of cracks on ETP-10 is similar to CL 5890 PT. The propagation of all cracks on the sample surface is stopped before reaching the sample edge. Figure 36 b gives an example of a crack tip where the propagation of such a crack on the sample surface is stopped by dispersion in the structure of the material. The penetration depth of cracks into the bulk was found to be very shallow. Tensile stresses, even under concentration at the hole edge are not sufficient to cause deep crack propagation in ETP-10.

IG 110 (Fig. 37): A few cracks were initiated at the edge of the hole under the applied heat fluxes. Two types of cracks could be detected. On one side cracks which after initiation by compressive stresses at the sample surface propagated into the bulk driven by tensile stresses. Usually these cracks propagated for a few mm into the bulk (Fig. 37 b). On the other side small cracks which were initiated in the same way, but which did not propagate into the bulk (Fig. 37 c). The propagation pattern of larger cracks on the sample surface is similar to the one observed on CL 5890 PT.

ATJ (Fig. 38): At the edge of the sample hole only very few microcracks could be detected which did not propagate into the bulk deeply (Fig. 38 a). These cracks are dissipated into branches and thus only have very short ranges on the material surface (Fig. 38 b). The fairly inhomogeneous structure of the ATJ material is ideally suited for arresting crack tips (Fig. 38 c). Thus in a comparison of all tested materials from 5.2.2 and 5.2.3 ATJ seems to have the highest resistance against crack initiation and crack propagation under high heat fluxes.

5.3 Discussion of the experimental results on graphites

5.3.1 Erosion

For a comprehensive evaluation of the experimental results on erosion of graphite materials the weight loss in the experiment was correlated to a heat flux parameter F as shown in Figure 39. The heat flux parameter F

$$F = \frac{P}{A} \sqrt{t}$$

with: P/A : power density in MW/m^2

t : duration of the heat flux in s

was chosen to combine the factors power density and duration of the heat load in one parameter which is in accord with the process of one-dimensional surface heating. For one-dimensional heat flux impact on surfaces with durations shorter than the thermal diffusion time of the samples the temperature rise on the sample surface is only dependent on power density and duration of the heat flux ($P/A \sqrt{t}$) and the material properties density, thermal conductivity, and specific heat [32,74,76,77,102]. As in the experiments the heating conditions were almost one-dimensional in the area of the sample (broad energy density distribution profile of the beam, Fig. 3) and the duration of the heat loads well below the thermal diffusion time, the heat flux parameter F is a parameter in close relation to the thermal reaction of the sample. This parameter allows to compare the erosion results of the experiments, although the pulse lengths varied in between 145 and 353 ms. A more detailed description on this parameter is given in [2]. Figure 39 shows the experimental results on erosion obtained on graphites as described in 5.2.2 and 5.2.3.

The figure indicates that the threshold for the occurrence of erosion on graphite under high heat fluxes is about $36 \text{ MW/m}^2\sqrt{\text{s}}$ which corresponds to power densities and pulse lengths of 114 MW/m^2 for 100 ms, 80.5 MW/m^2 for 200 ms, or 66 MW/m^2 for 300 ms. These values are in the range of the threshold values given in the literature (c.f. 5.1). Above these values weight losses by erosion rapidly increase.

The measured weight losses show significant scatter with ZXF-5Q showing very little erosion at moderate heat fluxes (2.5 mg at $47 \text{ MW/m}^2\sqrt{\text{s}}$) and one YPD sample (II) with small weight loss under high heat flux (13.3 mg at $57 \text{ MW/m}^2\sqrt{\text{s}}$). On the other side ATJ shows high erosion of 36.1 mg under a heat flux of $55 \text{ MW/m}^2\sqrt{\text{s}}$. The other graphites show weight losses varying within a factor of about 2 at comparable heat fluxes. AXF-5Q marks the lower end of this band with moderate erosion.

For an understanding of these erosion results several processes which contribute to the overall weight loss have to be taken into account:

Vaporization: Temperature driven vaporization of carbon is one of the main causes of erosion under high heat fluxes. With rising surface temperature the vapor pressure of materials rises exponentially which leads to increasing vaporization of material /76,77/. An energy balance between incoming heat flux, energy expended into vaporization and energy expended into radiation and thermal conduction is supposed to be reached at an equilibrium temperature of about 2900°C in short pulse/high heat flux experiments on graphites /101,103/. Large amounts of the vaporized material condense on colder surfaces near the heated area to form layers of pyrolytic carbon-like structure. Figure 40 shows a thick pyrolytic

carbon-like coating deposited on a collector surface next to the heated surface of carbon material samples. However the significant scatter in weight loss which occurred in the experiments cannot be explained sufficiently by vaporization processes only.

Particle erosion: After the experiments on most of the graphite samples surface areas were detected where binder bridges between grains were preferentially eroded and where such binder bridges have failed by microcracking. Frequently this failure occurs around large single grains or grain clusters typically of about 50 to 100 μm diameter. Figure 41 a, b, c gives three examples for such a loosening of the surface structure around grain clusters by preferential erosion and microcracking for ETP-10, CL 5890 PT, and ATJ. Clusters around which this process has reached an advanced stage may be emitted from the surface as particles. Figure 41 d shows a surface void on MT 200 K where obviously such a particle must have been emitted.

Figure 42 schematically shows the process of particle erosion. Before the experiment (1) the surface appears with grain surfaces, binder areas, and pores between grains /104/. With the onset of the heat flux the surface temperature rapidly rises and compressive stresses develop in the surface layer (2). Binder areas between grains are preferentially subjected to erosion. Increasing compressive stresses with the continuation of the heat flux cause microfailure of binder bridges between grains which already are weakened by preferential erosion (3). Compressive stresses in this surface area can be locally released by the emission of such a particle (4) whose contact to the substrate has been weakened before.

It is assumed that the tendency to such an erosion behaviour depends on the graphite grade, especially the kind of filler and binder, the grain size, and the heat treatment. As in these respects significant differences exist between the tested graphites, the scatter in the erosion behaviour may be largely ascribed to the process of particle erosion.

Chemical and physical sputtering: Compared to the two effects mentioned before the influence of chemical and physical sputtering is regarded as negligible. The critical temperature range for chemical sputtering of graphite (500°C to 900°C) /105-109/ is quickly passed within some 10 ms during the experiment. The hydrogen fluence of a high heat flux pulse is too low to cause significant weight loss by physical sputtering (hydrogen fluence about 1.5×10^{17} at/(cm² pulse)) /109-111/.

5.3.2 Cracking

During the high heat flux experiments on graphite (cf. 5.2.2) cracks were initiated on the sample surfaces of the following grades: AXF-5Q, ZXF-5Q, ISO 880, T6-P, MT 200 K, CL 5890 PT, EK 98, and FE 219 (microcrack) (see Table 8).

The description of the cracking behaviour of the various graphites in the experiments by use of a common figure of merit for the thermal shock resistance of materials R or a modified figure R' proved to be impossible /112/. Figures for the various graphites given by

$$R = \frac{\sigma}{E \alpha} \quad \text{or} \quad R' = \frac{\sigma \sqrt{k}}{E \alpha}$$

with σ : ultimate strength

α : coefficient of linear thermal expansion

E: Young's modulus

k: thermal conductivity

did not show any correlation to the experimental results. This may be due to the strong temperature dependence of the physical and mechanical properties employed in the figures of merit (σ , k, E). The data base for these properties at temperatures above 2200⁰C which seem to be relevant for the case of disruption heat loads and their simulation /101,103/ is insufficient.

Depending on the raw materials used, the pressing method and the graphitization temperature during the production process the high temperature properties of graphites vary considerably, especially in the temperature region above 2000⁰C where graphite starts to show increasing ductile behaviour /104/. Qualitatively the parameters of the thermal shock resistivity figures are dependent on the temperature as follows /104/:

Ultimate strength (tensile, compressive, flexural):

The mechanical properties of graphite improve at elevated temperatures. The maximum values are reached between 2200⁰C and 2500⁰C depending on the graphite. At higher temperatures the ultimate strength decreases rapidly due to the increasing plasticity of the material.

Young's modulus:

The value of the Young's modulus at elevated temperatures is highly dependent on the material (degree of graphitization, anisotropy, porosity). In general the Young's modulus increases with temperature until reaching a turn around from which the modulus starts to decrease again. The temperature of this turn around and the gradient of the decrease in the Young's modulus vary over a wide range depending on the material.

Linear thermal expansion coefficient:

With rising temperature the coefficient of linear thermal expansion slightly rises.

Thermal conductivity:

For all graphites the thermal conductivity decreases with increasing temperature quite rapidly to roughly one third from room temperature to 2000°C.

Thus the only parameter left with some reliability for the estimation of the thermal shock properties of various graphites is the linear thermal expansion coefficient as here the temperature dependence is less pronounced. A comparison of the values of the linear thermal expansion coefficient (Table 6) with the cracking behaviour of the graphites shows that all graphites with large thermal expansion coefficients (larger than $6 \times 10^{-6}/^{\circ}\text{C}$) tended to crack under the applied heat fluxes. Among these the grades with highest sensitivity to cracking were found (ISO 880, AXF-5Q, and ZXF-5Q). Of the graphites with lower coefficients of thermal expansion two grades cracked (CL 5890 PT and EK 98) and one grade showed microcracking (FE 219).

The results obtained on samples where stress concentrations were induced by a 6 mm diameter hole in the heat loaded surface (cf. 5.2.3) are consistent with those obtained on standard samples without holes. In these experiments AXF-5Q proved to be most sensitive to cracking followed by CL 5890 PT. IG 110 and ETP-10 only showed small cracks. ATJ turned out to be most resistant against crack formation.

A comprehensive view on these results leads to the following ranking in sensitivity to cracking under high heat fluxes (in order of increasing cracking resistance):

ISO 880, (YPD: fracture on one sample)

AXF-5Q, ZXF-5Q

EK 98

T6-P, MT 200 K

CL 5890 PT

FE 219

IG 110, ETP-10

ATJ (CGW)

From the observations of cracks on irradiated samples and from the literature on graphite fracture /104,113-119/ a model for the cracking of graphites under high heat fluxes has been derived. In this model the process of cracking is divided into two subsequent phases of crack initiation and crack propagation (Fig. 43).

Crack initiation: During the rapid heating under high heat loads (100 MW/m² and above) graphite surfaces reach temperatures above 2000°C

within 80 ms /76/. The resulting thermal expansion causes large compressive stresses in a thin surface layer of the material /94/. Thus cracking on the surface of a graphite sample is initiated by compressive stresses. Micrographs of the crack initiation sites on graphite samples (Figs. 34 b, 35 b) prove that the initial failure of the material is caused by compressive stresses as the cracking pattern indicates failure by shear /113/. Because this process occurs at surface temperatures well above 2000⁰C, the actual compressive stresses under these conditions presently cannot be determined because of a lack of data on the thermophysical behaviour of graphites above 2000⁰C. As graphite shows increasingly ductile behaviour in this temperature regime the failure of graphite is assumed to occur in an elastic-plastic mode /104/. Under short thermal loads as applied in the experiments (145 to 353 ms) and under even shorter load durations during disruptions (overall duration about 20 ms including thermal and magnetic quench) only a very thin surface layer of the material is heated with steep thermal gradients developing in the material in direction of the incident heat flux which is characterized by the exponential term in eq. (3) (cf. 4.3). Thus the initial driving force for crack propagation into the material is lost very soon because the stress field rapidly changes with a decrease of compressive stresses and a subsequent increase of tensile stresses in the bulk of the material. This tensile stress field is caused by reactive stresses to the thermal expansion of the material surface under the heat load. Additionally the stress field in areas near the surface can change as the induced cracks can cause a relaxation of existing stresses. The curvature of cracks observed on AXF-5Q, ZXF-5Q, and ISO 880 samples seems to have been caused by such changes in the stress field.

Crack propagation: On the samples where thermal induced stresses occurred without additional stress concentration by holes in the surface geometry the observed depth of crack penetration in the bulk material was very small and did not exceed 1.6 mm on any graphite (except YPD, where fracture occurred on one sample). Obviously the stresses in these samples were not sufficient to sustain crack propagation to greater depths.

However under stress concentration which occurred on samples, where a hole was machined in the surface deep crack propagation was observed on AXF-5Q and CL 5890 PT and to a smaller extent on IG 110. In these cases the concentration of tensile stresses tangential to the edge of the hole was sufficient to sustain crack propagation. For the grades ETP-10 and ATJ even these stresses were not high enough for deep crack propagation. The cracks (microcracks) which were induced by the concentration of compressive stresses at the hole edge on the sample surface remained confined to this surface layer.

Observations of the microstructure of the tested graphite grades show a correlation to their cracking behaviour under high heat fluxes.

According to a model on the stress distribution in the front of a crack in graphite /114/ inhomogeneities of the material structure by grains, binder phase, and pores cause considerable variations of the stress distribution compared to a homogeneous material (Fig. 44).

A comparison of the microstructure of a material with the microscopic appearance of cracks shows that with increasing inhomogeneity of the material cracks propagate in a "zig-zag"-like pattern and tend to branch into minor cracks. The "zig-zag" pattern follows the structure of the

material with grains, binder phase, and pores. By this way larger amounts of energy are dissipated into the propagation of cracks with the result of an increased resistance against crack propagation compared to homogeneous materials. Observations on (AXF-5Q, ZXF-5Q, ISO 880) showed that on grades with a very homogeneous microstructure cracks microscopically propagate on a fairly straight path whereas the more inhomogeneous materials (MT 200 K, CL 5890 PT, EK 98) show crack propagation in the "zig-zag" mode. The most pronounced behaviour in this way is shown by ATJ (Fig. 38). This most inhomogeneous grade of the tested materials prevents crack propagation into the depth of the material by immediate dissipation of microcracks into branches which are easily arrested in the structure of the material. Thus for an estimation of the crack propagation resistance of a graphite under tensile stresses besides the tensile strength of the material the microstructure has to be taken into account.

Similar observations were made in studies on fracture toughness and crack growth properties of graphites /104,114,115/. These studies include experiments on coarse and fine grain graphites. As a general result the higher tensile strength of fine grain graphites does not prove to be advantageous in terms of cracking properties as a coarse grain structure prevents straight crack propagation. The high heat flux experiments show that this observation is also valid among fine grain graphites as also here significant differences exist in the microstructure of the material from grade to grade.

Figure 45 shows a schematic of the process of crack formation on graphites under high heat fluxes which includes all parameters of

influence on this process as discussed above. Concerning a further evaluation of the cracking behaviour of graphites under the two stage model of crack initiation by compressive stresses and crack propagation under tensile stresses the following statements may serve as guideline:

- An exact determination of the crack initiation process under compressive stresses presently is impossible as only extremely few data on the mechanical and thermophysical properties of graphites in the temperature region above 2000⁰C are available. Thus presently the only possible way is a phenomenological comparison of the behaviour of different graphite grades as undertaken in this study.
- The process of crack propagation in graphite materials under tensile stresses can be furtherly investigated by experimental work on fracture mechanics as here the data base on fine grain graphites for fusion applications is scarce /104,114-119/.

6. Response of pyrolytic carbon and brazed pyrolytic carbon - copper compounds to high heat fluxes

Pyrolytic carbon is regarded as a material for special applications as first wall component. The very high thermal conductivity of this material in direction perpendicular to the grain orientation gives it the capacity of standing high heat fluxes for long pulses provided the heat is removed by a heat sink of sufficient capability on the backside of the pyrolytic carbon component. Thus it is desirable to attach the pyrolytic carbon material to a metal base structure which is actively

cooled, e.g. by brazing of pyrolytic carbon slices to copper cooling tubes. Such components are expected to have the capability of quasi steady state heat flux removal in the order of 30 to 40 MW/m².

In the frame of several experimental studies using electron beam facilities the high heat flux behaviour of pyrolytic carbon was investigated /26,37,53,93,94/. All these studies report outstanding results in terms of low erosion under high heat fluxes and good thermal shock stability. For a further investigation of the high heat flux behaviour of pyrolytic carbon and a brazed pyrolytic carbon compound system the following experiments were carried out (see Table 9):

Two grades of pyrolytic carbon ("Pyroid" of Pfizer Inc. (*) and

*: Physical properties of the Carbone Lorraine product were not available. For Pyroid of Pfizer the following values are given at room temperature /120/:

flexural strength (σ_F) (-dir.):	84.4 N/mm ²
tensile strength (σ_T) (-dir.):	105.4 N/mm ²
compressive strength (σ_C) (-dir.):	140.6 N/mm ²
(⊥-dir.):	316.4 N/mm ²
Young's modulus (E) (-dir.):	31150 N/mm ²
lin. therm. expansion (α) (-dir.):	1 x 10 ⁻⁶ /°C
(⊥-dir.):	13 x 10 ⁻⁶ /°C
therm. conductivity (k) (-dir.):	346.2 W/(m°C)
(⊥-dir.):	1.7 W/(m°C)
density (ρ):	2.2 g/cm ³

remark: (⊥): against grain orientation
(||): with grain orientation

"normale" of Carbone Lorraine) were subjected to heat flux incidence parallel to their grain orientation (II).

As for the Carbone Lorraine product samples of suitable geometry were not available, three small bars were clamped together with the (II)-direction facing the heat flux. Sample sizes in the experiments varied between 25 mm x 30 mm and 30 mm x 30 mm. In addition to these experiments one test of the Carbone Lorraine grade was carried out with heat flux incidence in (L)-direction of the grain.

The test of a brazed pyrocarbon - metal compound system was performed on a sample with Pyroid bars of 5 mm thickness brazed to a 3 mm thick copper base plate of 40 mm x 40 mm size. As pyrolytic carbon is a material of high thermal conductivity it was expected that a major portion of the incident heat flux is quickly transferred through the pyrolytic carbon towards the brazed interface and the copper base plate. Thus also the interfacial behaviour of carbon material and base metal had to be examined. The following results were obtained by the experiments on pyrolytic carbon:

Pyroid (II) (Fig. 46): After the experiment the surface of Pyroid appeared to be slightly roughened. Further microscopical effects were not detected. Also the weight change of the sample under the heat load was within the range of uncertainty of the measurement (uncertainty 0.5 mg). Several cracks developed on the sample which straightly propagate on the sample surface. An examination of the crack surfaces revealed that crack propagation occurred interlaminar perpendicular to the direction of low thermal conductivity and high thermal expansion.

Carbone Lorraine (normale, II) (Fig. 47): Under the heat load no changes of the surface structure occurred. Also with the Carbone Lorraine grade the weight loss was within the detection limit. Cracks detected on one sample are of a similar mode like the ones found with Pyroid although the extent of cracking is less than on Pyroid.

Carbone Lorraine (normale, I): For purposes of comparison one Carbone Lorraine sample was subjected to heat flux incidence in direction of low thermal conductivity. Under a heat flux of 100 MW/m^2 for 347 ms the sample severely eroded with an overall weight loss of 502 mg.

Brazed Pyroid - copper compound system (Fig. 48): The brazed sample completely failed under the applied heat load of 106 MW/m^2 for 416 ms. Several interlaminar cracks on the Pyroid pieces occurred in the plane perpendicular to the direction of low thermal conductivity and high thermal expansion. However the complete failure of the sample occurred at the interface of pyrolytic carbon and copper where a long crack separated the carbon material layer from the metal base plate. The crack propagated through the brazed interface as well as through the pyrolytic carbon material. Obviously this crack was caused by bending of the copper base plate under the heat load which was transferred through the pyrolytic carbon to the base plate. By way of bending the copper seems to have released internal stresses which were caused by the brazing process of the compound. Because of their nonductility the pyrolytic carbon layers do not have the ability to also bend and thus spalled. The experimental results on pyrolytic carbon and the brazed pyrolytic carbon - metal compound system are of relevance to fusion applications in the following respects:

- As pyrolytic carbon material with front faces that can stand high heat fluxes is only available in small chips of a few cm^2 surface this material can only be applied with these chips being clamped together in a holder structure or being brazed to a metal substrate. Because of this, interlaminar cracking as observed in the experiments is not relevant. As these cracks propagate in a very straight mode holder structures can be designed to keep the segments which resulted from the cracking in place. Also these cracks can be tolerated if the segments are attached to the metal substrate by braze of pyrocarbon - metal compound systems with brazed interfaces.
- In current concepts of actively cooled high heat flux components (e.g. leading edge of pump limiter heads) pyrolytic carbon is attached to copper cooling tubes which are designed to remove the heat fluxes which were deposited on the pyrolytic carbon surface and subsequently transferred through the carbon material to the copper cooling tubes. During the removal of heat fluxes in the range of 30 to 40 MW/m^2 the copper cooling tubes operate at wall temperatures of 300 to 400 $^{\circ}\text{C}$. In the case of a disruption onto such a component a significant amount of additional energy would be transferred through the pyrolytic carbon to the tube walls and there an excursion to temperatures well above the mentioned 300 to 400 $^{\circ}\text{C}$ can occur. In such a case the metal base might undergo plastic deformation to release internal stresses and the brazed pyrolytic carbon layer might spall off as it happened during the high heat flux experiment.

7. Implication of the experimental results for the application of first wall materials and components

Table 10 lists the possible responses of metals and carbon materials to high heat fluxes as derived from the experimental results of this and a previous study /34/. Possible influences of these phenomena on plasma - wall interaction processes and resulting damage to components are indicated. However not all of the observed phenomena due to the response of a material to heat loads have to be regarded as damage (e.g. twin formation) if the integrity of a component is not reduced by this process.

On metals the greatest damage is caused by melting and cracking. In the experiments of this study cracking on samples did not occur before surface melting was initiated. The process of crack initiation under heat loads below the melting threshold was observed on tungsten and tungsten alloys /34,61,121/. Cracks on stainless steel and aluminium are initiated in resolidified melt zones. Due to fatigue growth of these cracks under cyclic operation of fusion devices the lifetime of the first wall can be drastically reduced /122-124/. Several lifetime estimates for metal first wall concepts do not include growth of pre-existent cracks /125-128/.

Figure 49 gives a comparison of the damage threshold for melting on metals and thresholds for erosion and crack initiation on graphites as function of the heat flux parameter F (cf. 5.3.1). For initial melting of aluminium and stainless steel far less heat load is needed compared to copper and molybdenum and initial damage on graphite.

Both disadvantages, the detrimental effect of pre-existent cracks on the fatigue lifetime and the high sensitivity to melting under high heat fluxes of stainless steel and aluminium call for a shielding of these materials against off-normal heat loads from the plasma.

The thresholds for melting of copper and molybdenum are much higher than those for stainless steel and aluminium. An excess of these thresholds has to be carefully avoided during plasma operation. If these metals are melted under excessive heat loads, redeposition of the eroded material will occur on the wall surfaces of the vessel. As redeposited material can be reeroded easily by sputtering of plasma particles, the plasma impurity content during further operation will increase which is especially unfavourable with medium or high Z materials like copper or molybdenum. A model of this process of plasma - wall interaction is described in /129/.

The high particle fluxes from the plasma on collector plates of divertors of next generation devices however demand low hydrogen, hydrogen isotope, and helium sputtering coefficients of the plate material so that high Z materials are preferred for this application as carbon materials would show very limited lifetimes due to comparatively high sputtering yields /8,25,130,131/. If the plasma temperature at the edge of the sheath in front of the divertor collector plate is kept low enough (<50 eV), high Z materials are favourable to low Z materials /132/. Compared to tungsten, another candidate for divertor application which has been tested in other studies /34,61,121/, molybdenum has a higher damage threshold under heat loads as no cracking occurs before initial melting.

Fine grain graphite materials proved to be quite resistant against thermal shocks (see Fig. 49). The main concern with this material is crack formation which can potentially lead to component failure by fracture. The process of cracking on graphite under high heat fluxes can be divided into two stages namely crack initiation under compressive stresses and crack propagation under tensile stresses into the component bulk. The experimental results indicate that considerable differences exist among the tested graphite grades with respect to crack initiation and crack propagation resistance. The best materials in these terms are those with a small coefficient of thermal expansion and a rather inhomogeneous microstructure like ATJ or ETP-10 (cf. 5.2.2, 5.3.2). A low coefficient of thermal expansion will lead to reduced thermal stresses. Cracks which are initiated in a material of comparatively inhomogeneous microstructure are easily dissipated and stopped within the material structure. In addition to the importance of the choice of the graphite grade for gaining maximum thermal shock stability the design of the component is of utmost importance. Under heat loads stress concentrations which can occur along notches or holes in the component can influence the high heat flux resistance to a comparable extent as the choice of the graphite grade (cf. 5.2.3, 5.3.2). Compressive stresses leading to crack initiation as well as tensile stresses being responsible for crack propagation can concentrate along such artificial voids.

One disadvantage in the application of graphites with a comparatively inhomogeneous microstructure is their enhanced erosion under high heat fluxes. Besides the process of vaporization particles of sizes in the order of one or a few grains can be eroded from the heated surface. Both

effects contribute to the erosion on these grades (cf. 5.3.1). However it is assumed that the disadvantage of higher erosion with graphites of rather inhomogeneous microstructure weighs less than the higher resistance against crack initiation and crack propagation. Additionally the curved cracking mode which was observed on graphites with high thermal expansion coefficient (AXF-5Q, ZXF-5Q, ISO 880) (cf. 5.2.2) implies that under subsequent cyclic loads surface layers can easily spall off which would lead to a thinning of the component which far exceeds the erosion effects mentioned before.

As an overall conclusion of these considerations the application of fine grain graphites with low thermal expansion coefficient and an inhomogeneous microstructure is favourable to an application of other grades in terms of high heat flux behaviour. In this context it needs to be mentioned that this recommendation is given without consideration of possible differences in the stability of various graphite grades under neutron irradiation /133/. For a final determination of a prime candidate graphite (PCG) besides the high heat flux behaviour among other issues especially the neutron irradiation behaviour have to be evaluated comprehensively.

The experimental results on the behaviour of graphites under off-normal heat load conditions are relevant for inertially and radiation cooled as well as for actively cooled components with graphites as plasma facing material. Compared to the thermal constant time which is in the same order of magnitude with such inertially or radiation cooled and actively cooled components disruption heat loads are transient effects with duration which are about three orders of magnitude shorter than the

thermal constant time. Thus the disruption response of graphite components of different technology should be similar with each other except the following differences:

- Radiation cooled components as they are proposed for long pulse machines of the next generation, especially NET, are operating at steady state temperatures of 1500 to 1800⁰C /8,130,131,134/. These surface temperatures are reached in compact devices with inertially cooled graphite components at the end of the pulse (CIT-design) /135,136/. It is assumed that disruption heat fluxes on such preheated components will cause higher erosion, because compared to actively cooled components operating at low temperatures of a few hundred ⁰C a larger amount of the incident disruption energy will be expended in vaporization. Whether also the cracking behaviour is influenced is still open.
- Actively cooled components consisting of a plasma facing graphite layer which is brazed to a cooled metal base can have internal residual stresses originating from a mismatch in the thermal expansion coefficients of surface layer and substrate material. The residual stresses in graphite may exert the same effect on crack initiation and crack propagation as it has been found for the case of stress concentration. Thus by internal stresses cracking of the sample under heat loads would be enhanced. On the other hand side the surface geometry of brazed graphite layers does not need to have artificial voids like holes or notches as they are often necessary for the attachment of all graphite components to the wall (e.g. holes for bolts, notches for remote handling). Such stress concentrations under

heat loads can be avoided on actively cooled components.

A special case to be considered are components of pyrolytic carbon layers brazed to actively cooled metal bases. As these components are designed for the removal of very high heat fluxes in the order of 30 to 40 MW/m² /137/ the cooling tubes are operated at high wall temperatures (for copper cooling tubes 300 to 400 °C). During a disruption the incident heat load is quickly transferred from the pyrolytic carbon surface to the metal base due to the very high thermal conductivity of pyrolytic carbon. This additional heat load to the metal tube walls may increase the tube wall temperature as much that internal stresses might be relaxed by deformation of the component. As the pyrolytic carbon layer cannot follow such a deformation this layer might spall from the metal base leading to the failure of the component.

8. Summary

An experimental program on metals and carbon materials was carried out to determine the response of these materials to high heat fluxes and to establish a data base on this issue. The device used for the experiments has been the 10 MW Neutral Beam Injection Test Stand of the IPP Nagoya. Samples were exposed to a hydrogen beam with power densities of 15 to 120 MW/m² and pulse durations of 50 to 950 ms. The distribution of the power density over an area of 40 mm in diameter was almost homogeneous. The use of this device proved that Neutral Beam Injection Test Stands provide a most suitable tool for high heat flux experiments.

Among metals stainless steel, aluminium, copper, and molybdenum were subjected to high heat fluxes. The results can be summarized as follows:

- The melting thresholds for stainless steel and aluminium are similar with each other with about $15 \text{ MW/m}^2\sqrt{\text{s}}$. The melting thresholds for copper ($39 \text{ MW/m}^2\sqrt{\text{s}}$) and molybdenum ($49 \text{ MW/m}^2\sqrt{\text{s}}$) indicate the by far higher heat flux resistance of these materials.
- Cracks in the resolidified melt occurred on stainless steel and aluminium. Such cracks may drastically reduce the component lifetime. This and the low melting threshold of both materials call for a shielding against high heat fluxes from the plasma when applied as first wall materials.
- Very strong motion of the melt caused roughened surface structures after resolidification on stainless steel and molybdenum. The possible influence of this effect on plasma - surface interaction is discussed.

The high heat flux behaviour of 13 grades of fine grain graphite was investigated. In addition the influence of stress concentration on the thermal shock stability of graphite components was determined. The results are as follows:

- Among graphites significant scatter in the erosion behaviour under high heat fluxes exists. This scatter may be caused by a particle erosion process where graphite grains or clusters of grains are emitted from the heated graphite surface.
- The sensitivity to cracking under high heat fluxes considerably varies from grade to grade. The best graphites in terms of thermal shock stability are those with a small coefficient of thermal expansion

which keeps thermal stresses low and an inhomogeneous microstructure which eases the arrest of cracks. For the explanation of the cracking behaviour of graphites a two stage model of crack initiation under compressive surface stresses and crack propagation under tensile stresses in the bulk of the material was developed.

- For a successful application of graphite components a design is needed which avoids the occurrence of stress concentrations under heat loads. In the experiments graphite proved to react highly sensitive to stress concentration with enhanced crack initiation and propagation. However also here substantial differences in the sensitivity to stress concentration exist among the tested graphite grades.

Finally pyrolytic carbon and brazed pyrolytic carbon - copper base components as special purpose materials for the removal of high steady state heat fluxes were evaluated. Here the high thermal conductivity of pyrolytic carbon layers causes a fast transfer of considerable heat loads to the metal base. The metal structure may be heated as much that internal stresses may be relaxed by plastic deformation which can result in the failure of the component as the carbon layer may spall from the metal base.

References

- /1/ Contributions to the "Japan - US Workshop on Plasma Material Interaction / High Heat Flux Data Needs for the Next Step Ignition and Steady State Devices", IPP Nagoya, Jan. 26 - 30, 1987, IPPJ-AM-50 (1987)
- /2/ H. Bolt, A. Miyahara, T. Kuroda, O. Kaneko, Y. Kubota, Y. Oka, K. Sakurai, Inst. of Plasma Physics, Nagoya University, IPPJ-AM-51 (1987)
- /3/ B. B. Kadomtsev, Plasma Phys. Contr. Fusion 26 (1984) 217
- /4/ R. J. Onega, W. R. Becraft, C. A. Kukielka, Nucl. Sci. Eng. 75 (1980) 243
- /5/ B. J. Merrill, S. C. Jardin, M. C. Carroll, in: Proc. 10th Symp. on Fusion Engineering, Philadelphia, Pennsylvania (1986) 1291
- /6/ K. Itami, G. Jahns, H. Yamada, K. McGuire, Princeton Plasma Physics Laboratory, PPPL-2260 (1985)
- /7/ M. Ulrickson in: Proc. Japan - US Workshop on Plasma Material Interaction / High Heat Flux Data Needs for the Next Step Ignition and Steady State Devices", IPP Nagoya, Jan. 26 - 30, 1987, IPPJ-AM-50 (1987) 475
- /8/ F. Engelmann, M. Chazalon, M. F. A. Harrison, E. S. Hotston, F. Moons, G. Vieider, J. Nucl. Mater. 145-147 (1987) 154
- /9/ Conceptual Design Study of Quasi-Steady State Fusion Experimental Reactor (FEQ-Q) Part 1, Japan Atomic Energy Research Institute, JAERI-M 85-177 (1985), in Japanese
- /10/ P. Couture, K. McGuire, Princeton Plasma Physics Laboratory, PPPL-2380 (1986)
- /11/ H. Nakamura, T. Ando, S. Niikura, T. Arai, M. Yamamoto, and JT-60 Team, Japan Atomic Energy Research Institute, JAERI-M 86-173 (1986)
- /12/ G. L. Kulcinski, J. M. Dupouy, S. Ishino, J. Nucl. Mater. 141-143 (1986) 3
- /13/ C. Ferro, E. Franconi, A. Neri, J. Nucl. Mater. 111/112 (1982) 573
- /14/ E. Franconi, M. Barteri, G. M. Ingo, J. Nucl. Mater. 128/129 (1984) 481

- /15/ S. A. Cohen, R. Budny, G. M. McCracken, M. Ulrickson, Nuclear Fusion 21 (1981) 233
- /16/ R. J. Colchin, C. E. Bush, P. H. Edmonds, A. C. England, K. W. Hill, R. C. Isler, T. C. Jernigan, P. W. King, R. A. Langley, D. H. McNeill, M. Murakami, R. V. Neidigh, C. H. Neilson, J. E. Simpkins, J. Wilgen, J. C. DeBoo, K. H. Burell, E. S. Ensberg, J. Nucl. Mater. 76/77 (1978) 405
- /17/ H. Hoven, K. Koizlik, J. Linke, H. Nickel, E. Wallura, Berichte der Kernforschungsanlage Juelich, Juel-2002, Juelich (1985)
- /18/ JT-60 Team, Japan Atomic Energy Research Institute, JAERI-M 87-009 (1987), in Japanese
- /19/ T. Hino, J. DeGrassie, T. S. Taylor, G. Hopkins, C. Meyer, T. W. Petrie, C. Kahn, S. Ejima, and D-III Physics Group, J. Nucl. Mater. 121 (1984) 337
- /20/ M. Nishikawa, H. Yokomizo, A. Kitsunozaki, T. E. McKelvey, T. S. Taylor, D. Doll, N. Brook, R. Seraydarian, J. Nucl. Mater. 128/129 (1984) 493
- /21/ H. Yokomizo, M. Kasai, T. Taylor, R. Callis, D. Doll, H. Aikawa, A. Kitsunozaki, S. Konoshima, T. Matsuda, M. Nagami, M. Shimada, Nucl. Eng. Des./Fusion 1 (1984) 279
- /22/ D. K. Owens in: Proc. 14th Symp. on Fusion Technology, Avignon, France (1986), to be published
- /23/ M. Huguet, J. A. Booth, G. Celentano, E. Deksnis, K. J. Dietz, P. H. Rebut, R. Shaw, K. Sonnenberg in: Proc. 11th Symp. on Fusion Engineering, Austin, Texas (1986) 1239
- /24/ K. J. Dietz in: Proc. Japan - US Workshop on Plasma Material Interaction / High Heat Flux Data Needs for the Next Step Ignition and Steady State Devices", IPP Nagoya, Jan. 26 - 30, 1987, IPPJ-AM-50 (1987) 111
- /25/ T. Tone, M. Seki, A. Minato, T. Horie, H. Kawamura, M. Ogawa, K. Fujimura, T. Takeda, K. Fukuya, H. Iida, M. Sugihara, H. Hashizume, K. Miya, S. Tsujimura, T. Yamamoto, S. Yamazaki, Y. Tanaka, N. Tachikawa, Y. Shibutani, A. Nagata, N. Miki, T. Watanabe, Japan Atomic Energy Research Institute, JAERI-M 86-176 (1986) in Japanese
- /26/ K. Ioki, M. Yamada, M. Nishikawa, T. Uchikawa, M. Onozuka, H. Yamao, Fusion Eng. Des. 5 (1987) 181

- /27/ O. Kaneko, Y. Oka, K. Sakurai, T. Kuroda, Proc. 10th Symp. on Fusion Engineering, Philadelphia (1983) 1502
- /28/ Y. Oka, O. Kaneko, K. Sakurai, T. Kuroda, K. Hayashi, K. Masuda, Y. Samada, Proc. 13th Symp. on Fusion Technology, Varese (1984) 565
- /29/ Y. Oka, O. Kaneko, K. Sakurai, T. Kuroda, Nucl. Eng. Des./Fusion 4 (1987) 387
- /30/ D. Quataert, F. Brossa, P. Moretto, G. Rigon, Proc. 13th Symp. on Fusion Technology, Varese, Italy (1984) 401
- /31/ F. Brossa, E. Franconi, P. Moretto, G. Rigon, J. Nucl. Mater. 141/143 (1986) 210
- /32/ R. DeConinck, A. Gijs, M. Snijkers, Rev. int. hautes Temper. Refract., Fr., 16 (1979) 294
- /33/ Y. Gotoh, H. Hoven, K. Koizlik, J. Linke, U. Samm, B. Thiele, E. Wallura, J. Nucl. Mater. 133/134 (1985) 257
- /34/ H. Bolt, H. Hoven, E. Kny, K. Koizlik, J. Linke, H. Nickel, E. Wallura, Berichte der Kernforschungsanlage Juelich, Juel-2086, Juelich (1987)
- /35/ E. Kny, K. Koizlik, H. Nickel, Proc. 14th Symp. on Fusion Technology, Avignon, France (1986), to be published
- /36/ K. Koizlik, H. Bolt, H. Hoven, J. Linke, H. Nickel, E. Wallura, Proc. 14th Symp. on Fusion Technology, Avignon, France (1986), to be published
- /37/ M. Ulrickson, J. Nucl. Mater. 85/86 (1979) 231
- /38/ M. Ulrickson, J. Vac. Sci. Technol. 18 (3) (1981) 1037
- /39/ D. W. Doll, M. Ulrickson, J. Nucl. Mater. 85/86 (1979) 191
- /40/ A. Tobin, J. Nucl. Mater. 85/86 (1979) 197
- /41/ C. D. Croessmann, G. L. Kulcinski, J. B. Whitley, J. Nucl. Mater. 128/129 (1984) 816
- /42/ C. D. Croessmann, G. L. Kulcinski, J. B. Whitley, Proc. 11th Symp. on Fusion Engineering, Austin, Texas, USA (1986) 884
- /43/ C. D. Croessmann, The Thermal Response of Structural Materials to Intense Energy Deposition, Ph. D. Thesis, University of Wisconsin (1986)
- /44/ C. D. Croessmann, G. L. Kulcinski, J. B. Whitley, Sandia National Laboratories, SAND86-2010 (1986)
- /45/ S. T. Picraux, J. A. Knapp, M. J. Davis, J. Nucl. Mater. 120 (1984) 278

- /46/ J. R. Easoz, R. Bajaj, R. E. Gold, J. W. H. Chi, Nucl. Technol./Fusion 4 (1983) 780
- /47/ J. R. Easoz, R. Bajaj, Proc. 10th Symp. on Fusion Engineering, Philadelphia, Penns., USA (1983) 1008
- /48/ J. R. Easoz, R. Bajaj, J. Vac. Sci. Technol. A3 (3) (1985) 1119
- /49/ M. Seki, S. Yamazaki, A. Minato, T. Horie, Y. Tanaka, T. Tone, J. Fus. Energy 5 (3) (1986) 181
- /50/ M. Seki, T. Tone, S. Yamazaki, Proc. Japan-US Workshop P-70 on High Heat Flux Materials, March 3-5 1986, National Research Institute for Metals, Tsukuba Laboratories (1986) 321
- /51/ M. Seki, S. Yamazaki, A. Minato, T. Horie, Y. Tanaka, T. Tone, Fusion Eng. Des. 5 (1987) 215
- /52/ K. Ioki, M. Yamada, M. Nishikawa, T. Uchikawa, H. Yamao, J. Nucl. Mater. 141/143 (1986) 204
- /53/ M. Onozuka, T. Uchikawa, M. Nayama, H. Yamao, K. Ioki, S. Niikura, H. Nakamura, Proc. 11th Symp. on Fusion Engineering, Austin, Texas, USA (1986) 920
- /54/ M. Onozuka, T. Uchikawa, H. Yamao, H. Kawai, A. Kousaku, H. Nakamura, S. Niikura, Proc. 14th Symp. on Fusion Technology, Avignon, France (1986), to be published
- /55/ D. E. Schechter, C. C. Tsai, F. Sluss, W. R. Becraft, D. J. Hoffmann, Fusion Technol. 8 (1985) 559
- /56/ K. Nakamura, R. Yamada, M. Saidoh, Y. Murakami, J. Nucl. Mater. 111/112 (1982) 852
- /57/ K. Nakamura, Japan Atomic Energy Research Institute, JAERI-M 82-026 (1982) in Japanese
- /58/ K. Nakamura, Japan Atomic Energy Research Institute, JAERI-M 85-089 (1985) in Japanese
- /59/ T. Abe, Y. Murakami, K. Obara, S. Hiroki, K. Nakamura, T. Mizoguchi, A. Doi, K. Inagawa, J. Nucl. Mater. 133/134 (1985) 754
- /60/ M. Yoshikawa, Fusion Eng. Des. 5 (1987) 38
- /61/ M. Shibui, J. Ohmori, S. Itoh, T. Sasaki, T. Kuroda, O. Kaneko, K. Sakurai, Y. Oka, Proc. 11th Symp. on Fusion Technology, Austin, Texas, USA (1986) 877
- /62/ T. Kuroda, O. Kaneko, K. Sakurai, Y. Oka, M. Shibui, J. Ohmori, Kakuyugo Kenkyu (in Japanese) 54 (1985) 371

- /63/ K. Miya, private communication (1986-7)
- /64/ ASM Metals Reference Book (American Society for Metals, n. 1., 1983)
- /65/ R. B. Ross, Metallic Materials Specification Handbook (Chapman and Hall, London, 1980)
- /66/ K. Matsuoka, Y. Hamada, S. Kitagawa, K. Matsuura, Y. Ogawa, K. Toi, K. Yamazaki, Y. Itou, T. Ishizuka, K. Kikuchi, K. Ioki, M. Tomita, T. Yamanaka, Y. Sawada, M. Shibui, T. Takano in: Proc. 10th Symp. on Fusion Engineering, Philadelphia, Pennsylvania (1983) 89
- /67/ K. Ioki, A. Kameari, M. Yamada, M. Nishikawa, Y. Hamada, K. Toi, Y. Ogawa, S. Kitagawa, K. Matsuoka, K. Yamazaki, K. Matsuura, Nucl. Eng. Des./Fusion 1 (1984) 287
- /68/ K. Kamada, T. Sato, T. Noda, N. Kuroishi, K. Abe, H. Kakihana in: Proc. 14th Symp. on Fusion Technology, Avignon, France (1986), to be published
- /69/ Y. Hamada, Y. Ogawa, K. Matsuoka, S. Kitagawa, Nucl. Eng. Des./Fusion 4 (1987) 275
- /70/ K. Kamada, Nucl. Eng. Des./Fusion 4 (1987) 363
- /71/ S. K. Combs, S. L. Milora, C. A. Foster, H. H. Haselton, M. M. Menon, C. C. Tsai, Rev. Sci. Instrum. 56 (1985) 1526
- /72/ C. C. Tsai, W. R. Becraft, W. L. Garner, H. H. Haselton, D. J. Hoffmann, M. M. Menon, W. L. Stirling in: Proc. 11th Symp. on Fusion Engineering, Austin, Texas (1986) 860
- /73/ D. L. Sevier, P. W. Trester in: Proc. 11th Symp. on Fusion Engineering, Austin, Texas (1986) 916
- /74/ J. P. Holman, Heat Transfer (McGraw Hill, New York, 1986)
- /75/ H. W. Carslaw, J. C. Jaeger, Conduction of Heat in Solids (Clarendon, Oxford, 1959)
- /76/ R. Behrisch, Nucl. Fusion 12 (1972) 695
- /77/ R. Behrisch, J. Nucl. Mater. 93+94 (1980) 498
- /78/ Y. S. Touloukian, R. W. Powell, C. Y. Ho, P. G. Klemens, Eds., Thermophysical Properties of Matter, Vol. 1, Thermal Conductivity (IFI/Plenum, New York-Washington, 1970)
- /79/ Y. S. Touloukian, E. H. Buyco, Eds., Thermophysical Properties of Matter, Vol. 4, Specific Heat (IFI/Plenum, New York-Washington, 1970)

- /80/ Y. S. Touloukian, Ed., Thermophysical Properties of High Temperature Solid Materials (Macmillan, New York, 1970)
- /81/ Metallic Materials Data Handbook, Aviation Publication AvP932 (ESDU International, n. 1., 1982)
- /82/ F. Mast, H. Vernickel, J. Nucl. Mater. 111/112 (1982) 566
- /83/ H. Vernickel, J. Nucl. Mater. 111/112 (1982) 531
- /84/ T. R. Anthony, H. E. Cline, J. Appl. Phys. 48 (1977) 3888
- /85/ F. G. Collins, B. N. Antar, AIAA Journal 20 (1982) 1464
- /86/ H. E. Cline, T. R. Anthony, J. Appl. Phys. 48 (1977) 3895
- /87/ S. Schiller, U. Heisig, S. Panzer, Electron Beam Technology (J. Wiley-Interscience, Berlin, 1982)
- /88/ K. Hickman, Indust. Engng. Chem. 44 (1952) 1892
- /89/ H. Palmer, J. Fluid Mech. 75 (1976) 487
- /90/ S. I. Anisimov, A. Kh. Rakhmatulina, Sov. Phys.-JETP, 37 (1973) 441
- /91/ M. Ulrickson, private communication (1987)
- /92/ C. D. Croessmann, G. L. Kulcinski, J. B. Whitley, Sandia National Laboratories, SAND86-0764 (1986)
- /93/ J. Bohdansky, C. D. Croessmann, J. Linke, Proc. 14th Symp. on Fusion Technology, Avignon, France (1986) to be published
- /94/ J. Bohdansky, C. D. Croessmann, J. Linke, J. M. McDonald, D. H. Morse, A. E. Pontau, R. D. Watson, J. B. Whitley, D. M. Goebel, Y. Hirooka, O. Leung, R. W. Conn, J. Roth, W. Ottenberger, H. E. Kotzlowski, Nucl. Instr. Meth. B 23 (1987) 527
- /95/ W. Delle, "1st Workshop on Graphite for Fusion Applications", KFA Juelich, Nov. 21, 1985 and
J. Linke, W. Delle, H. Hoven, E. Wallura, private communication (1986)
- /96/ K. Ioki, M. Nishikawa, I. Tatsumi, T. Uchikawa, M. Fujiwara, J. Nucl. Sci. Technol. 22 (1985) 529
- /97/ T. Uchikawa, M. Fujiwara, R. Nayama, T. Irie, M. Onozuka, M. Tomita, K. Ioki, M. Nishikawa, Fusion Technol. 8 (1985) 1748
- /98/ H. Nakamura, S. Niikura, T. Uchikawa, M. Onozuka, H. Yamao, M. Nayama, K. Ioki, Japan Atomic Energy Research Institute, JAERI-M 86-048 (1986), in Japanese
- /99/ D. L. Sevier, P. W. Trester, G. Hopkins, T. E. McKelvey, T. S. Taylor, J. Nucl. Mater. 103/104 (1981) 187

- /100/ G. R. Hopkins, P. W. Trester, J. L. Kaae, J. Nucl. Mater. 128/129 (1984) 802
- /101/ M. Shibui, J. Ohmori, T. Kuroda, Proc. 14th Symp. on Fusion Technology, Avignon, France (1986), to be published
- /102/ R. Benz, A. Naoumidis, H. Nickel, Berichte der Kernforschungsanlage Juelich, Juel-2056, Juelich (1986)
- /103/ B. Brandt, private communication (1987)
- /104/ W. Delle, K. Koizlik, H. Nickel, Graphitische Werkstoffe fuer den Einsatz in Kernreaktoren, Teil II (Karl Thiemig, Muenchen, 1983)
- /105/ J. Roth in: Topics in Applied Physics, Vol. 52, R. Behrisch, Ed. (Springer-Verlag, Heidelberg, 1983) 91
- /106/ J. Roth, J. Bohdansky, W. Poschenrieder, M. K. Sinha, J. Nucl. Mater. 63 (1976) 222
- /107/ B. Feinberg, R. S. Post, J. Vac. Sci. Technol. 13 (1976) 443
- /108/ R. Yamada, N. Nakamura, K. Sone, M. Saidoh, J. Nucl. Mater. 95 (1980) 278
- /109/ J. B. Roberto, R. Behrisch, J. Nucl. Mater. 128/129 (1984) 764
- /110/ G. M. McCracken, P. E. Stott, Nucl. Fusion 19 (1979) 889
- /111/ J. Bohdansky, J. Roth, Radiation Effects 89 (1985) 49
- /112/ H. Bolt, C. D. Croessmann, A. Miyahara, T. Kuroda, Y. Oka, K. Sakurai in: Proc. of the "Japan - US Workshop on Plasma - Material Interaction / High Heat Flux Data Needs for the next Step Ignition and Steady State Devices" IPP Nagoya, Jan. 26 - 30, 1987, IPPJ-AM-50 (1987) 285
- /113/ H. Kawakami in: Proc. of the "IAEA Meeting on Graphite Component Structural Design" Japan Atomic Energy Research Institute, Sept. 8 - 11, 1986, JAERI-M 86-192 (1987) 163
- /114/ M. Roedig, G. Kleist, H. Schuster, H. Nickel, Berichte der Kernforschungsanlage Juelich, Juel-1632, (1979)
- /115/ H. Kakui, T. Oku, J. Nucl. Mater. 137 (1986) 124
- /116/ T. Oku, S. Ishiyama, M. Eto, M. Inagaki, T. Hashida, H. Takahashi in: Proc. of the "IAEA Meeting on Graphite Component Structural Design" Japan Atomic Energy Research Institute, Sept. 8 - 11, 1986, JAERI-M 86-192 (1987) 217
- /117/ H. Cords, A. Djaloeis, G. Kleist, J. Moench, B. Oefinger, R. Zimmermann, Berichte der Kernforschungsanlage Juelich, Juel-1355, (1976)

- /118/ M. Roedig, G. Kleist, H. Schiffers, H. Nickel in: Contributions for the Fifth London International Conference on Carbon and Graphite, Imperial College, London, Sept. 18 - 22, 1978, W. Delle, Ed., Juel-Conf-25, (1978) 70
- /119/ T. Hayashida, T. Fukusawa, H. Takahashi, S. Ishiyama, T. Oku in: Proc. of the "IAEA Meeting on Graphite Component Structural Design" Japan Atomic Energy Research Institute, Sept. 8 - 11, 1986, JAERI-M 86-192 (1987) 158
- /120/ Pfizer Inc., product information on Pyroid
- /121/ M. Shibui, J. Ohmori, T. Kuroda, O. Kaneko, K. Sakurai, J. Oka, Fusion Eng. Des. 5 (1987) 197
- /122/ T. Fett, A. Mueller, D. Munz, H. Stamm in Proc. 13th Symp. on Fusion Technology, Varese, Italy (1984) 973
- /123/ D. R. Harris, Radiation Effects 101 (1986) 3
- /124/ D. R. Harris, E. Zolti, Nucl. Eng. Des./Fusion 3 (1986) 331
- /125/ International Tokamak Reactor, Phase Two A, Part I and II, (IAEA, Vienna, 1983)
- /126/ D. Ehst, S. Majumdar, Y. Cha, A. Hassanein in Proc. 10th Symp. on Fusion Engineering, Pennsylvania, Philadelphia (1983) 1083
- /127/ A. E. Dabiri, Oak Ridge National Laboratory, ORNL/FEDC-85/9 (1986)
- /128/ J. R. Haines, K. Kitamura, T. Kobayashi, H. Iida, Japan Atomic Energy Research Institute, JAERI-M 86-099 (1986)
- /129/ H. Bolt, H. Hoven, K. Koizlik, J. Linke, H. Nickel, E. Wallura, Berichte der Kernforschungsanlage Juelich, Juel-2024 (1985)
- /130/ J. M. Dupouy, M. F. Harrison, G. Vieider, C. H. Wu, J. Nucl. Mater. 141-143 (1986) 19
- /131/ F. Engelmann, M. Chazalon, M. F. A. Harrison, E. S. Hotston, F. Moons, G. Vieider, EURATOM-Report, EU-FU/XII-80/86/55 (1986)
- /132/ W. M. Stacey, M. A. Abdou, D. B. Montgomery, J. M. Rawls, J. A. Schmidt, T. E. Shannon, R. J. Thome, Nucl. Technol./Fusion 4 (1983) 202
- /133/ IAEA Workshop Report "Graphite in High Power Fusion Reactors", Rigi-Kaltbad, Switzerland, Oct. 18-21, 1982 (1983)
- /134/ Next European Torus, Status Report, EURATOM-Report, EU-FU/XII-80-86/51 (1986)
- /135/ R. Gallix, F. Puhn, G. Listvinsky, J. Weede in: Proc. 14th Symp. on Fusion Technology, Avignon, France (1986), to be published

- /136/ G. Listvinsky, J. J. Weede, S. L. Salem, A. Wolfson, Fusion Technol. 10 (1986) 514
- /137/ J. B. Whitley, J. A. Koski, R. Aymar in: Proc. 14th Symp. on Fusion Technology, Avignon, France (1986), to be published

Parameter	Present devices	Near term	Commercial reactors
Peak heat flux (kW/cm ²)			
Normal operation	0.4-5	0.5-1	0.5-1
Disruptions	80-500	500	500
Pulse length			
Normal (s)	1-5	5-2000	Steady state
Disruptions (ms)	0.02-0.3	0.3-20	3-20
Surface materials	TiC coated C C, Be, Mo	Be, BeO, SiC C, Ta, W	Be, W, Ta
Structural materials	Steels Mo or Ni alloys	Steels Ni or Cu alloys	Refractory or Cu alloys
Coolants	None	H ₂ O	H ₂ O, liquid metals

Table 1: Expected operating requirements for plasma interactive components /12/

Location	IPP Nagoya Japan	JARRI Japan	NRIM Japan	KHI Japan	MHI Japan	Hitachi Japan	SNLA USA	SNLA USA	Westinghouse (ESURF) USA	HEDL USA	KFA FRG	KFA FRG	JRC-Japan Italy
Type of load	H ⁺ , H ⁰	e ⁻	e ⁻	e ⁻	e ⁻	Laser	e ⁻	H ⁺ , D ⁺	e ⁻	e ⁻	e ⁻	H ⁺ , H ⁰	e ⁻
Particle energy	< 120keV	< 100keV	50eV, 2keV (150A/cm ²) (50A/cm ²)	100keV	< 120keV	λ=10.6μm	150keV	40keV	150keV	.25keV	150keV	20... 50keV	60keV
Power density	< 20 kW/cm ²	< 20kW/cm ²	7.5kW/cm ² ~ 100kW/cm ²	17kW/cm ² for 13mmx13mm	~ 100kW/cm ²	up to 1.7kW/cm ²	up to 100kW/cm ²	> 4kW/cm ²	up to 100kW/cm ²		up to 50kW/cm ²	8-15kW/cm ²	up to 50kW/cm ²
Pulse length	< 1s	...10s	1s ~ 10ms 0.5s	1ms...ms	50ms ~ ms	100ms...ms	few ms...ms	10-30s	few ms...ms	0.5s...ms	1ms...ms	100ms...ms ...10s	5ms...ms
Rise time	10ms	50ms	100ms, 5ms	less than 0.2ms	< 50ms	100ms	1ms	1ms	1ms			5...10ms	1ms
Loaded area	< 150mm x 400mm	up to 60 x 80cm	1cm x 1cm, up to 2cm x 2cm	4cm x 4cm *1 40cm x 40cm *2	up to 60cm x 60cm	6cm ²	1...100cm ²	> 100cm ²			up to 25cm ²	150cm ²	< 20mm ²
Total power	9kW	8MW	10KW, ~200KW (pulse)	60KW	120KW	5KW	30KW	800KW	50KW	60KW	30KW	4MW	5KW
Thermal cycling	No	No	Yes, Yes	Yes	Yes	Yes	Yes	Yes	Yes	Yes	Yes	No	Yes
Status	operational	under preparation	operational	operational	operational	operational	operational	systems checkout	phased out	hot cell operation under construction	operational	under preparation	operational

*1 = high frequency rastering mode
*2 = low frequency rastering mode

Table 2: High heat flux test facilities and major technical data.

no.	material	shot no.	pulse length (ms)	power density (MW/m ²)
	stainless steel			
1	1.4311	18050	50	70
2	1.4311	15965	88	64
3	1.4311	15991	504	21
4	1.4311	16084	951	16
	stainless steel			
5	304	20815	101	51
6	304	20787	101	60
7	304	25124	101	76
8	304	28215	151	55
9	304	25125	202	76
10	aluminium	28393	50	68
11	aluminium	20470	101	44
12	aluminium	25124	101	49
13	aluminium	28215	202	32
14	copper	28673	189	97
15	copper	20779	208	94
16	copper	28610	258	83
17	copper	25155	302	80
18	copper	28563	510	60
19	molybdenum	29137	271	104
20	molybdenum	25204	302	77
21	molybdenum	20845	403	80
22	molybdenum	28762	611	62

Table 3: Parameters of the experiments on metals

material	melting threshold ($\text{MW/m}^2\sqrt{\text{s}}$)	structure of resolidified melt layer	cracks in resolidified melt
stainl. steel	14	ripple formation	yes
aluminium	15	plain	yes
copper	39	plain	no
molybdenum	49	ripple formation	no

Table 4: Summary of experimental results on metals

remark: The melting threshold is indicated in form of the heat flux parameter F in $\text{MW/m}^2\sqrt{\text{s}}$ (cf. 4.2.3). The indicated values are valid for short heat loads of less than 1 s with an accuracy of 20 %.

AXF-5Q	and
ZXF-5Q	of Poco Graphite, Inc., 1601 South State St., Decatur, Texas 76234, USA
ATJ	and
CGW	of Union Carbide Corp., Carbon Products Div., P.O. Box 94617, Cleveland, Ohio 44101, USA
ISO 880	and
IG 110	of Toyo Tanso Co., Ltd., 7-12 Takeshima, 5-chome, Nishiyodogawa-ku, Osaka, Japan
MT 200 K	and
YPD	of Toyo Carbon Co., Ltd., 10-1 Nihonbashi, 2-chome, Chuo-ku, Tokyo, Japan
T6-P	and
ETP-10	of Ibiden Co., Ltd., Kandamachi, 2-chome, Ogaki, Japan
CL 5890 PT	of Le Carbone Lorraine, 45, Rue des Acacias, Boite Postale 164, 75821 Paris Cedex, France
EK 98	of Ringsdorff-Werke GmbH, Drachenburgstr. 1, D-5300 Bonn-Bad Godesberg, FRG
FE 219	of Schunk Kohlenstofftechnik GmbH, P.O. Box 6420, D-6300 Giessen, FRG

Table 5: Graphite grades used in the experiments and manufacturers

graphite/ grade	σ_F (N/mm ²)	σ_T (N/mm ²)	σ_C (N/mm ²)	E (N/mm ²)	α (10 ⁻⁶ /°C)	k (W/m°C)	ρ (g/cm ³)
AXF 5Q	90	63	143	11700	7.7	100	1.83
ZXF-5Q	124	90	193	14500	7.7		1.83
ISO 880	95	70	185	13000	6.5	99	1.90
T6-P	100	50	175	15000	6.5	57	1.90
MT 200 K	75	45		14000	6.0		1.80
CL 5890 PT	60	33	130	11600	4.6	74	1.79
EK 98	47	30	110	11500	3.4	69	1.86
FE 219	36	16	75	9200	4.0	75	1.76
ETP-10	50	30	100	11000	3.5	103	1.75
IG 110	40	25	80	10000	4.6	115	1.77
ATJ	:30 ⊥ :25	:30 ⊥ :22	:70 ⊥ :68	: 8400 ⊥ : 6300	:2.1 ⊥ :3.6	:140 ⊥ : 80	1.74
CGW	:37 ⊥ :31	:33 ⊥ :28	:80 ⊥ :78	:12300 ⊥ : 9000	:2.2 ⊥ :3.5	:135 ⊥ :110	1.82
YPD	:50 ⊥ :25				:1-2 ⊥ :12-13	:210 ⊥ : 81	2.0

Table 6: Graphites tested, their mechanical and physical properties (R_T)
 σ_F : flexural strength, σ_T : tensile strength, σ_C : compressive strength, E: Young's modulus, α : linear thermal expansion coefficient, k: thermal conductivity

no.	material	shot no.	pulse length (ms)	power density (MW/m ²)	weight loss (mg)	remarks
1	sandwich	18996	227	94		*, 3 shots on one sample
	sandwich	19011	170	94		
	sandwich	19058	195	102		
2	AXF-5Q	21091	258	94	11.7	
3	AXF-5Q	22127	233	92	8.7	
4	AXF-5Q	24537	176	93		
5	ZXF-5Q	29153	145	98	-0.2	
6	ZXF-5Q	29168	290	97	23.7	
7	ZXF-5Q	67	208	104	2.5	
8	ISO 880	21165	214	93	14.6	
9	ISO 880	24957	164	91		
10	T6-P	24344	164	96		
11	MT 200 K	23474	183	93	10.5	
12	CL 5890 PT	21120	221	94	16.4	
13	CL 5890 PT	23443	176	95	9.0	
14	CL 5890 PT	24713	158	94		
15	EK 98	17102	290	79		two shots on one sample
	EK 98	17120	284	81		
16	EK 98	22356	183	88	0.6	
17	EK 98	23418	176	98	12.9	
18	FE 219	29465	221	97	21.2	
19	FE 219	29566	183	103	15.2	
20	ETP-10	19383	176	98		two shots on one sample
	ETP-10	19431	202	97	28.5	
21	ETP-10	23012	195	91	7.2	
22	IG 110	18175	221	96		three shots on one sample
	IG 110	18210	202	99		
	IG 110	18234	195	105		
23	IG 110	22464	214	94	17.0	
24	IG 110	24805	202	92		

Table 7: Parameters of the experiments on graphite (continued)

no.	material	shot no.	pulse length (ms)	power density (MW/m ²)	weight loss (mg)	remarks
25	ATJ	22321	170	93	9.6	
26	ATJ	23310	221	96	10.4	
27	ATJ	24610	183	92		
28	CGW	22449	227	97		
29	YPD (II)	19102	353	99		two shots on one sample
	YPD (II)	19115	302	101	26.5	
30	YPD (II)	23158	309	96	20.3	
31	YPD (⊥)	19136	202	98		two shots on one sample
	YPD (⊥)	19201	189	98	31.5	

32	AXF-5Q	79	265	105	17.1	stress c. sample
33	AXF-5Q	425	321	103	17.7	"
34	CL 5890 PT	203	277	105	25.0	"
35	CL 5890 PT	486	252	106	22.9	"
36	ETP-10	252	258	102	23.8	"
37	ETP-10	507	214	106	13.1	"
38	IG 110	377	315	103	22.0	"
39	IG 110	632	321	104	18.7	"
40	ATJ	95	271	105	36.1	"
41	ATJ	650	201	103	10.4	"

Table 7: Parameters on the experiments on graphites

remarks: *: 14 small size samples of 9 grades clamped together and irradiated at the same time (see Fig. 14)

stress c. sample: A hole of 6 mm diameter was drilled in the surface of these samples to initiate concentration of thermal stresses at the edge of the hole.

graphite	erosion structure	cracks				behaviour under stress conc.	
		occurrence	macroscopic prop. mode	max. prop. depth (mm)	microscopic prop. mode	tested	observation
AXF-5Q	homogeneous	yes	curved	1.6	straight	X	deep crack propagation
ZXF-5Q	homogeneous	yes	curved	1.6	straight		
ISO 880	homogeneous	yes	curved	1.4	straight		
T6-P	fairly homogeneous	yes	straight	1.0	straight		
MT 200 K	inhomogeneous, str. particle er.	yes	straight	1.2	sl. zig zag		
CL 5890 PT	inhomogeneous	yes	straight	1.4	zig zag	X	deep crack propagation
EK 98	sl. inhomogeneous	yes	curved + straight	1.8	zig zag		
FE 219	inhomogeneous	microcrack					
ETP-10	inhomogeneous, str. particle er.	no				X	cracks at surface
IG 110	inhomogeneous	no				X	slight crack propagation
ATJ	very inhomogen.	no				X	microcracks
CGW	very inhomogen.	no					
YPD	inhomogeneous	one sample fractured					

Table 8: Summary of experimental results on graphite

no.	material	shot no.	pulse length (ms)	power density (MW/m ²)	weight loss (mg)
1	Pyroid ()	32541	321	102	The detected weight losses were within the error range of the measurements (0.5 mg).
2	CL"normale"()	32291	328	103	
3	CL"normale"()	-32681	284	111	
4	CL"normale"(<u>⊥</u>)	32477	347	100	502
5	Pyroid brazed to copper	29	416	106	

Table 9: Parameters of the experiments on pyrolytic carbon and a brazed pyrolytic carbon - copper compound system

material	phenomenon	effect on PWI	damage
metals	relaxation of internal stresses		deformation
	twin formation		
	grain growth		degradation of mechanical properties
	cracking		spalling, possible fracture
	melting	redeposition	loss of melt layer due to EMF; decrease of wall thickness
	vaporization	redeposition	
	preferential vaporization of constituents		
	roughening of resolidified melt layer	increase of impurities	
	cracks in resolidified melt layer		fatigue crack growth into unaffected material may occur

Table 10: continued

material	phenomenon	effect on PWI	damage
graphite	vaporization	redeposition	decrease of component thickness
	particle erosion	redeposition	decrease of component thickness
	cracks (initiated by compressive stresses)		spalling of surface layers may occur
	cracks (initiated by and propagated by tensile stresses)		possible fracture
pyrolytic carbon	cracks (straight propagation)		(use of holder structure can cope with damage)
C - metal systems	C-layer: see graphite and PYC metal: relaxation of internal stresses		deformation of the metal structure (spalling of C-layers from the metal base)

Table 10 (cont.): Response of metals and carbon materials to high heat fluxes, the effect on plasma - wall interaction and possible damage on components

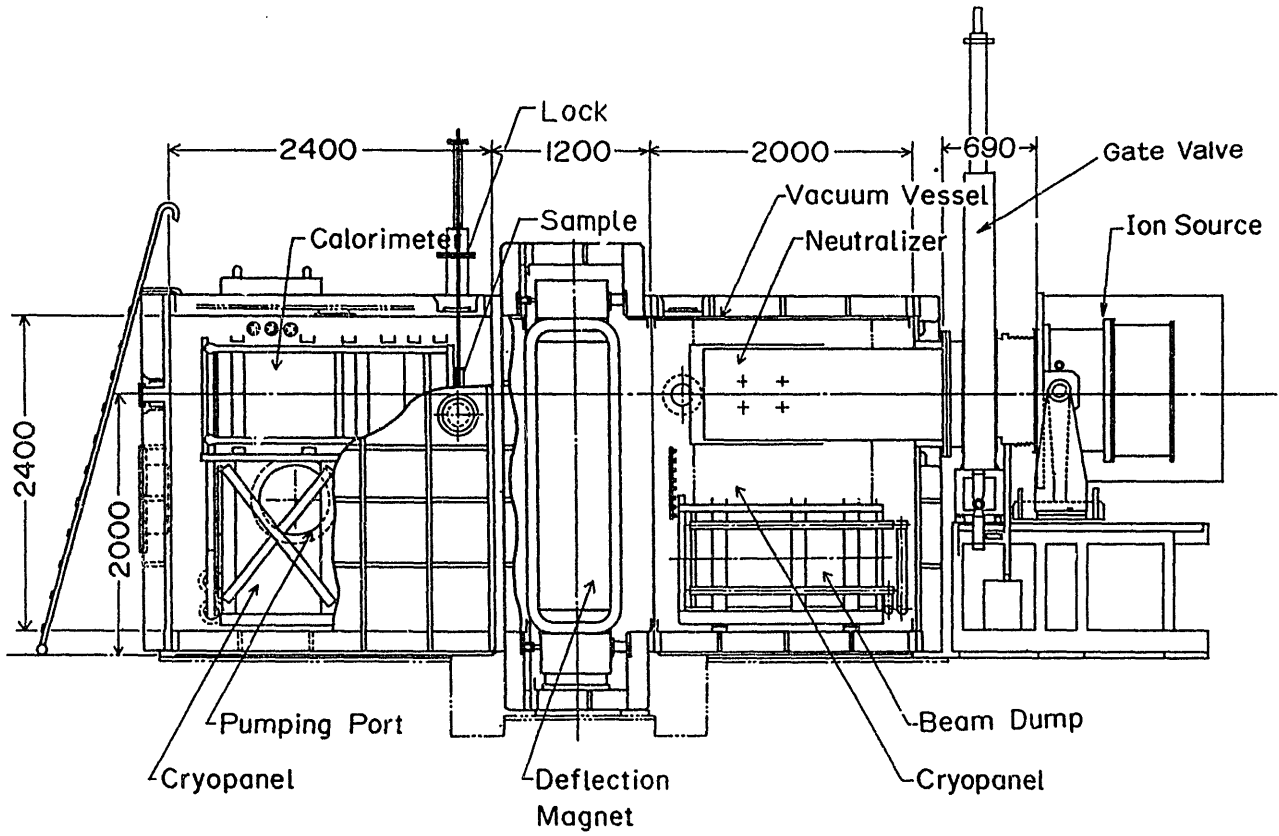


Figure 1: Schematic of the Neutral Beam Injection Test Stand used for materials tests

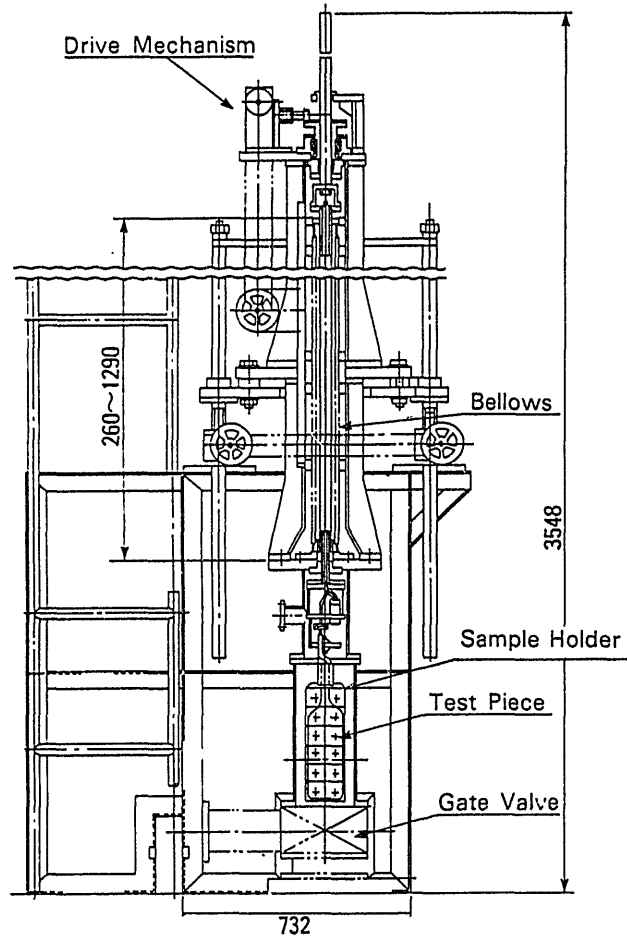


Figure 2: Lock system and drive mechanism for the insertion of materials samples into the Neutral Beam Injection Test Stand vacuum vessel

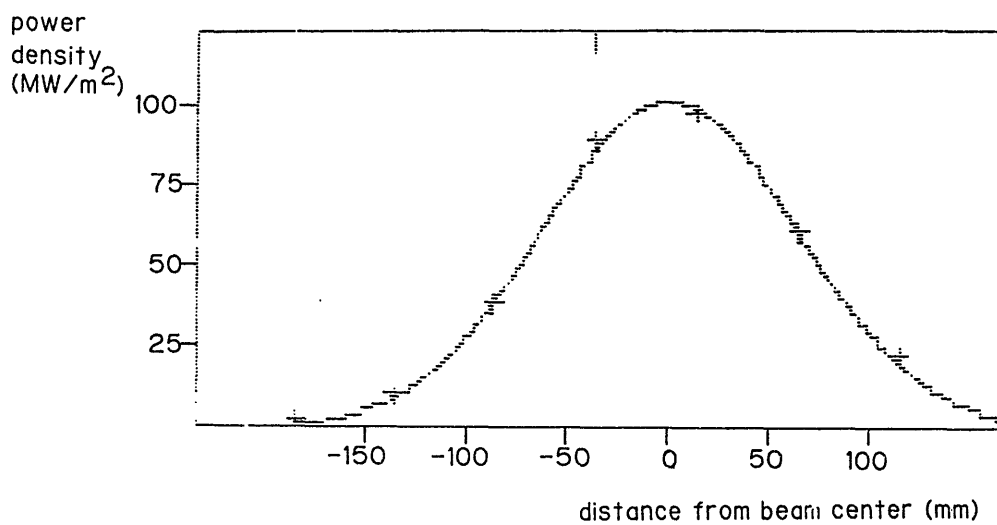


Figure 3: Power density distribution profile of the hydrogen beam

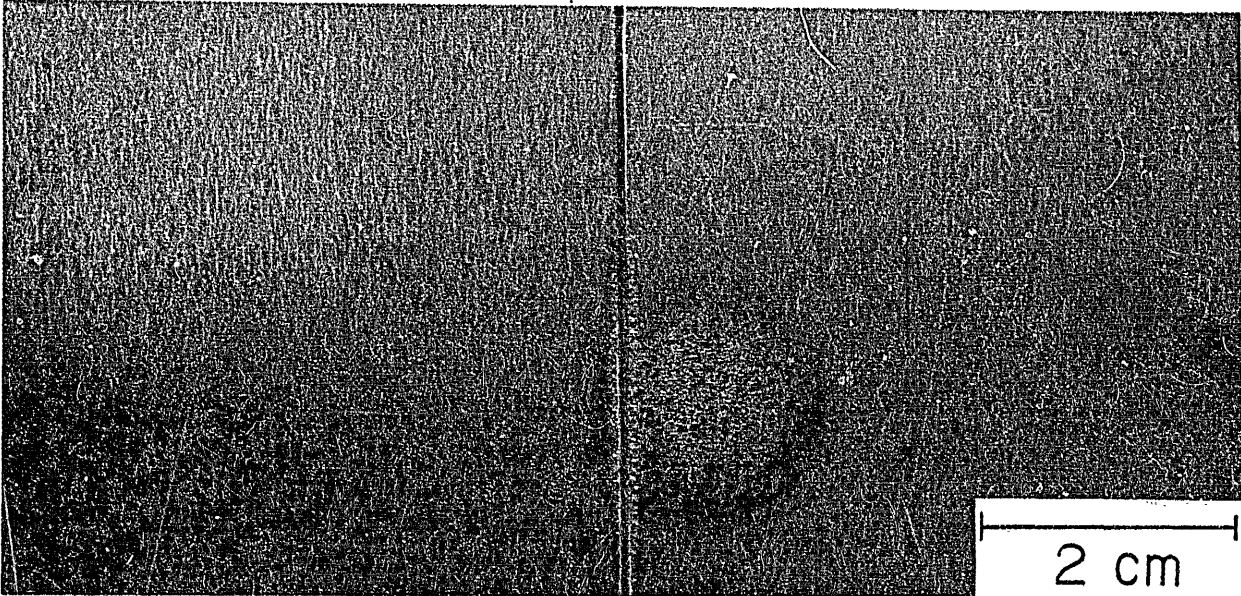


Figure 4: Stainless steel 1.4311
pulse length 50 ms, power density 70 MW/m²

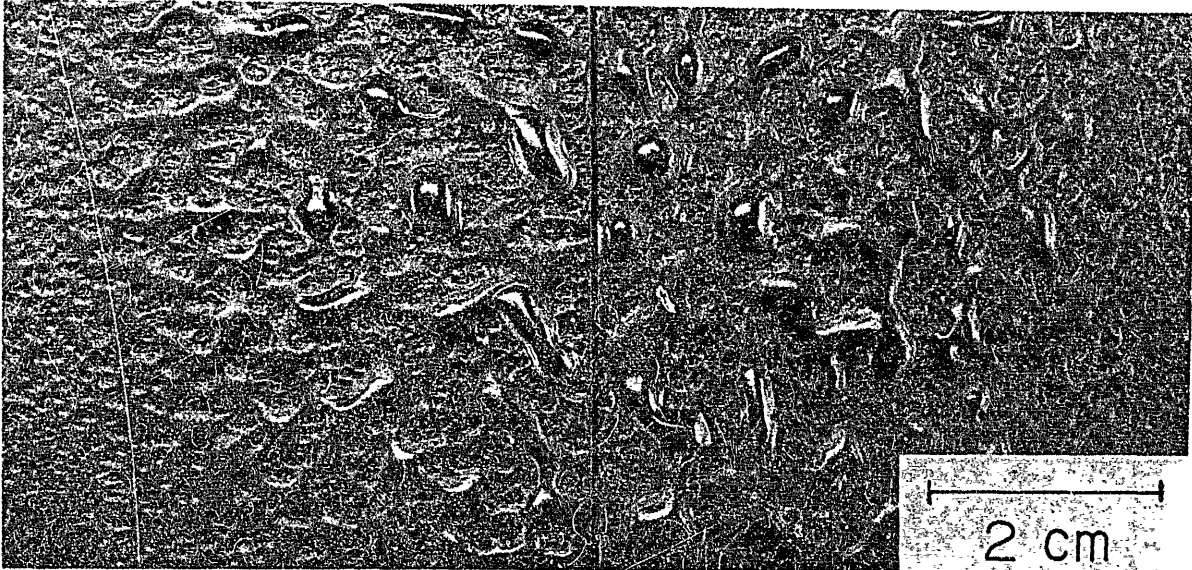


Figure 5: Stainless steel 1.4311
pulse length 951 ms, power density 16 MW/m²

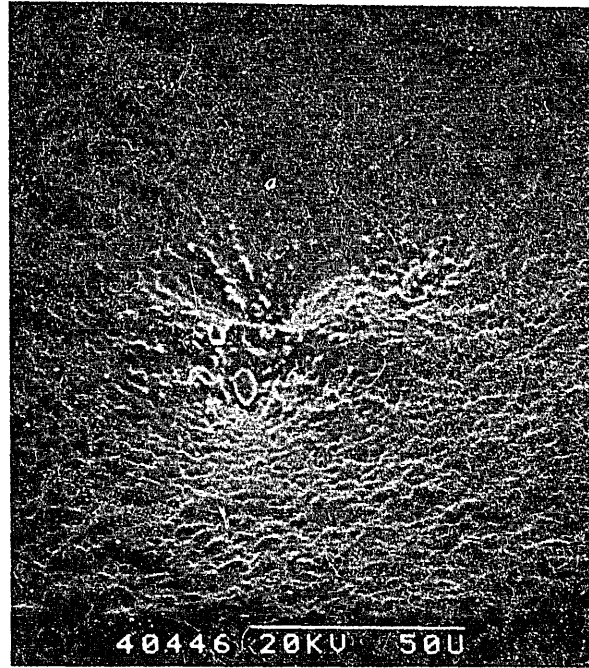
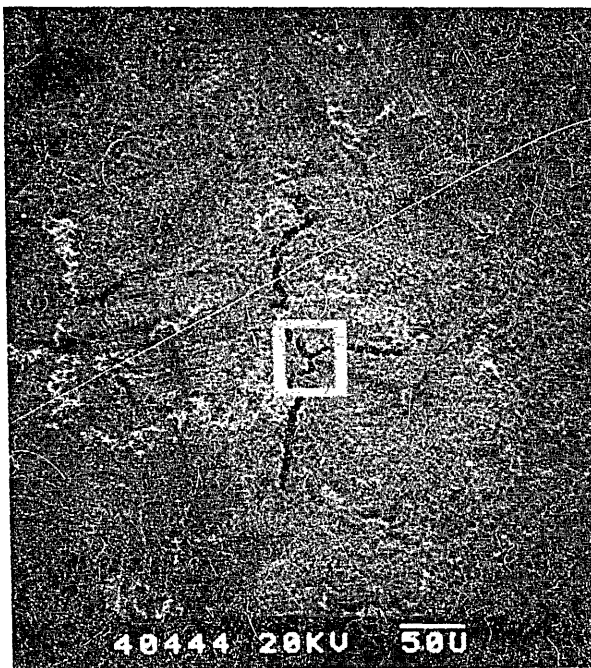
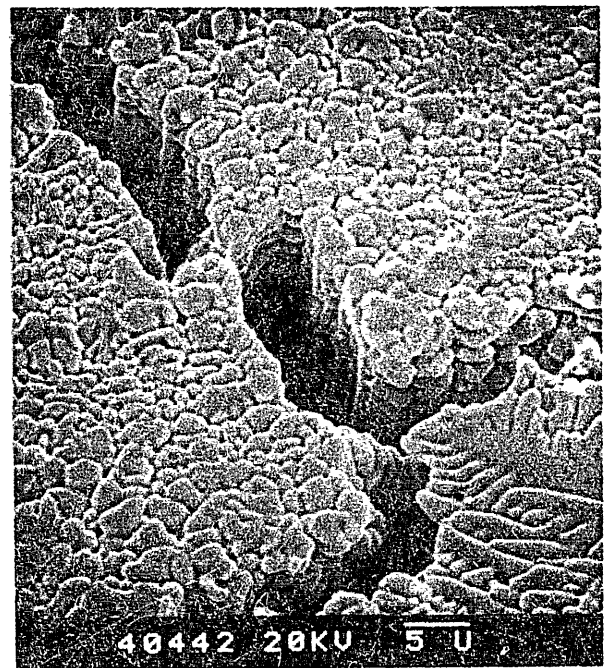


Figure 6: Stainless steel 304
pulse length 101 ms, power density 51 MW/m²

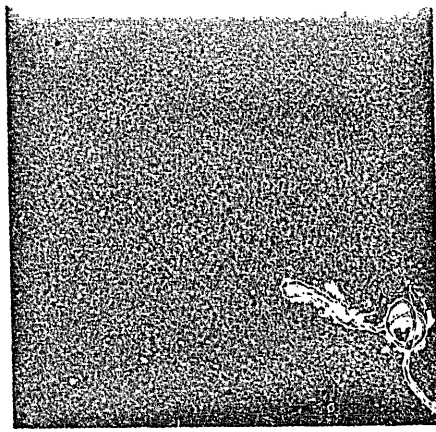


a)



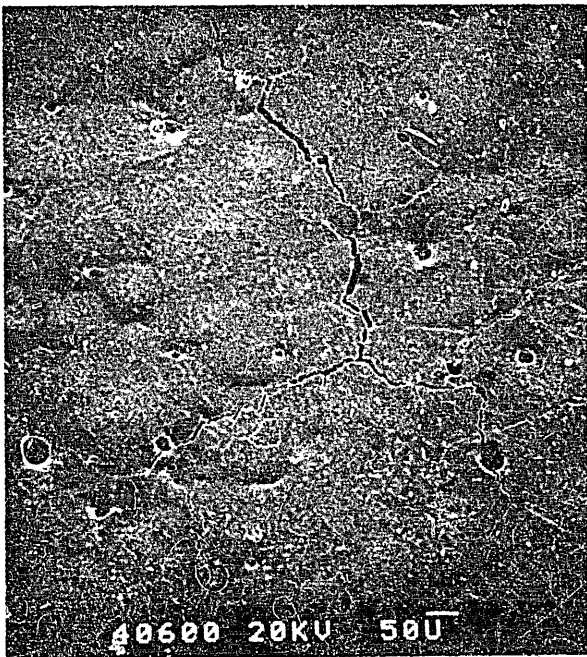
b)

Figure 7: Stainless steel 304
pulse length 101 ms, power density 60 MW/m²

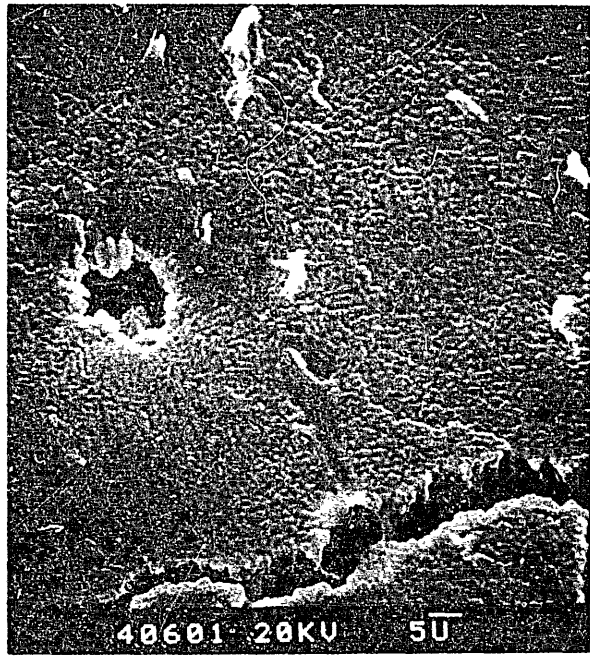


1cm

a)



b)



c)

Figure 8: Aluminium
pulse length 202 ms, power density 32 MW/m^2

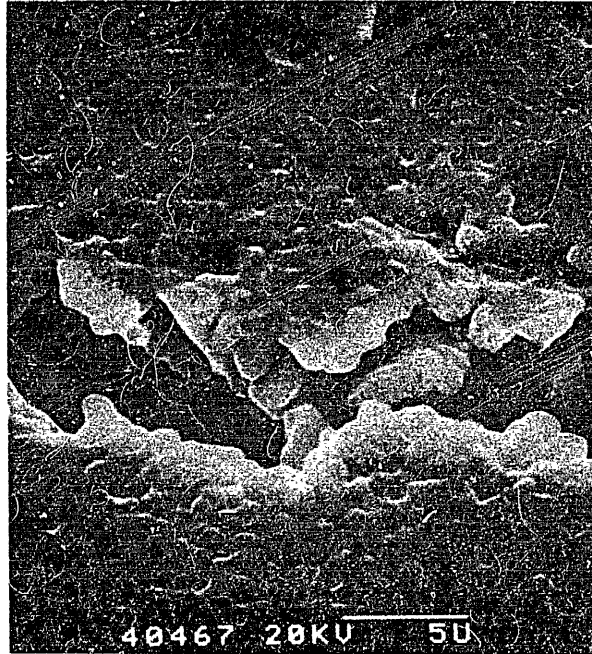
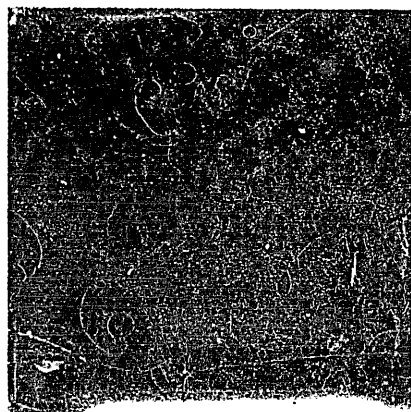
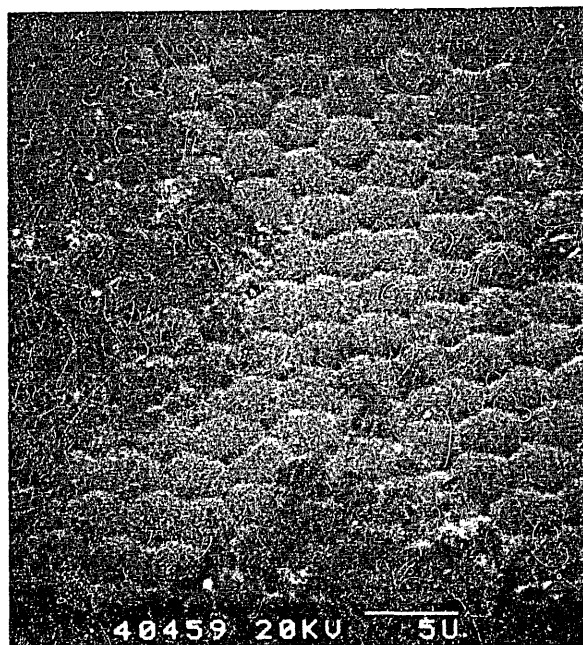


Figure 9: Aluminium
pulse length 101 ms, power density 44 MW/m^2



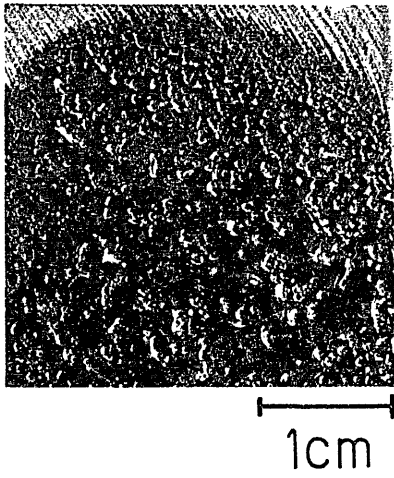
1cm

a)

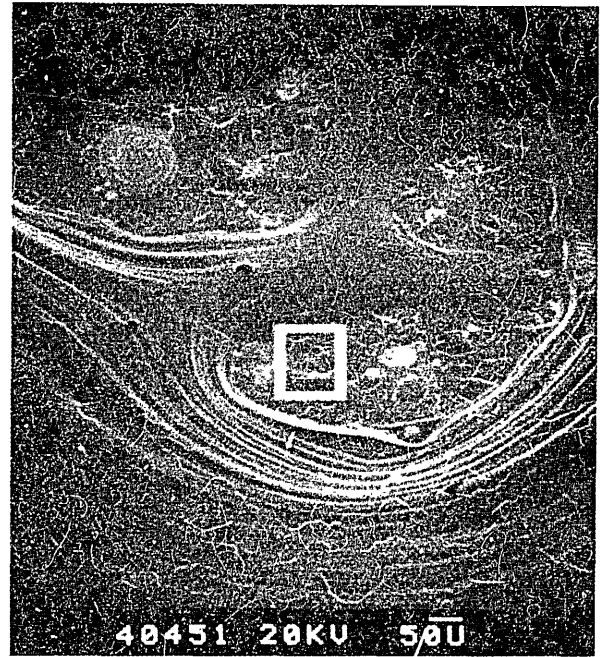


b)

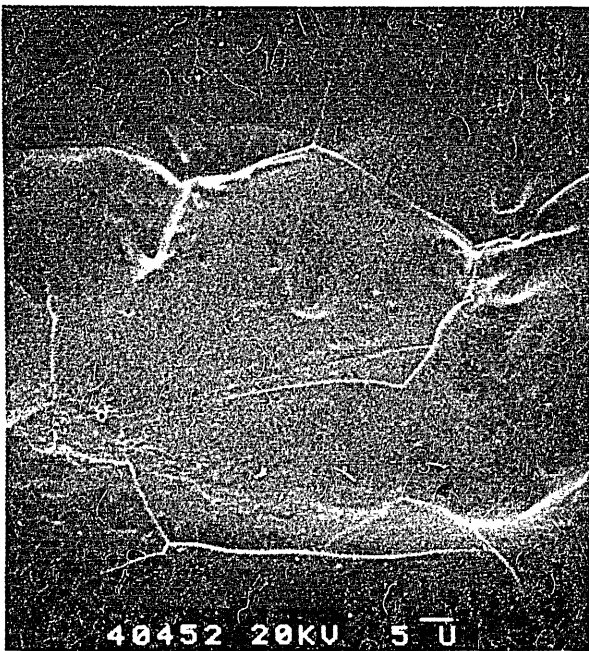
Figure 10: Copper
pulse length 208 ms, power density 94 MW/m^2



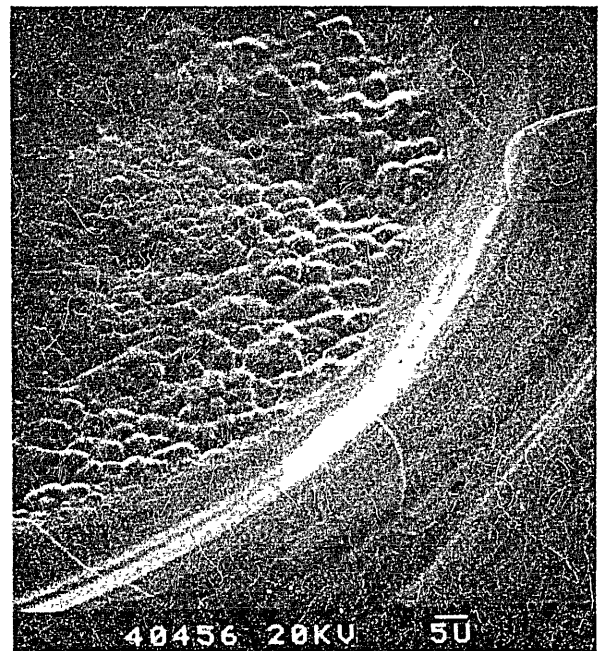
a)



b)



c)



d)

Figure 11: Molybdenum
pulse length 403 ms, power density 80 MW/m^2

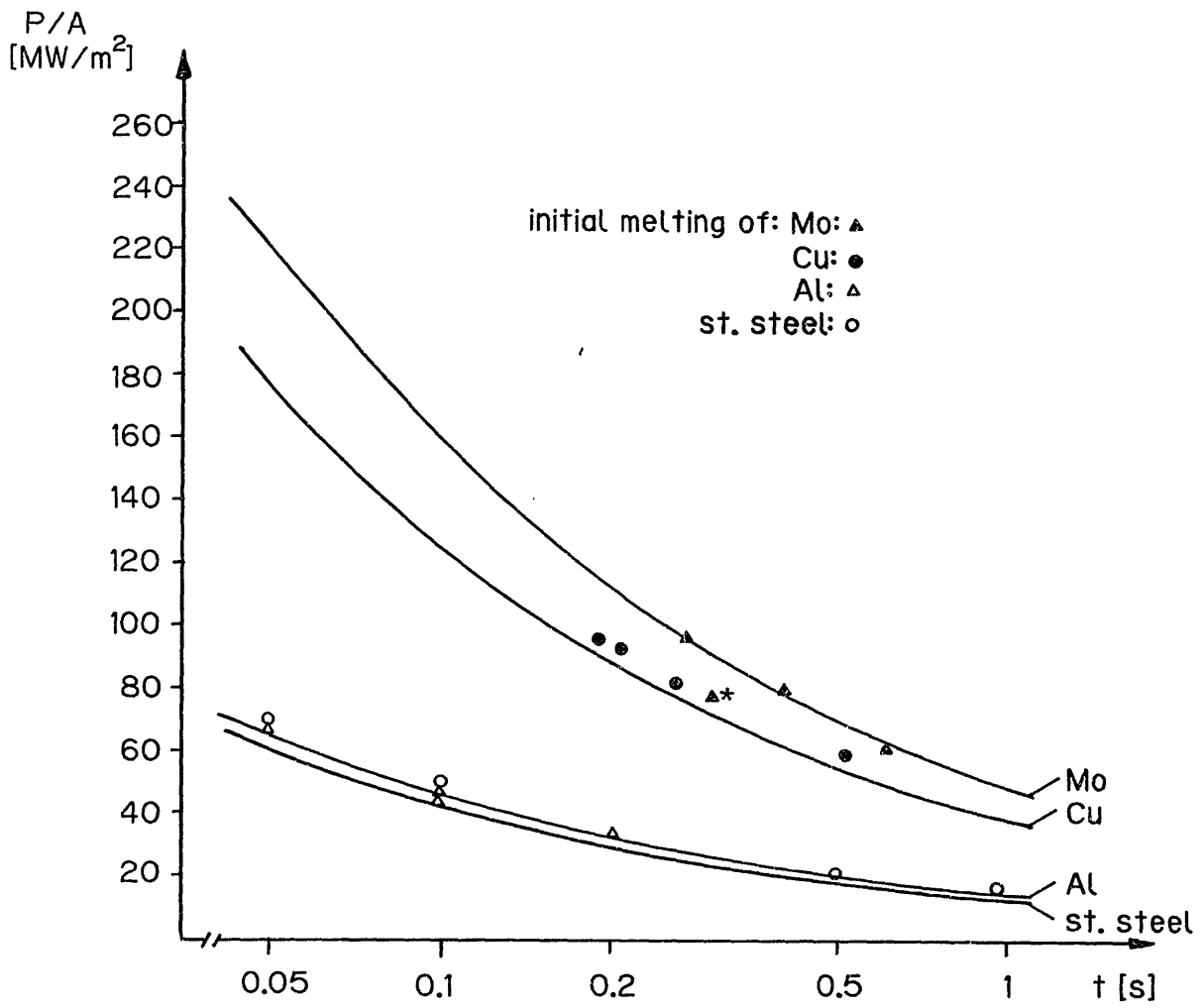


Figure 12: Melting thresholds of metals as function of power density and pulse length. Thresholds marked by full lines are based on one-dimensional calculation, points are experimental values. remark: *: preheated sample

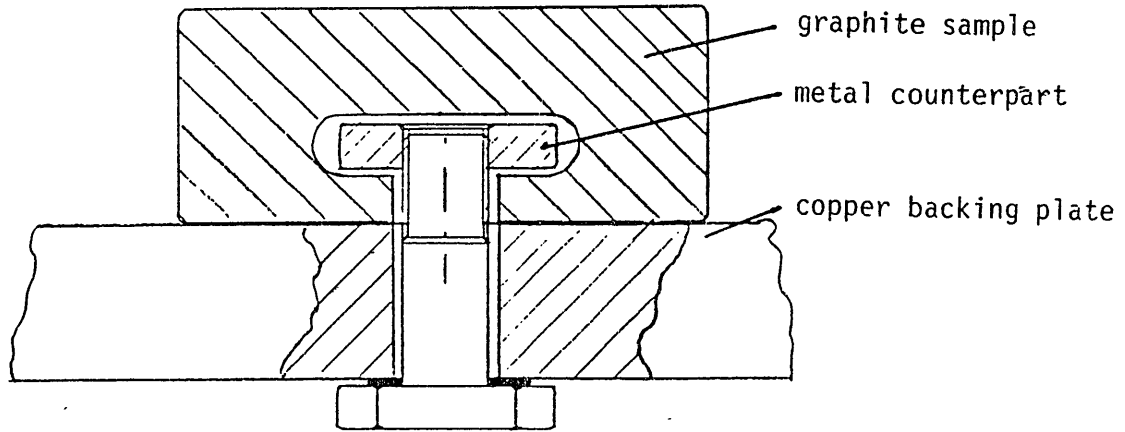


Figure 13: Attachment of graphite test piece to the sample holder (copper backing plate)

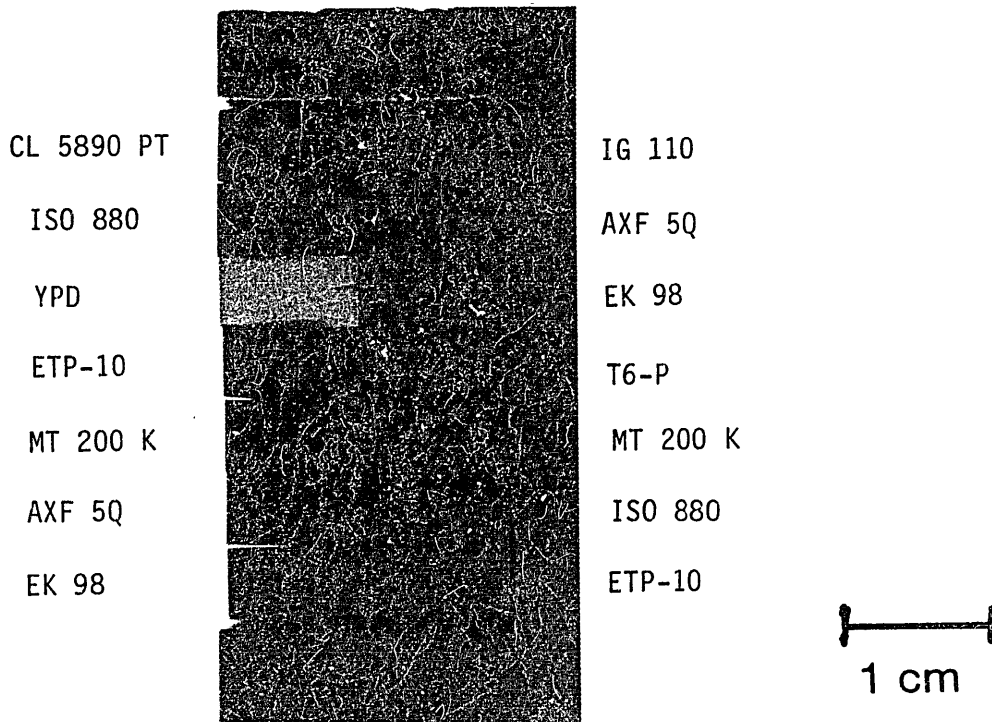
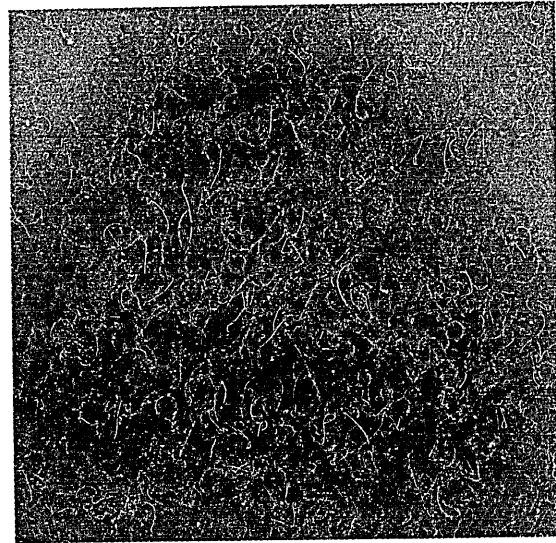
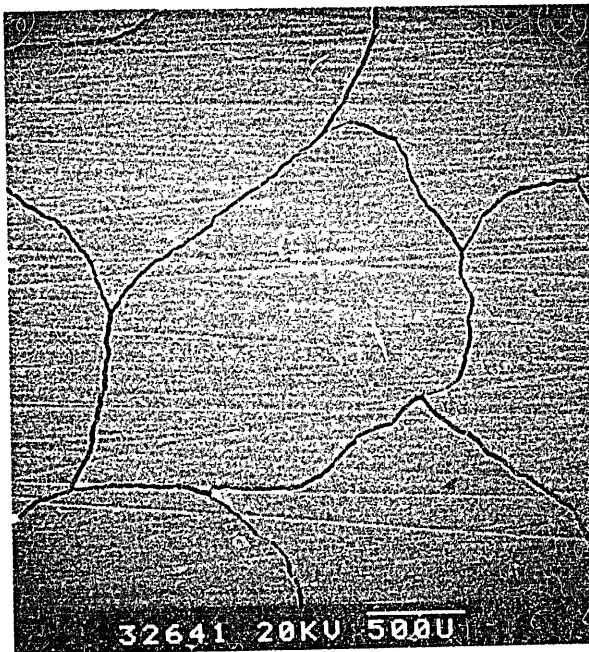


Figure 14: Screening test; small graphite samples are clamped together for beam exposure in the same experiment

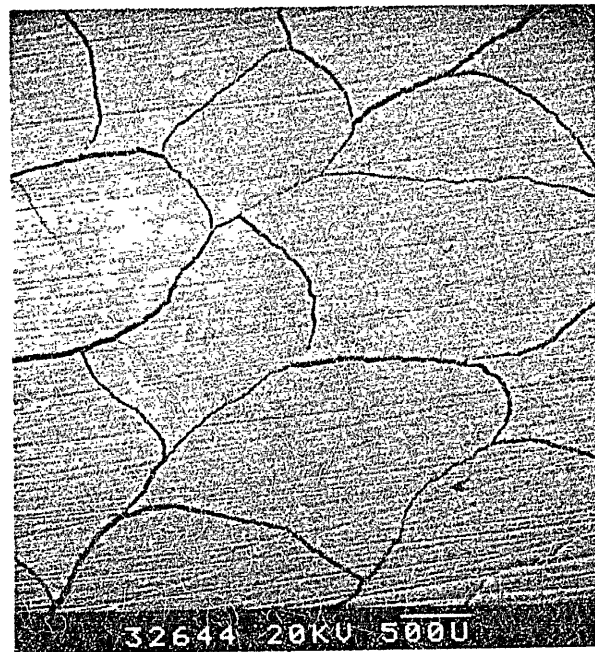
three pulses:	pulse length	power density
	227 ms	94 MW/m ²
	170 ms	94 MW/m ²
	195 ms	102 MW/m ²



a)



b)



c)

Figure 15: Cracks on the surface of ZXF-5Q
pulse length 290 ms, power density 97 MW/m^2

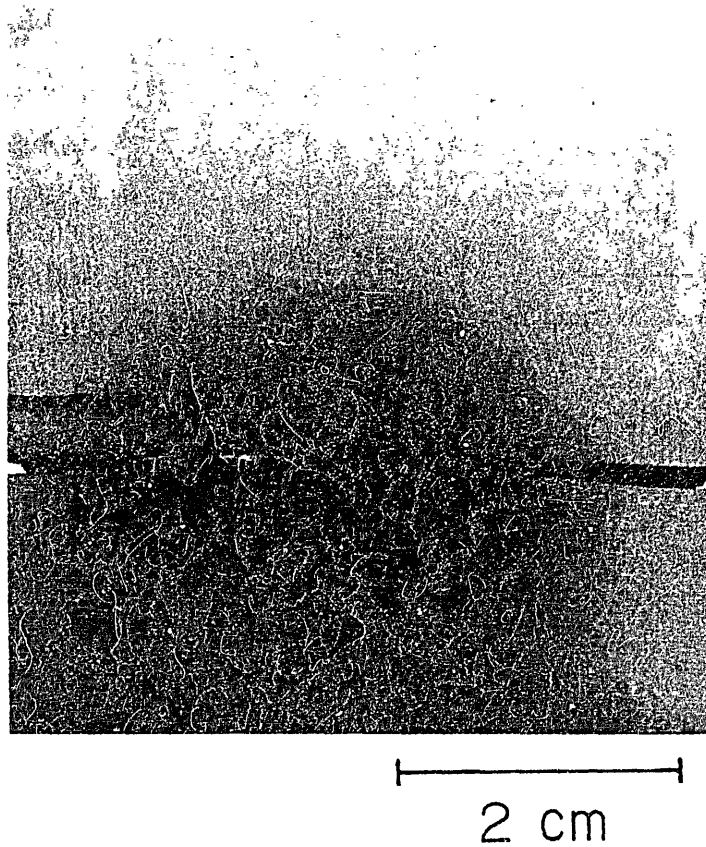
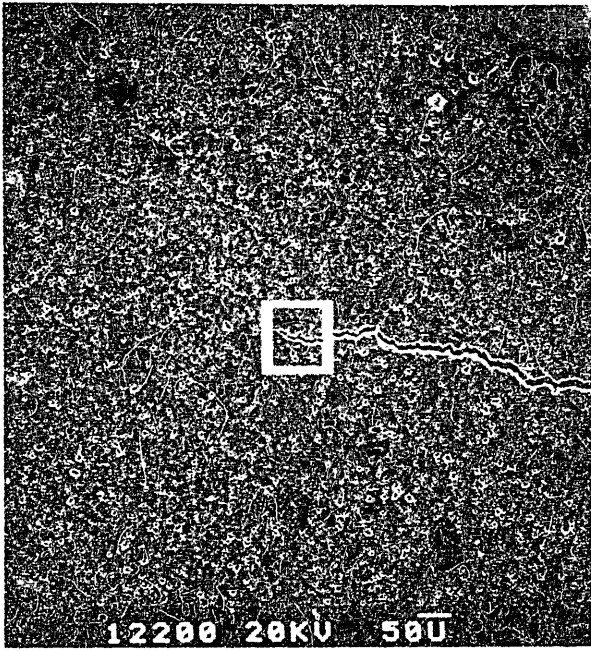
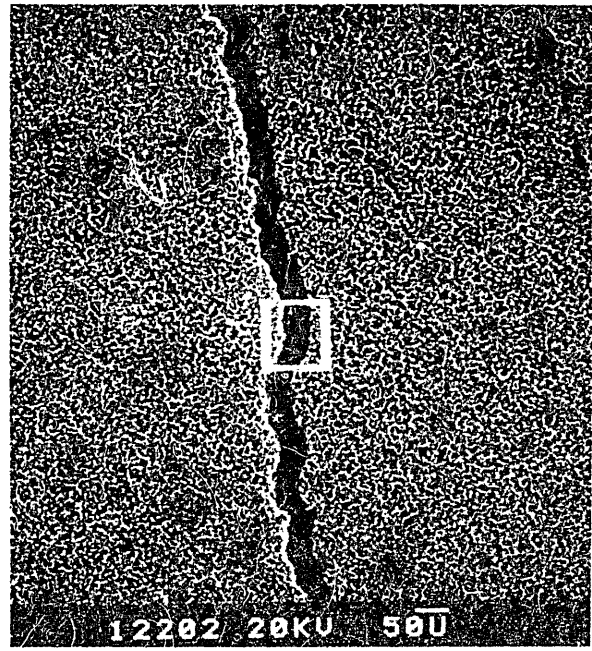


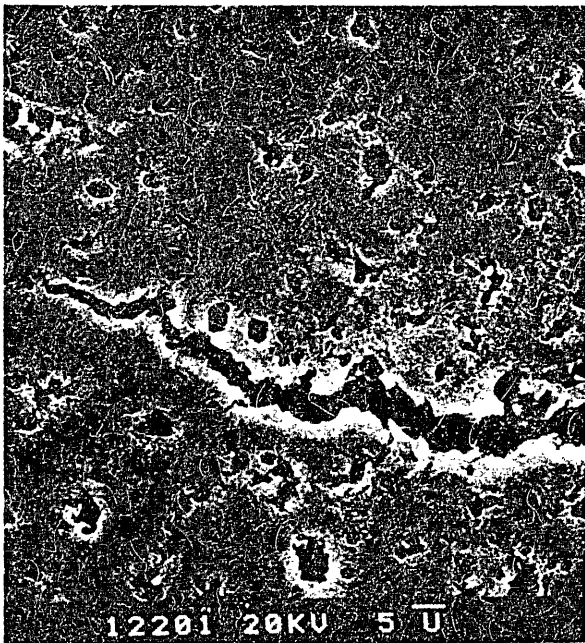
Figure 16: Fracture of YPD
pulse length 309 ms, power density 96 MW/m^2



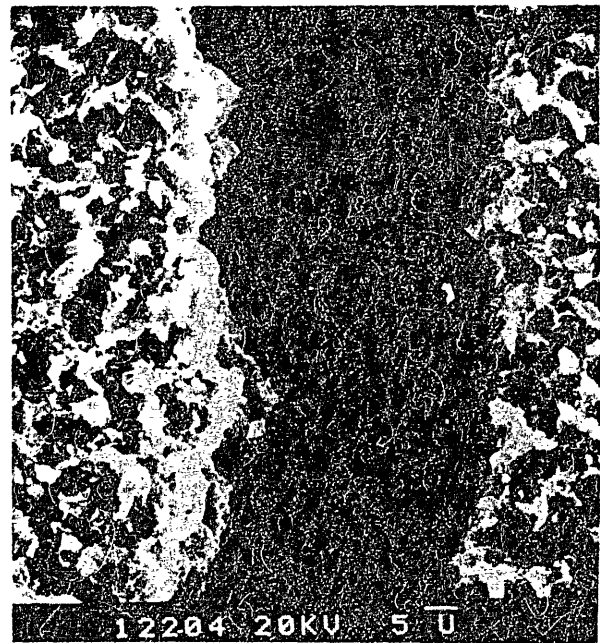
a)



b)



c)

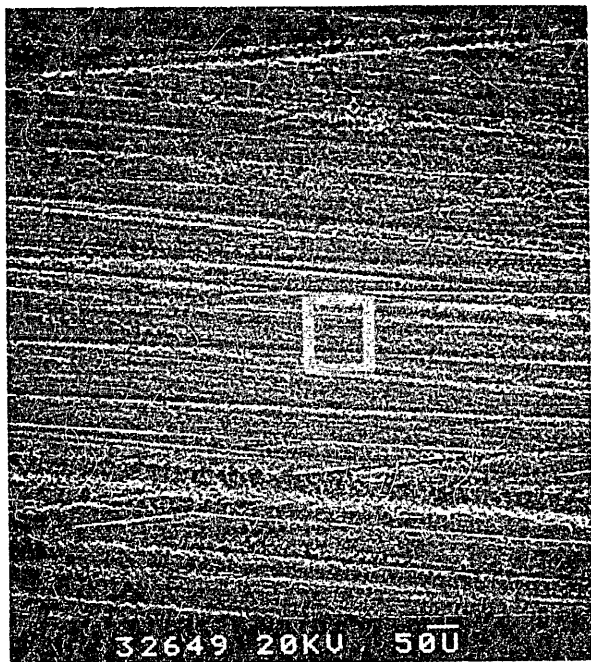


d)

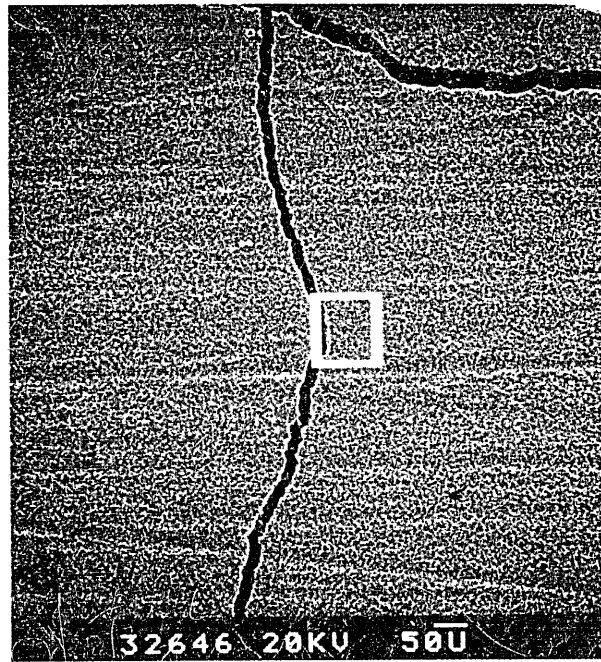
slightly eroded

heavily eroded

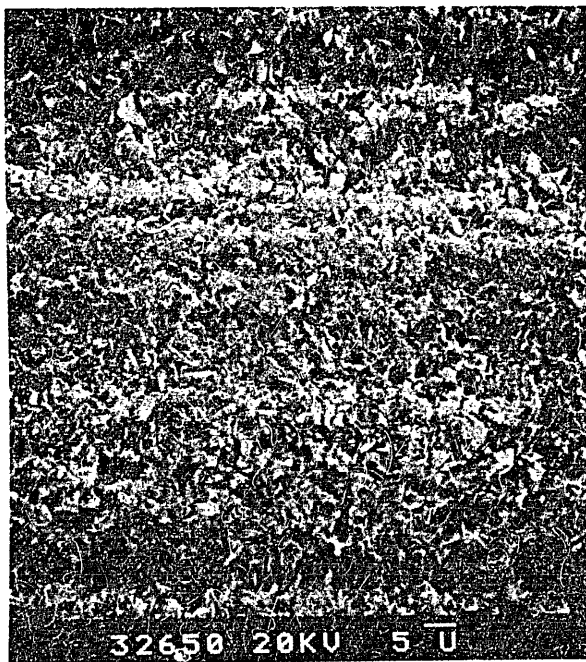
Figure 17 a) - d): Poco AXF-5Q
pulse length 233 ms, power density 92 MW/m^2



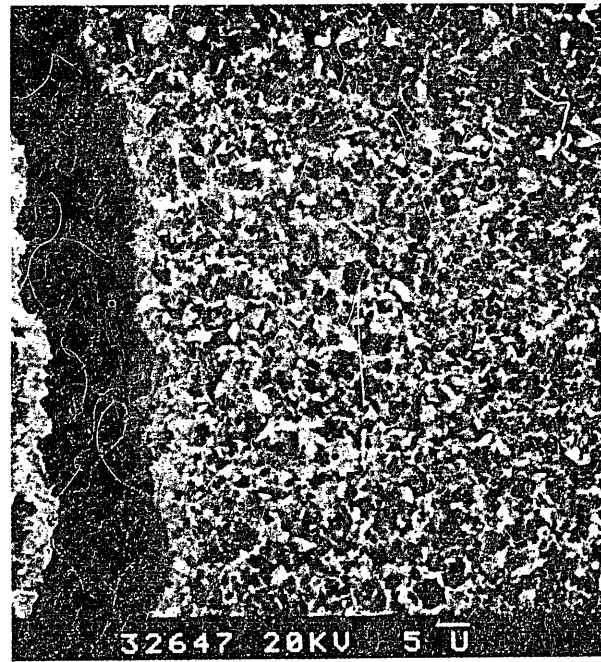
a)



b)



c)

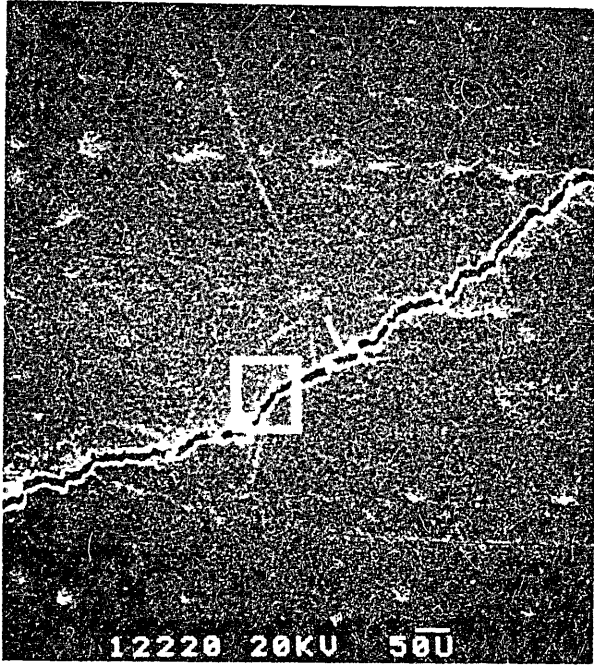


d)

slightly eroded

heavily eroded

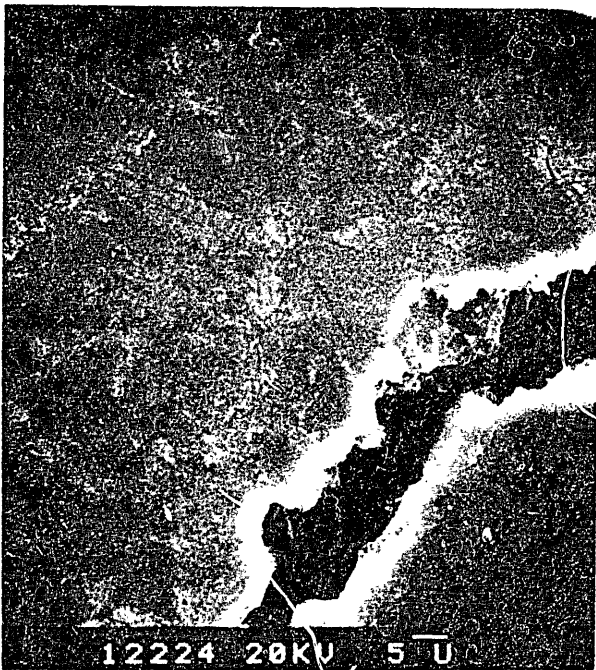
Figure 18 a) - d): Poco ZXF-5Q
pulse length 290 ms, power density 97 MW/m^2



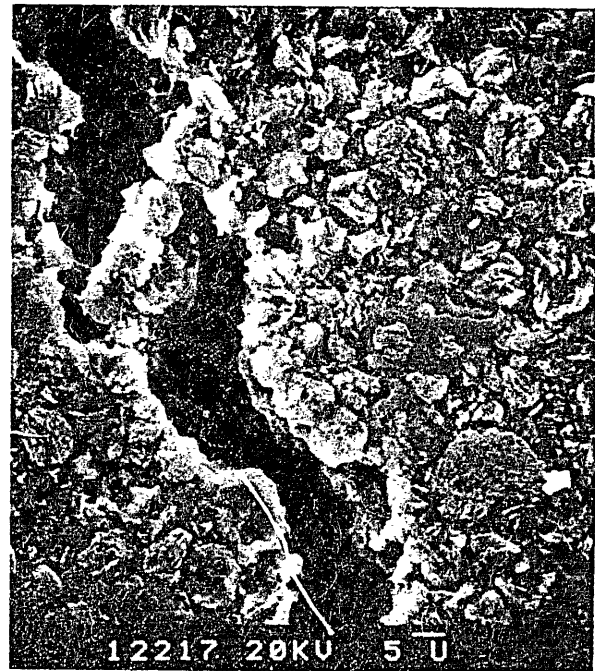
a)



b)



c)



d)

slightly eroded

heavily eroded

Figure 19 a) - d): Toyo Tanso ISO 880
pulse length 214 ms, power density 93 MW/m^2

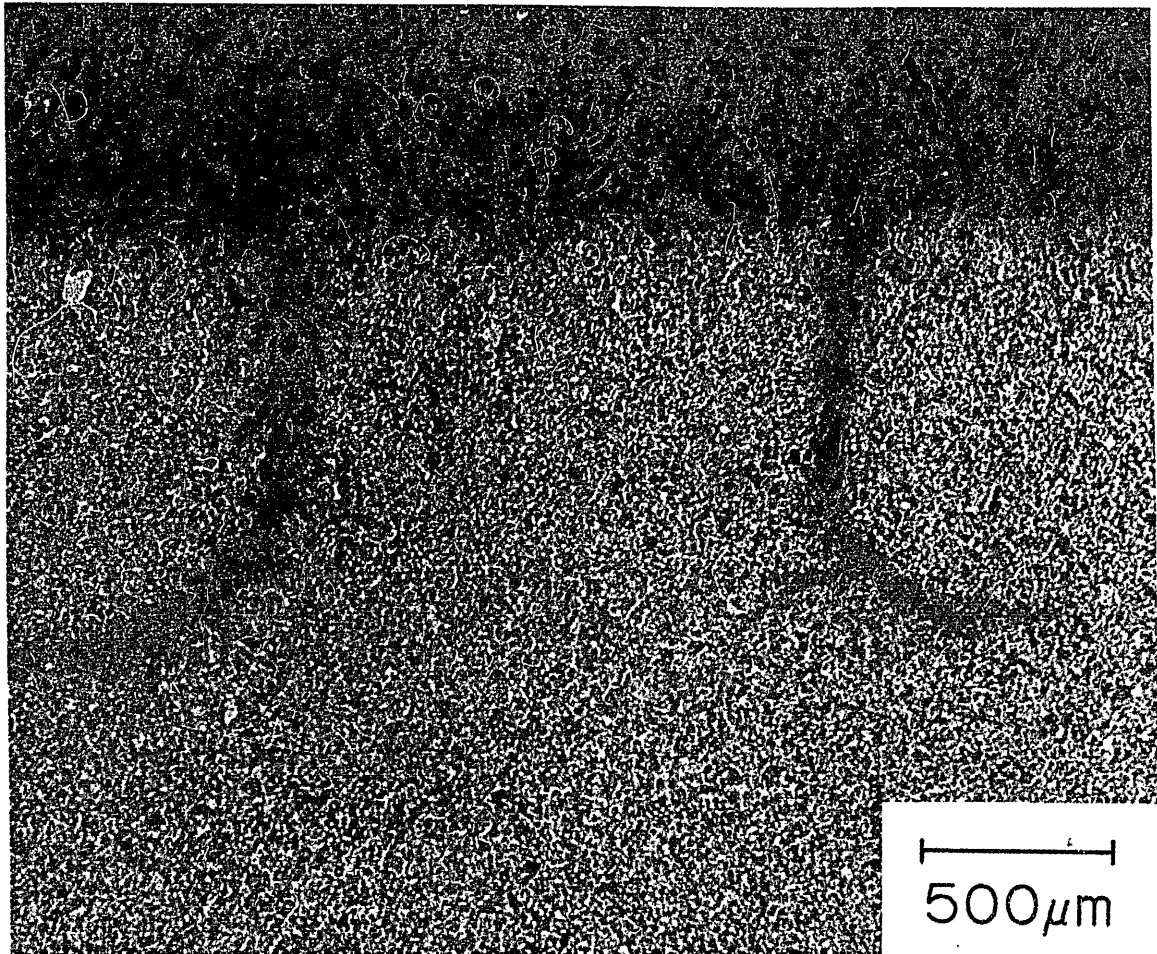
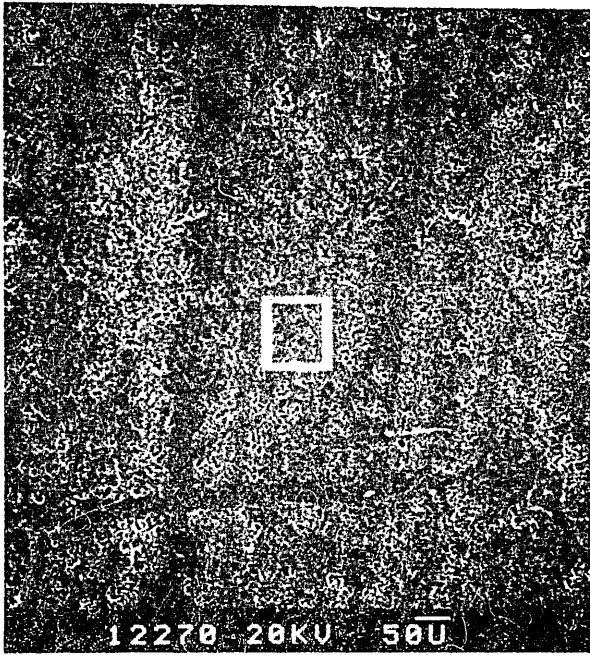
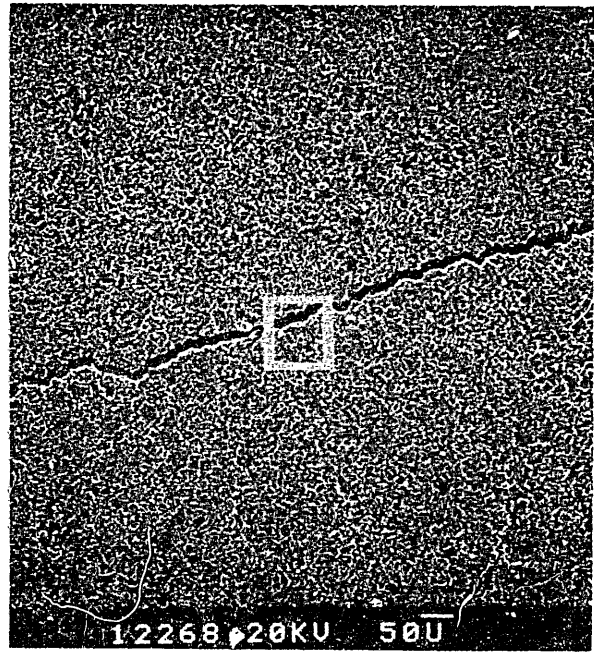


Figure 20: Toyo Tanso ISO 880, cross section
pulse length 214 ms, power density 93 MW/m²



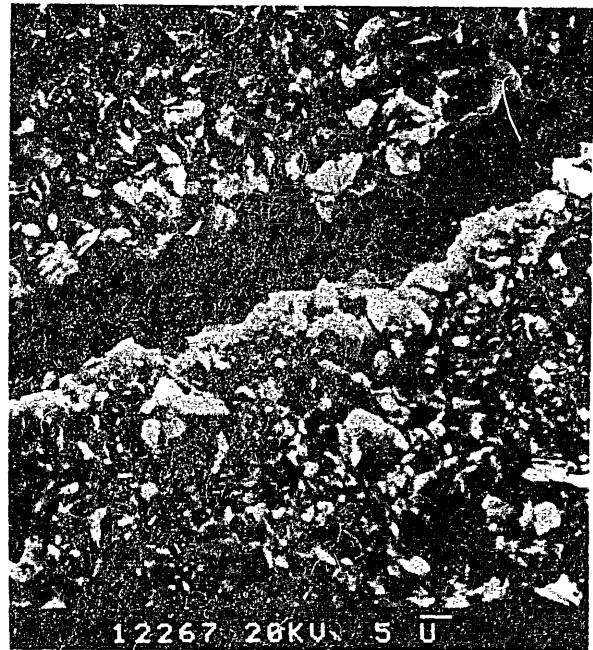
a)



b)



c)

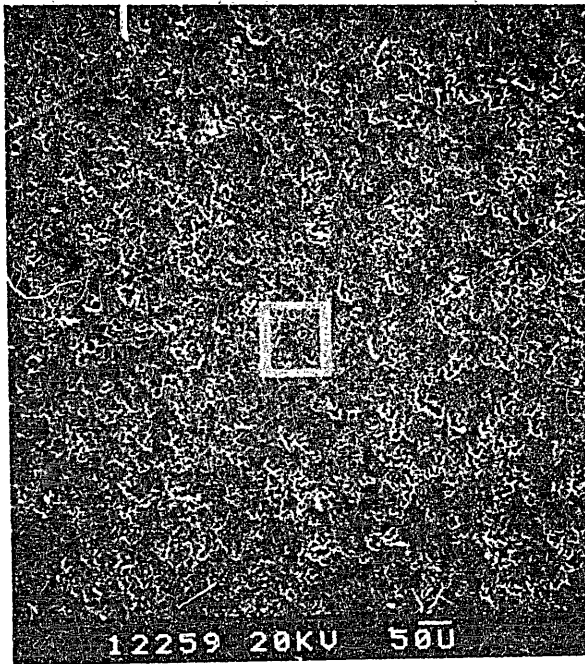


d)

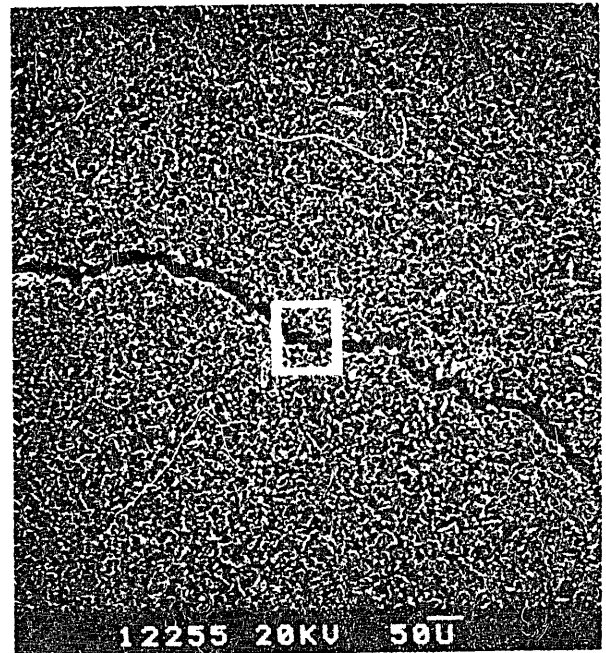
slightly eroded

heavily eroded

Figure 21 a) - d): Ibidem T6-P
pulse length 164 ms, power density 96 MW/m^2



a)



b)



c)



d)

slightly eroded

heavily eroded

Figure 22 a) - d): Toyo Carbon MT 200 K
pulse length 183 ms, power density 93 MW/m^2

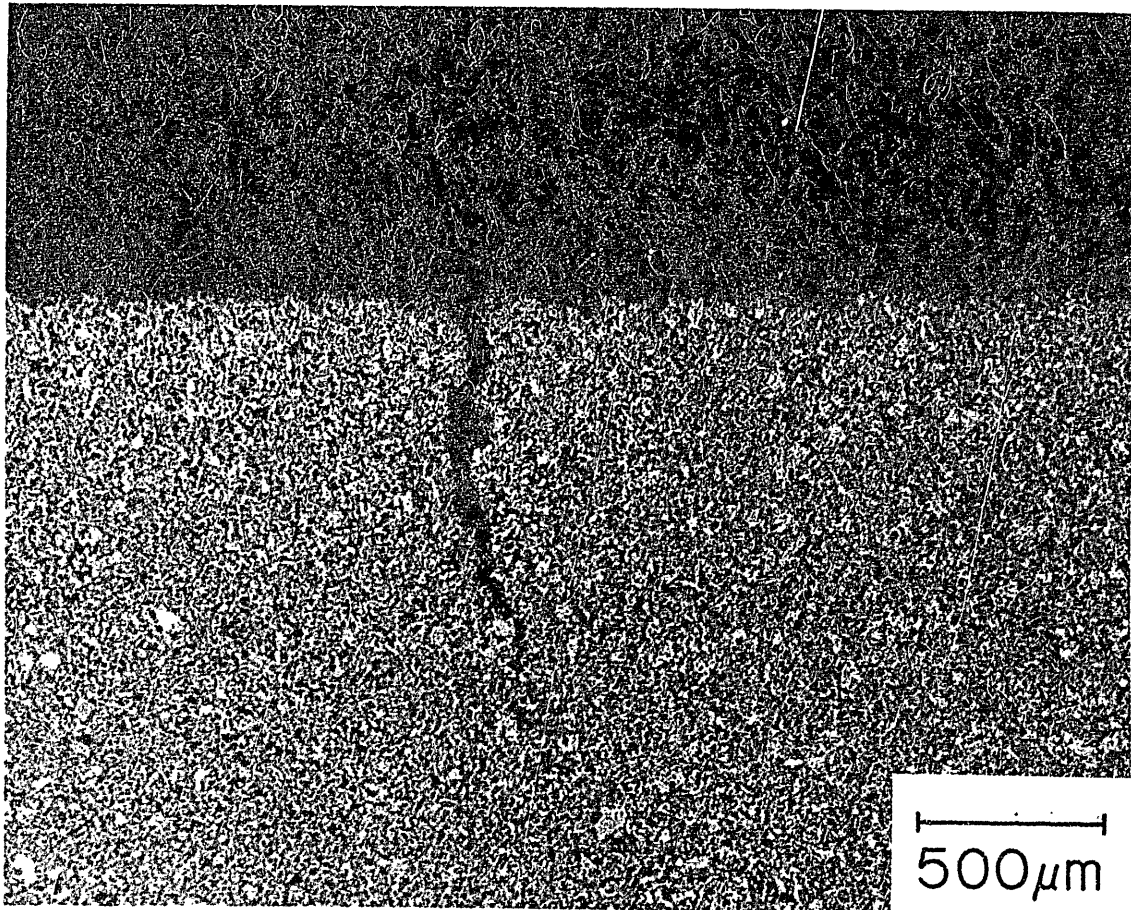
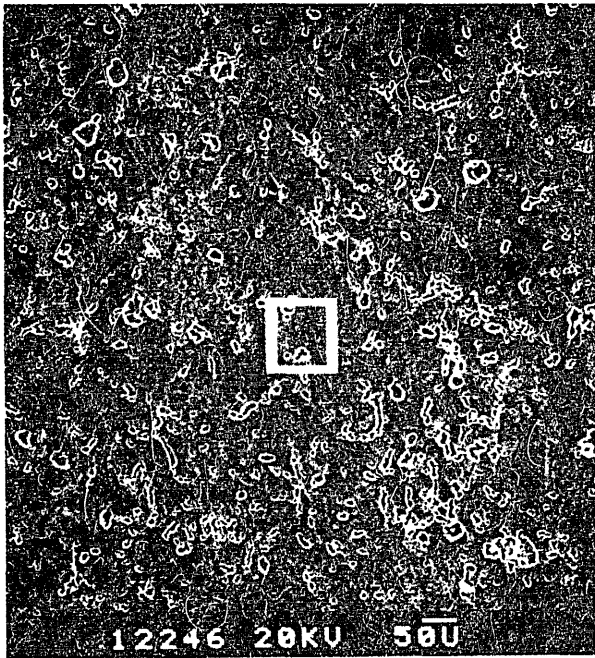
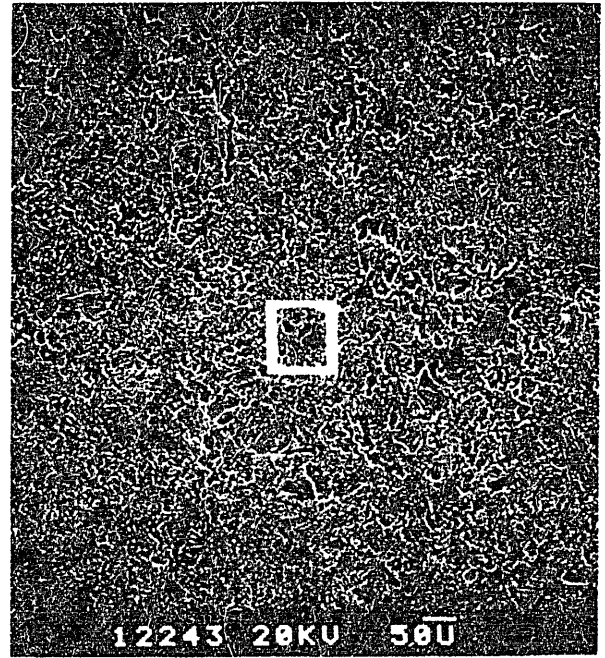


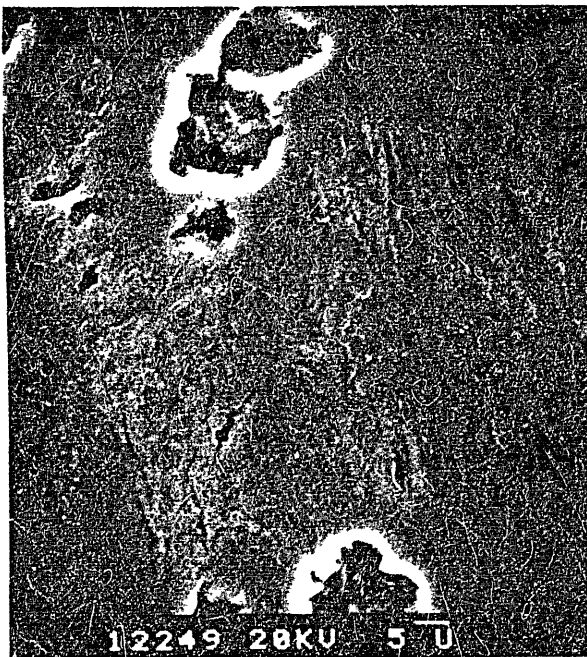
Figure 23: Toyo Carbon MT 200 K, cross section
pulse length 183 ms, power density 93 MW/m^2



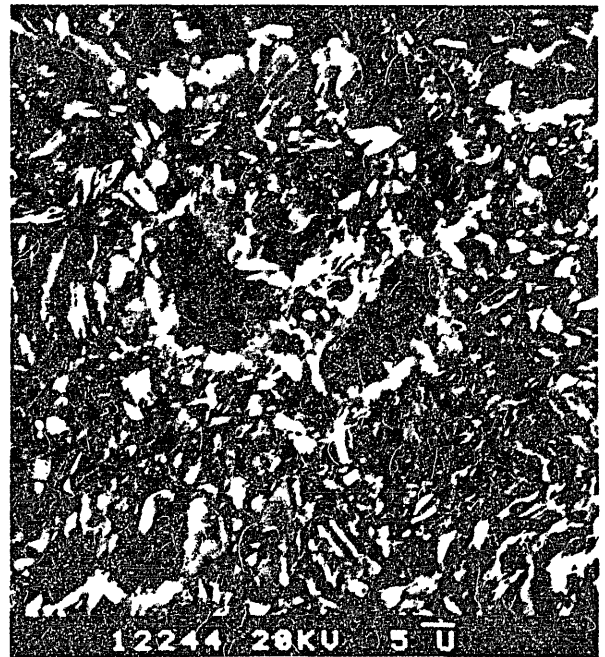
a)



b)



c)



d)

slightly eroded

heavily eroded

Figure 24 a) - d): Carbone Lorraine CL 5890 PT
pulse length 221 ms, power density 94 MW/m^2

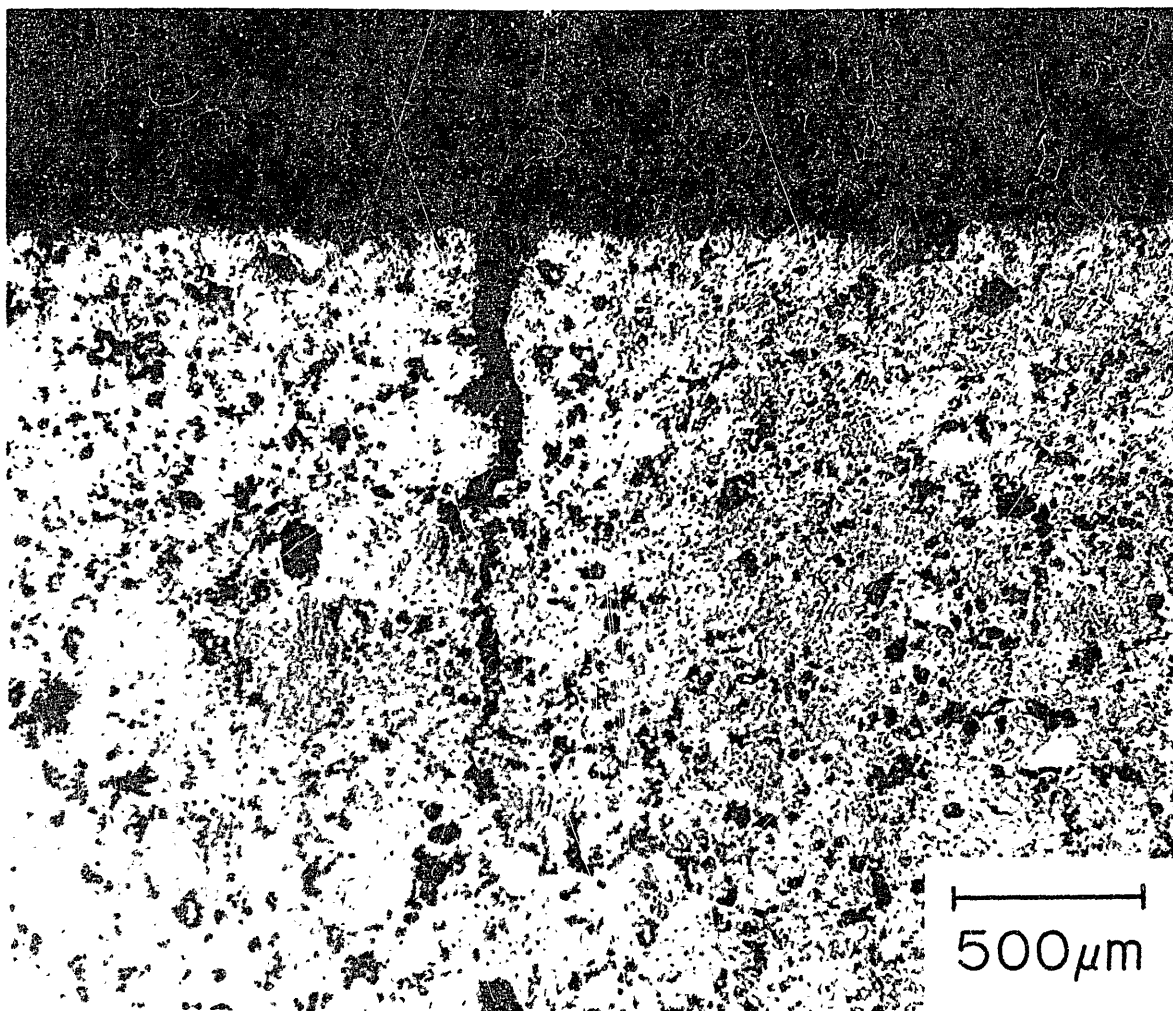
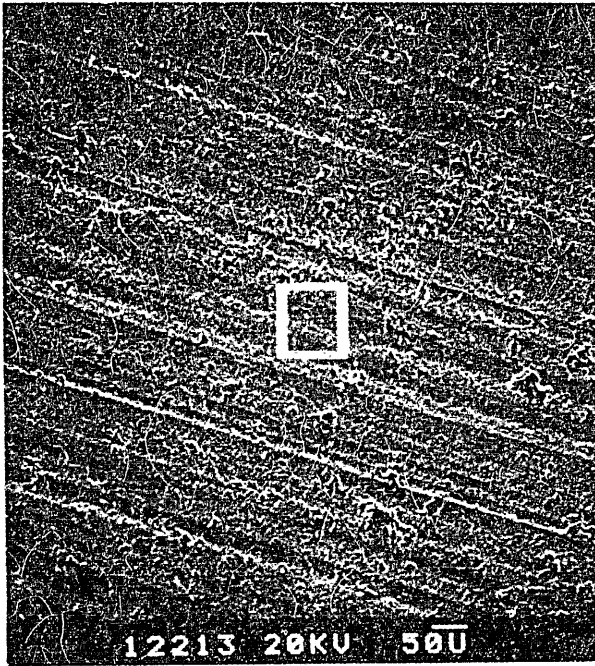
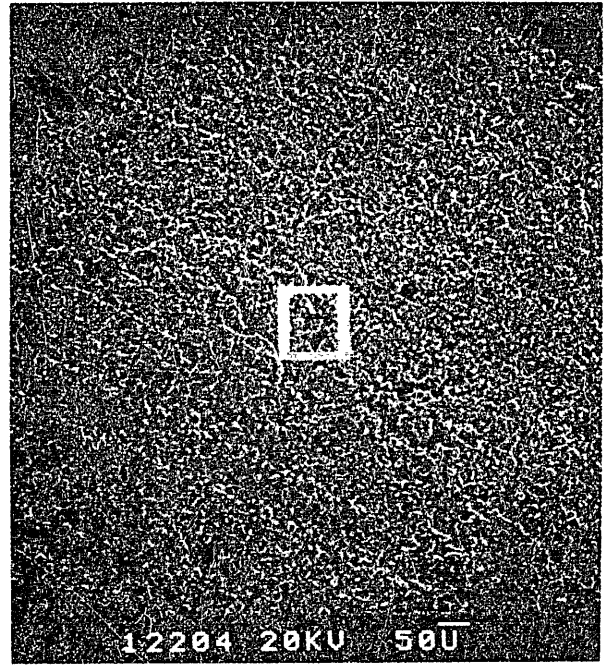


Figure 25: Carbone Lorraine CL 5890 PT, cross section
pulse length 221 ms, power density 94 MW/m^2



a)



b)



c)



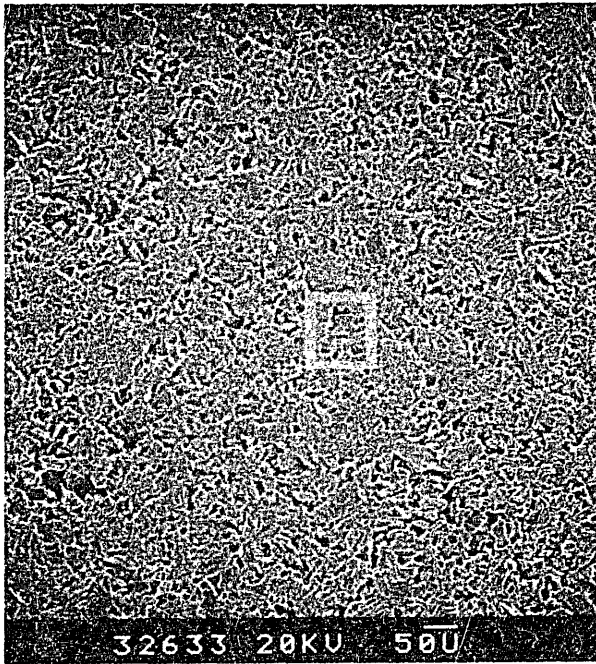
d)

slightly eroded

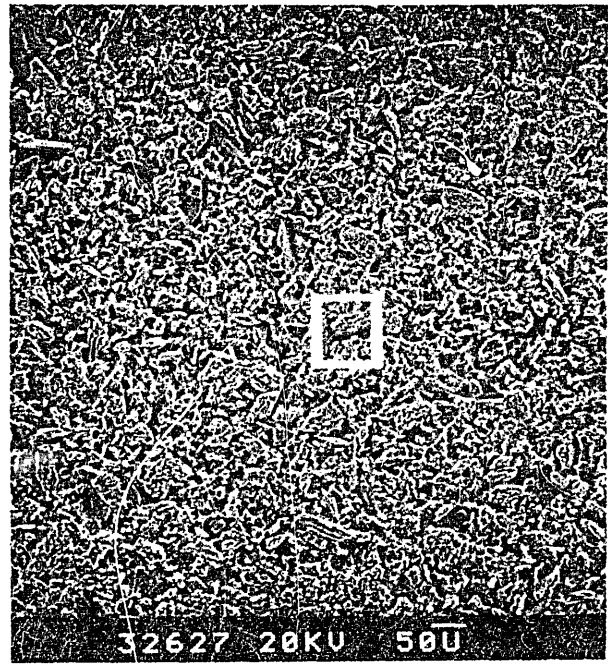
heavily eroded

Figure 26 a) - d): Ringsdorff EK 98

pulse length 176 ms, power density 98 MW/m^2



a)



b)



c)

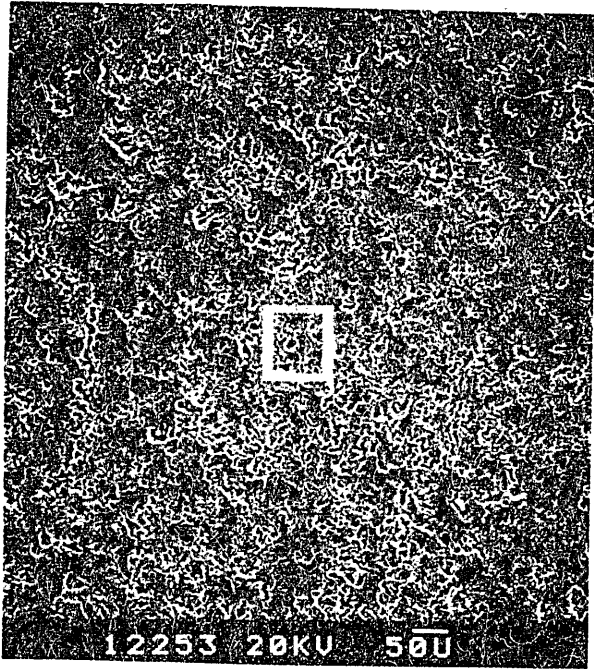


d)

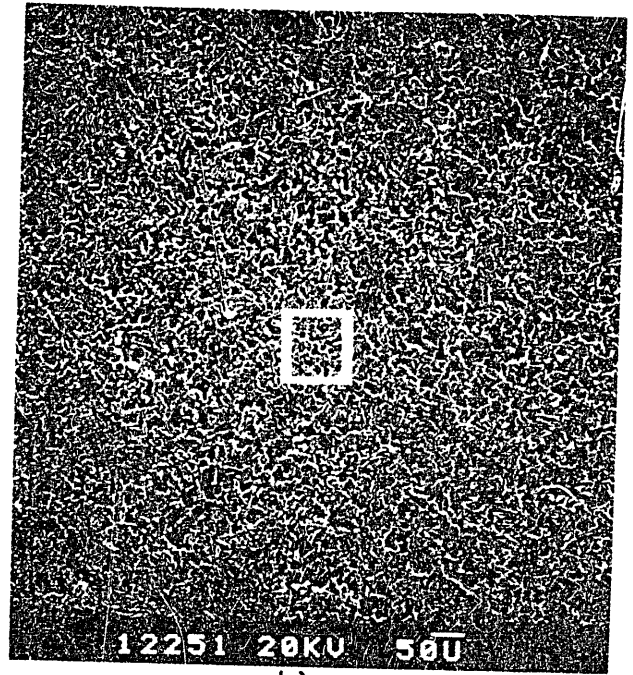
slightly eroded

heavily eroded

Figure 27 a) - d): Schunk Kohlenstofftechnik FE 219
pulse length 221 ms, power density 97 MW/m^2



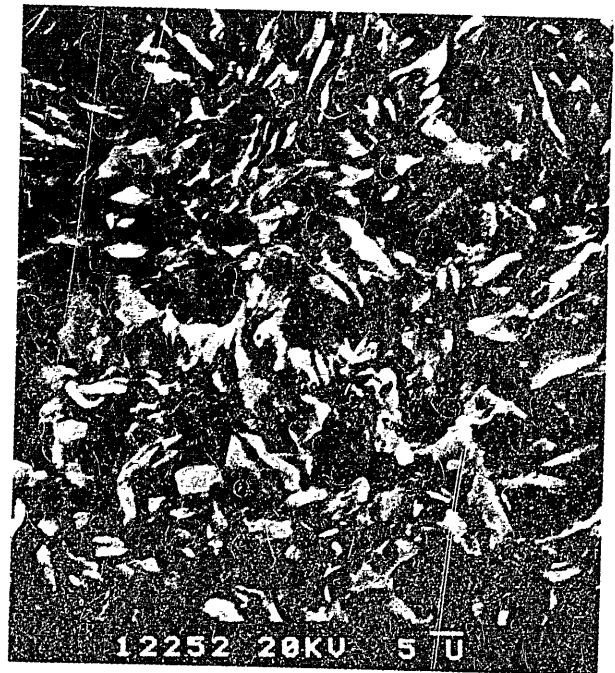
a)



b)



c)



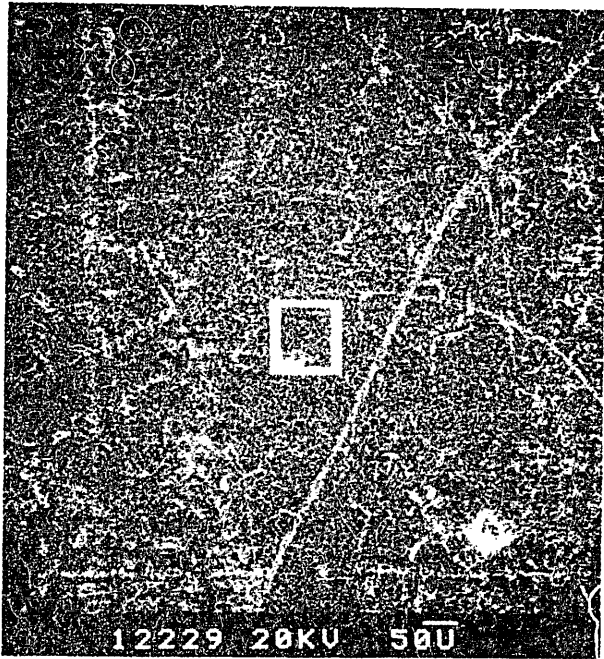
d)

slightly eroded

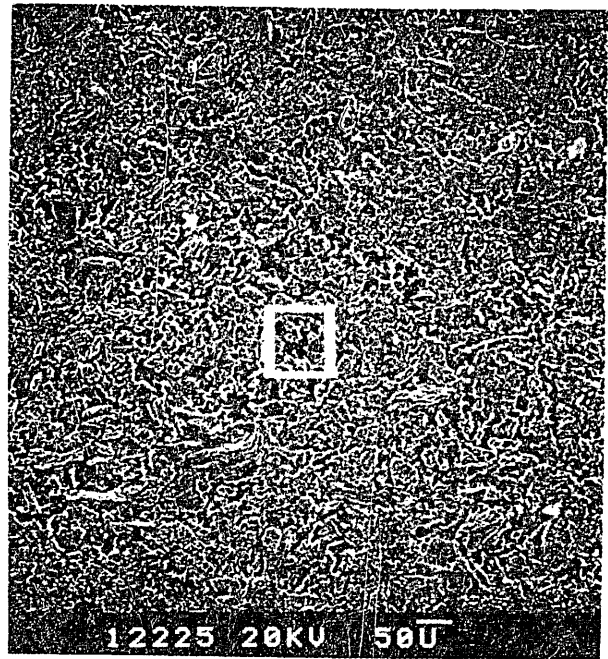
heavily eroded

Figure 28 a) - d): Ibidem ETP-10

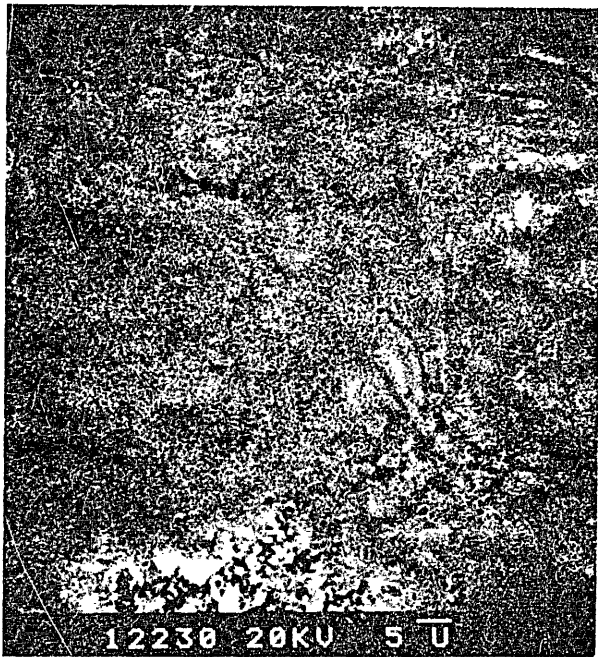
pulse length 195 ms, power density 91 MW/m^2



a)



b)



c)

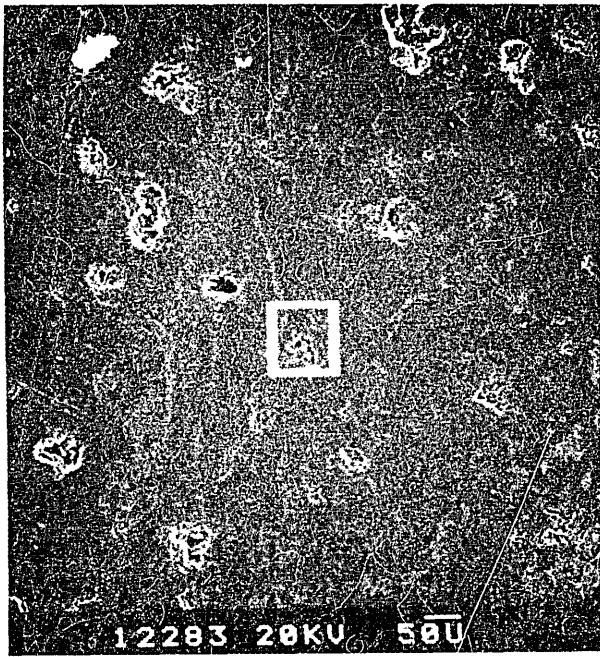


d)

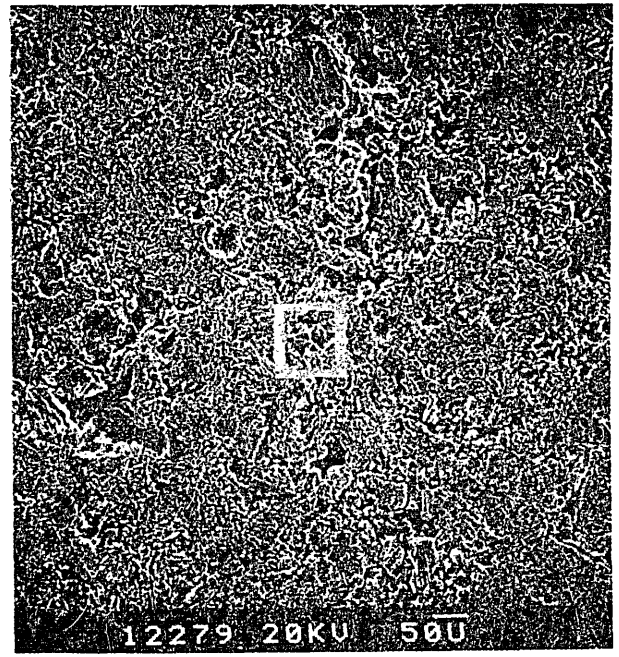
slightly eroded

heavily eroded

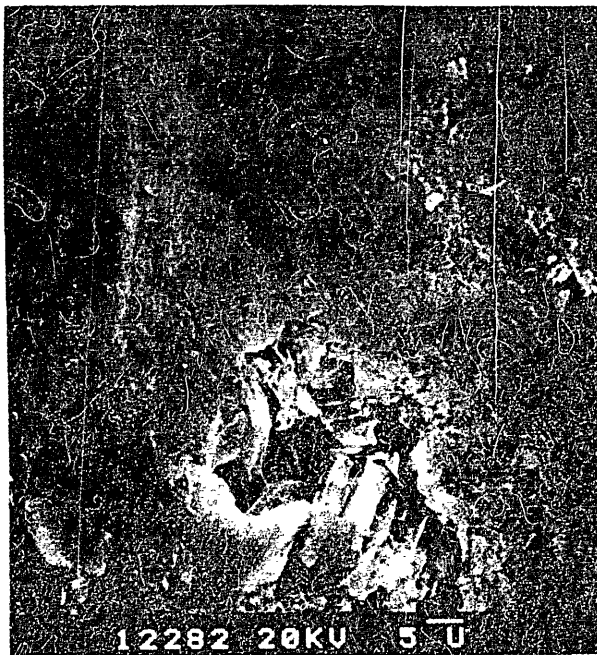
Figure 29a) - d): Toyo Tanso IG 110
pulse length 214 ms, power density 94 MW/m^2



a)



b)



c)



d)

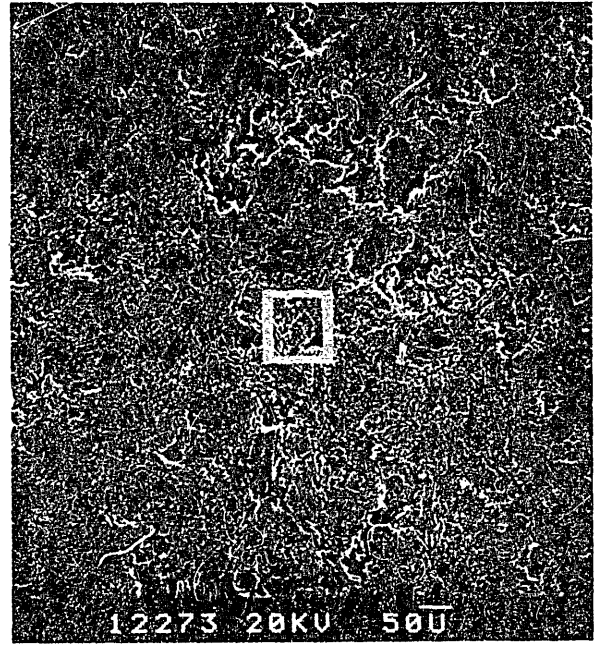
slightly eroded

heavily eroded

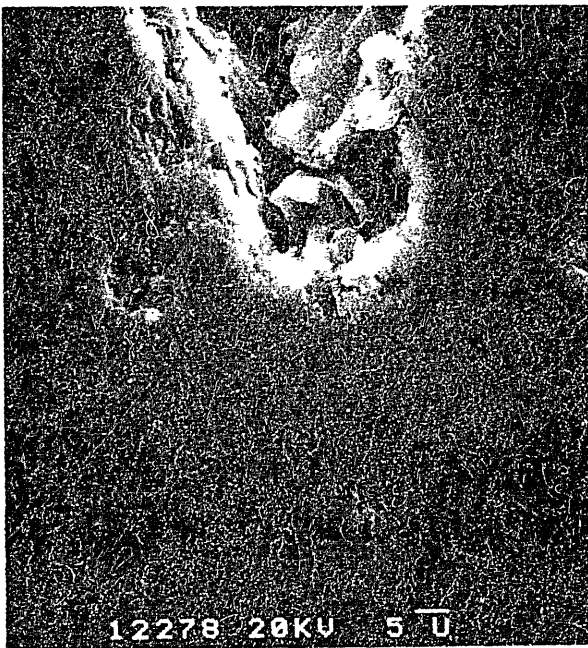
Figure 30 a) - d): Union Carbide ATJ
pulse length 221 ms, power density 96 MW/m^2



a)



b)



c)



d)

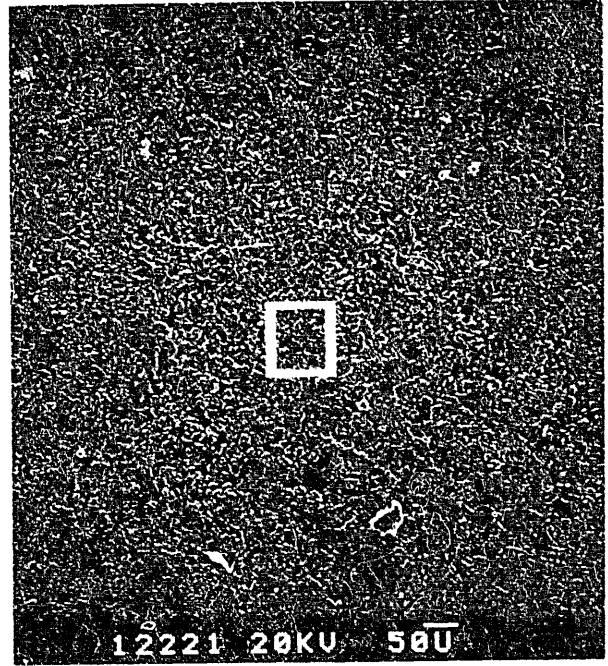
slightly eroded

heavily eroded

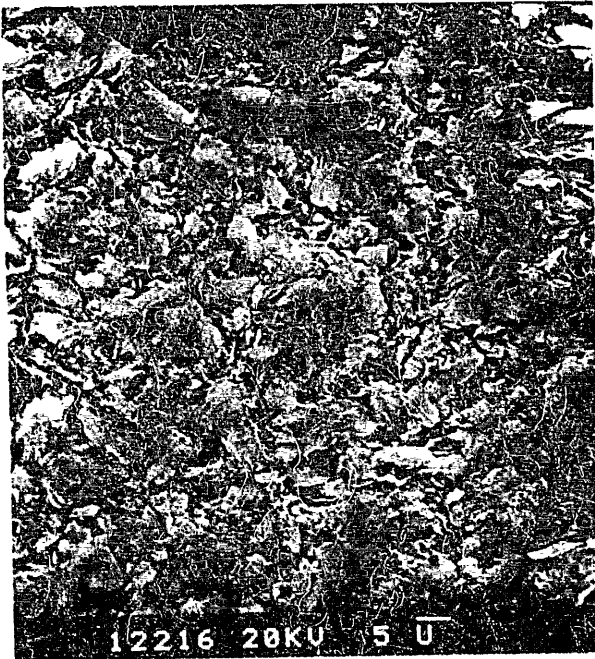
Figure 31a) - d): Union Carbide CGW
pulse length 227 ms, power density 97 MW/m^2



a)



b)



c)



d)

slightly eroded

heavily eroded

Figure 32 a) - d): Toyo Carbon YPD (II)
pulse length 309 ms, power density 96 MW/m^2

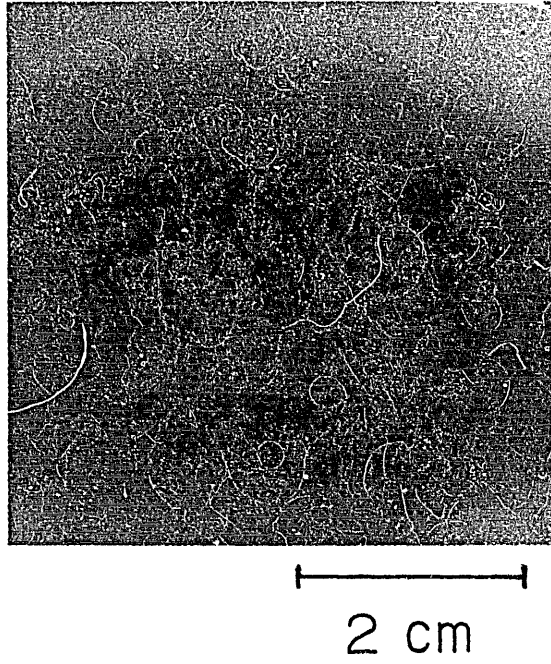
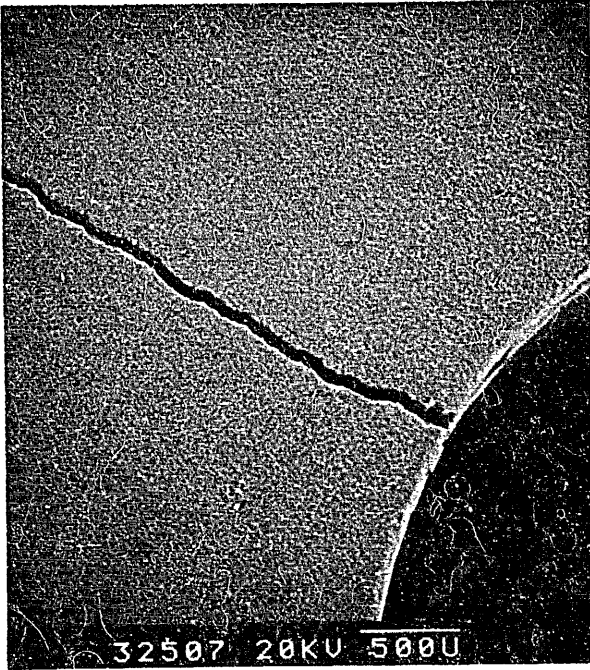
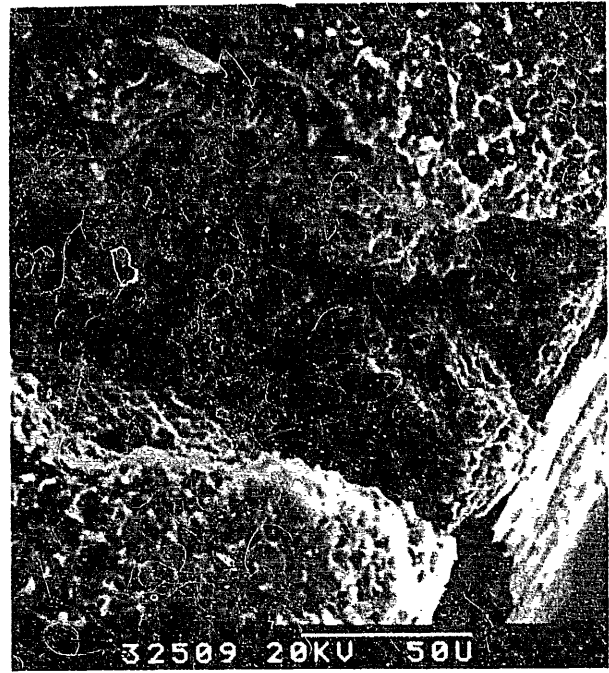


Figure 33 : Poco AXF-5Q, stress concentration sample
pulse length 265 ms, power density 105 MW/m^2



a)



b)



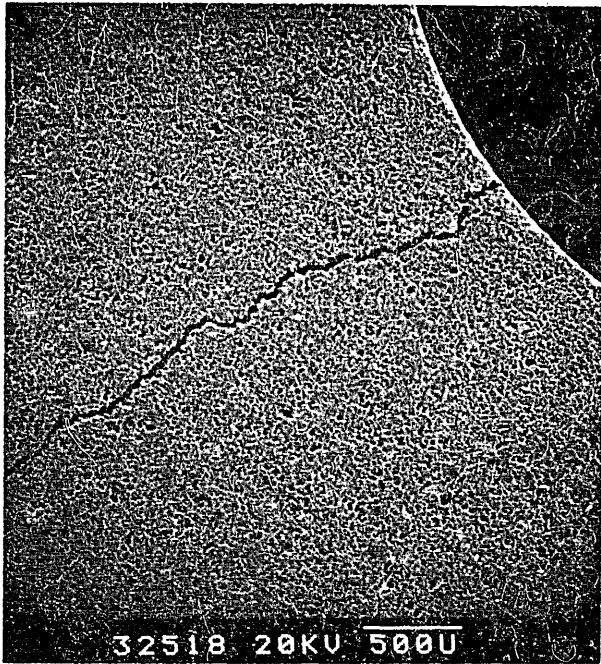
c)

Figure 34 a) - c): Poco AXF-5Q, stress concentration sample
pulse length 265 ms, power density 105 MW/m^2

a): crack propagating from hole edge

b): crack initiation site at hole edge

c): view from hole edge into the depth of the hole



a)



b)



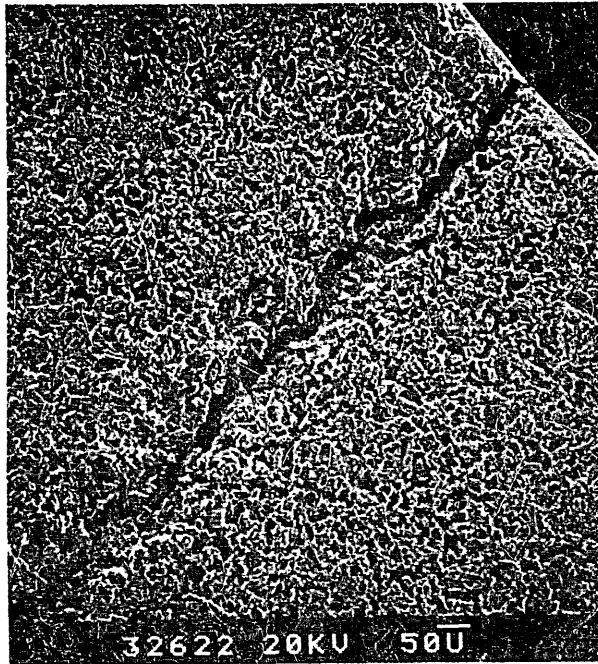
c)

Figure 35 a) - c): Carbone Lorraine CL 5890 PT, stress concentr. sample pulse length 277 ms, power density 105 MW/m^2

a): crack propagating from hole edge

b): crack initiation site at hole edge

c): view from hole edge into the depth of the hole

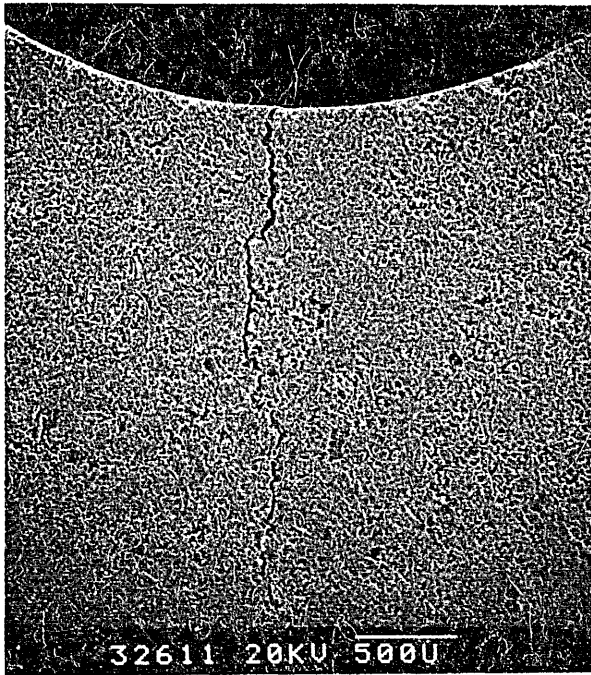


a)



b)

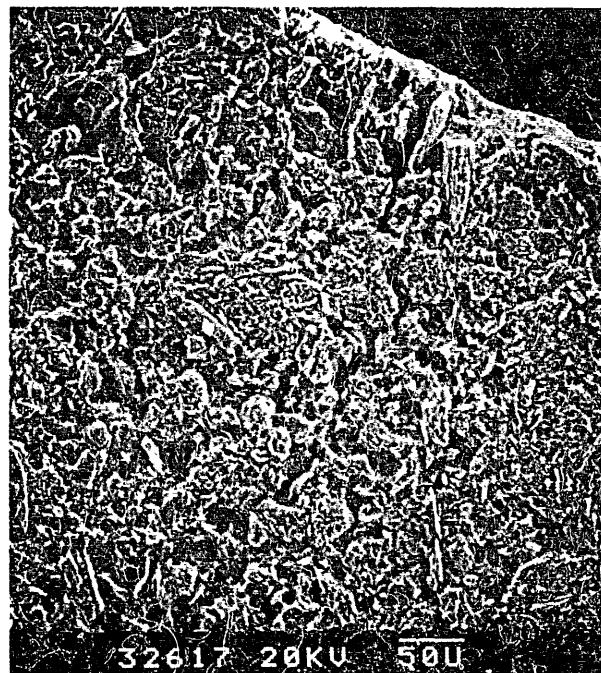
Figure 36 a), b): Ibidem ETP-10, stress concentration sample
pulse length 258 ms, power density 102 MW/m^2
a): crack propagating from hole edge
b): crack tip



a)

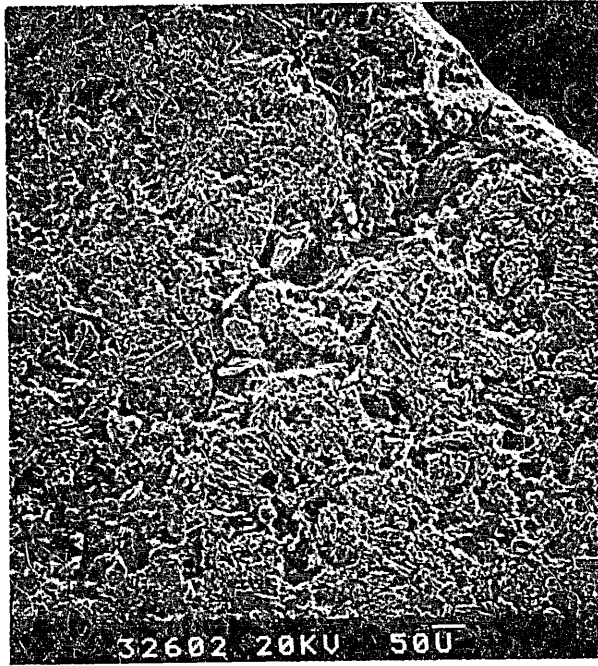


b)

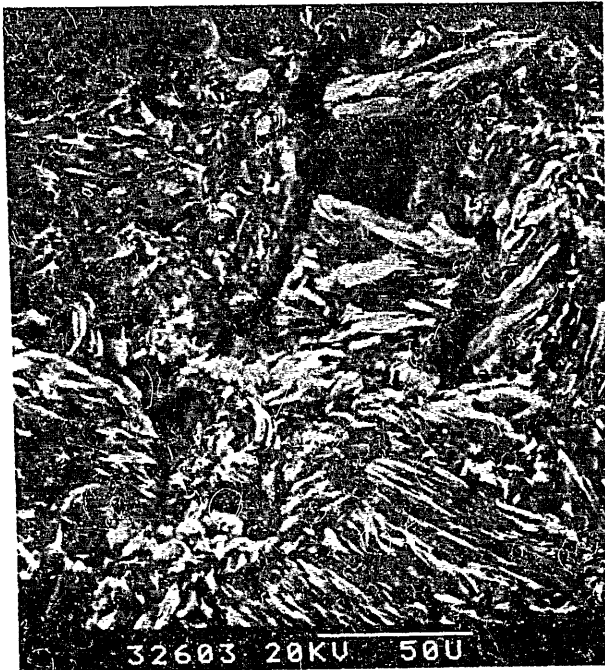


c)

Figure 37 a) - c): Toyo Tanso IG 110, stress concentration sample
pulse length 315 ms, power density 103 MW/m^2
a): crack propagating from hole edge
b): view from hole edge into the depth of the hole
c): microcrack initiated at hole edge



a)



b)



c)

Figure 38 a) - c): Union Carbide ATJ, stress concentration sample
pulse length 271 ms, power density 105 MW/m^2

a): microcrack initiated at hole edge

b): microcrack tip

c): large magnification of the microcrack tip

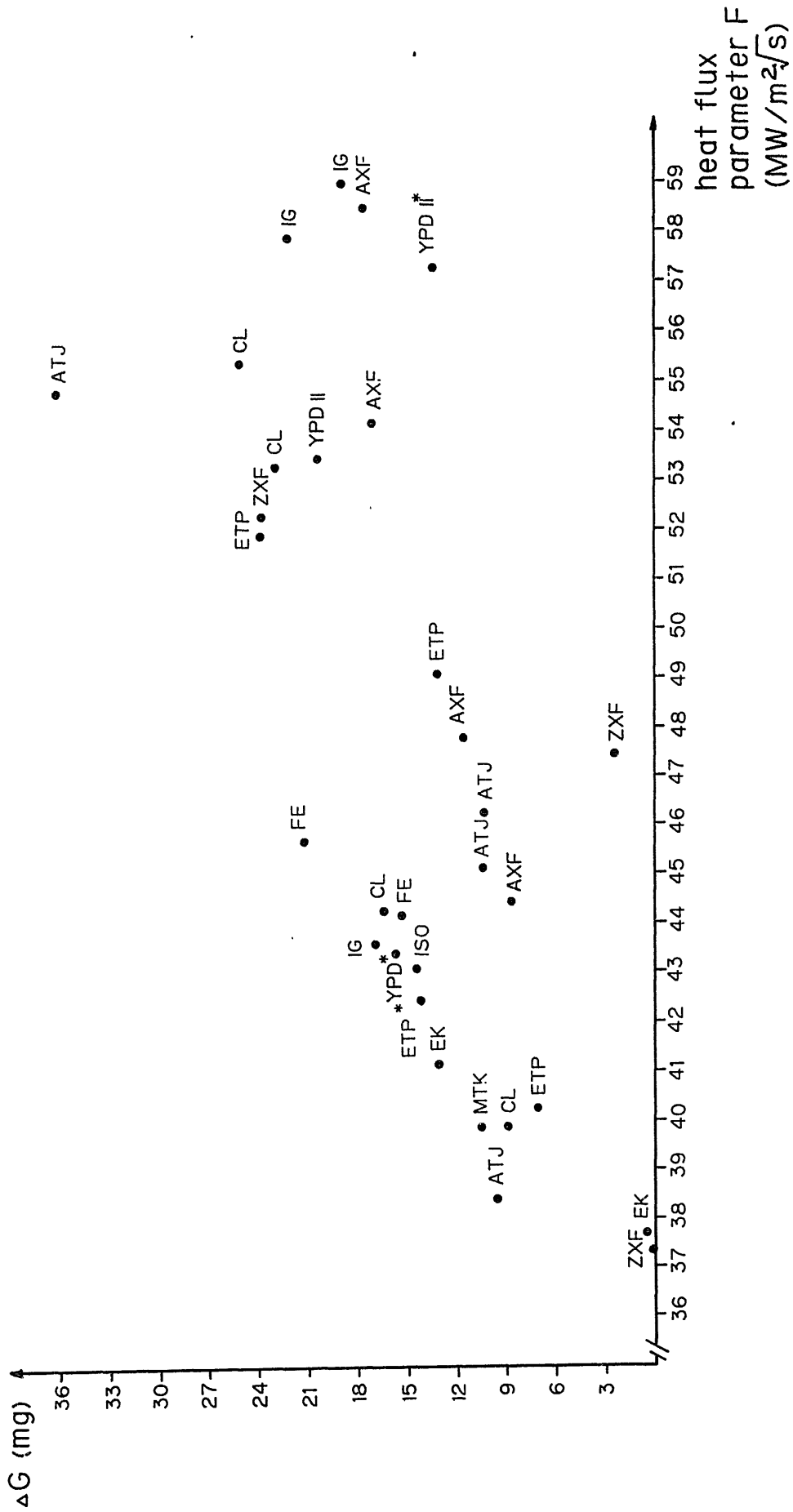


Figure 39: Erosion of graphite samples as function of the incident heat flux, indicated by the heat flux parameter F (cf. 5.3.1)

remark: *: Mean values of samples which were subjected to multiple shots

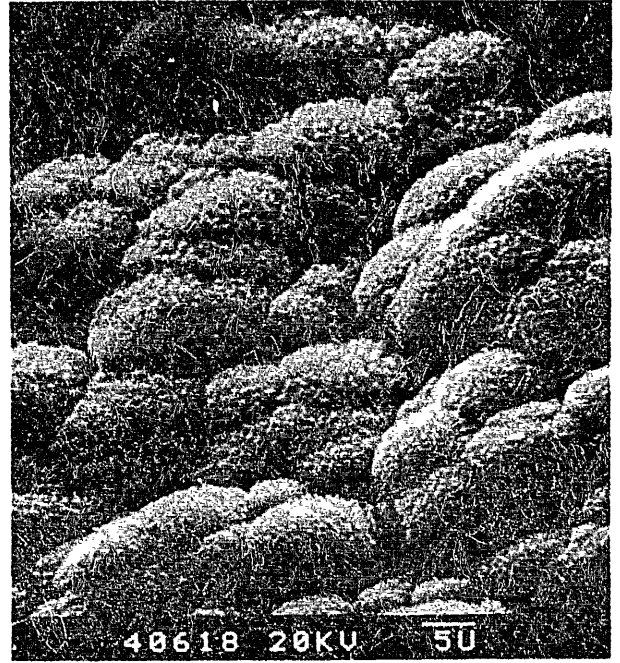
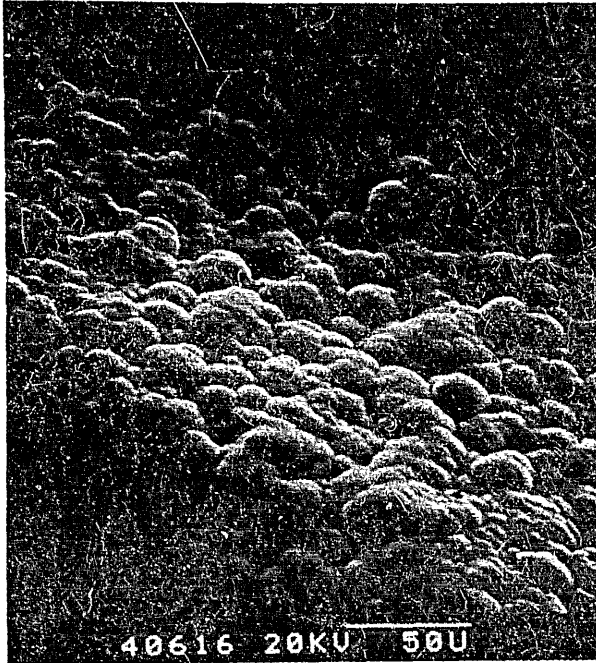
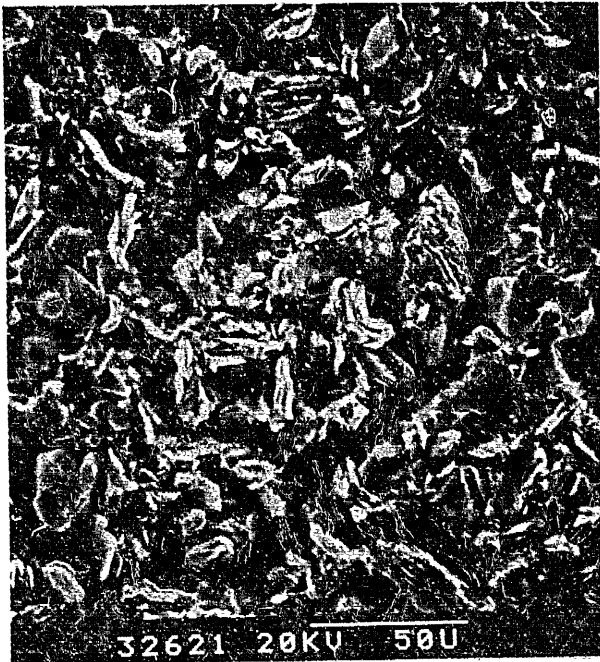


Figure 40: Redeposited carbon accumulated during about 50 pulses on graphite, C-C composite, and pyrocarbon samples; location perpendicular to the exposed surface at sample edge



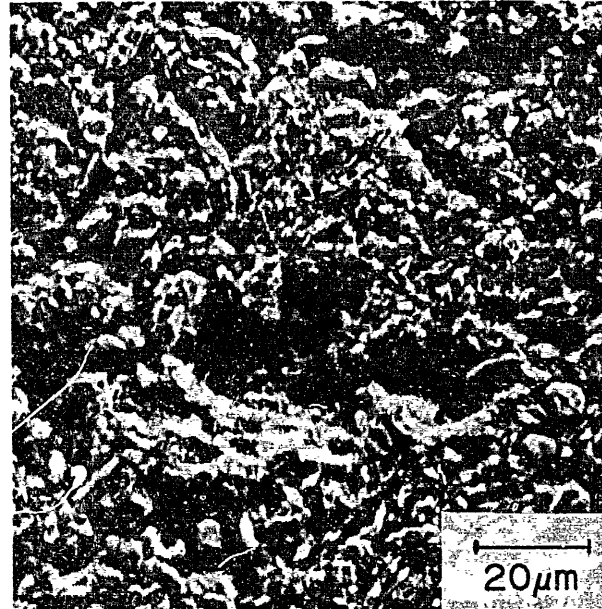
a)



b)



c)



d)

Figure 41 a) - d): Examples for the particle erosion process on graphites
 a): ETP-10, pulse length 258 ms, power density 102 MW/m^2 ;
 loosening of grain cluster on surface
 b): ATJ, pulse length 271 ms, power density 105 MW/m^2 ;
 loosening of grain clusters on surface
 c): CL 5890 PT, pulse length 277 ms, power den. 105 MW/m^2 ;
 loosening of grain cluster on surface
 d): MT 200 K, small size sample from screening test;
 surface void after particle emission

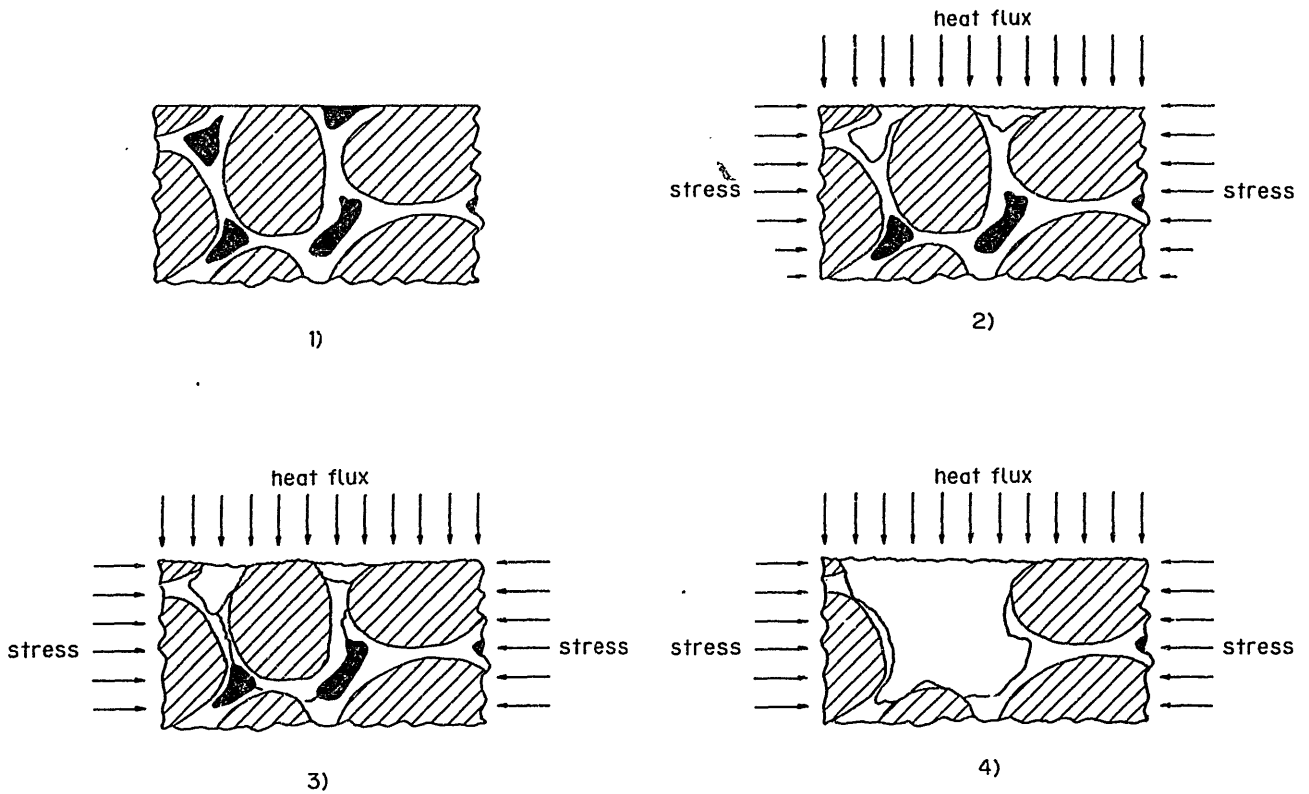
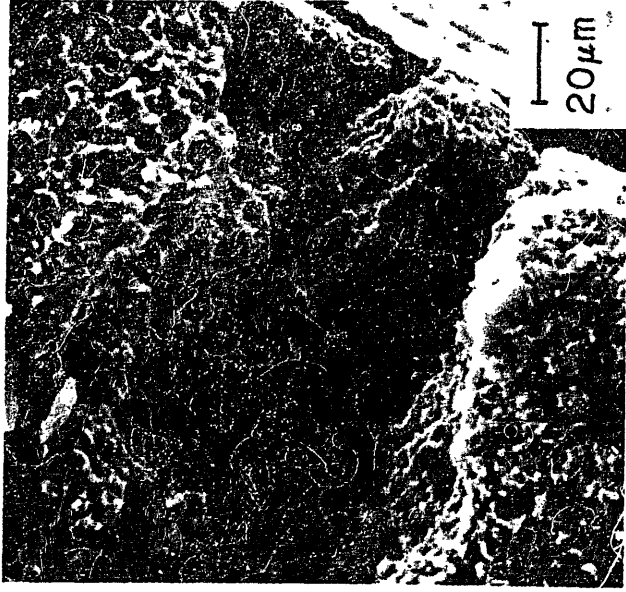


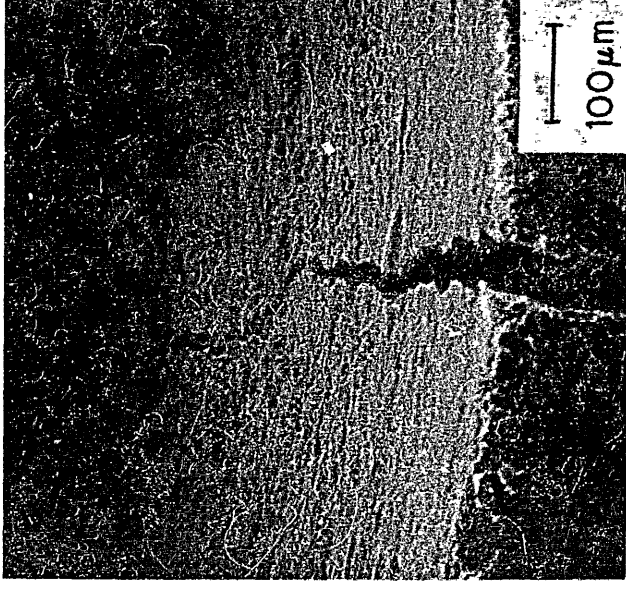
Figure 42 : Schematic model of the particle emission process on graphites under high heat fluxes

- 1) Graphite structure with grains, binder, and pores before the onset of the heat flux
- 2) After the onset of the heat flux the binder phase is preferentially eroded, and compressive stresses develop in the surface layer
- 3) Compressive stresses cause failure of binder bridges
- 4) A particle is emitted which causes a local stress relief



1. Crack initiation:

Driven by compressive surface stresses under high heat loads



2. Crack propagation:

Mainly driven by resultant tensile stresses in the bulk

Figure 43: Two stage model of crack formation on graphites under high heat fluxes

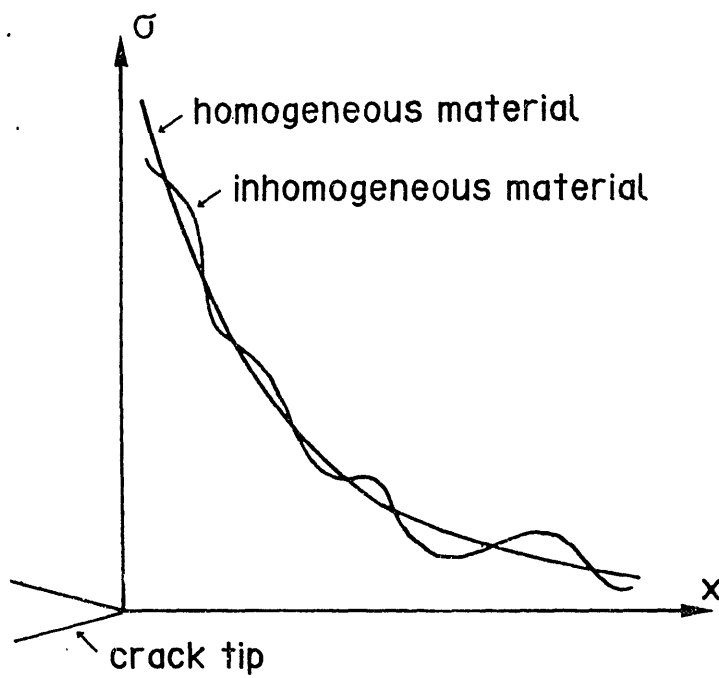
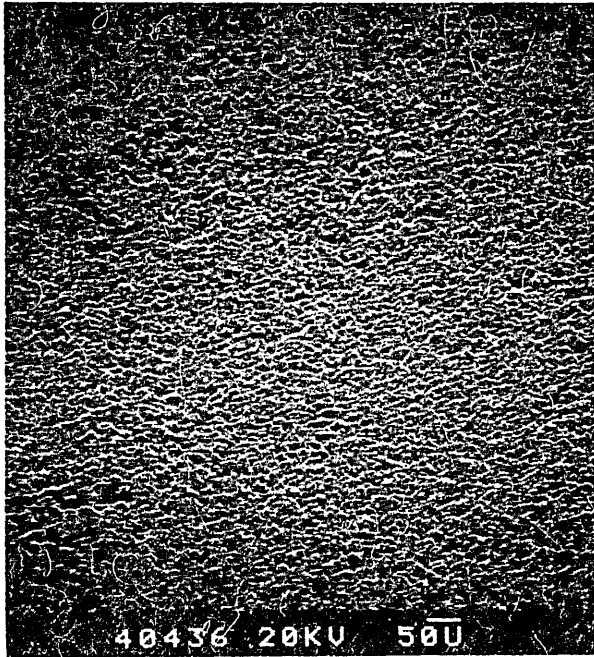
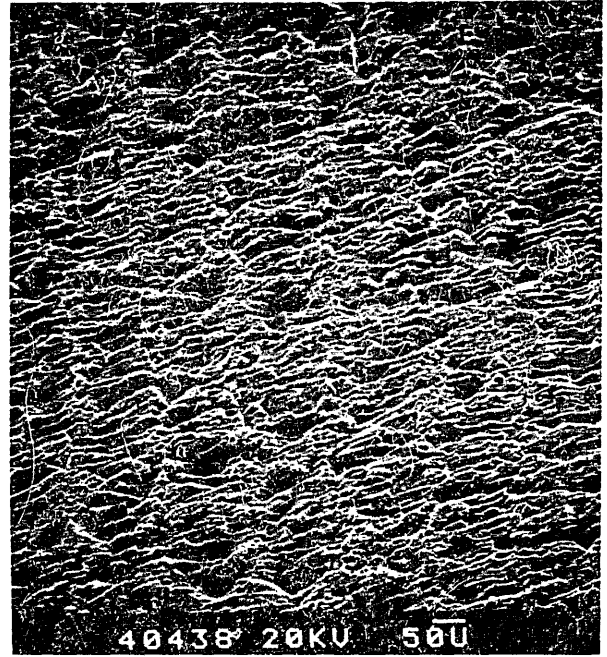


Figure 44: Stress distribution in front of a crack tip in a homogeneous and an inhomogeneous material /114/

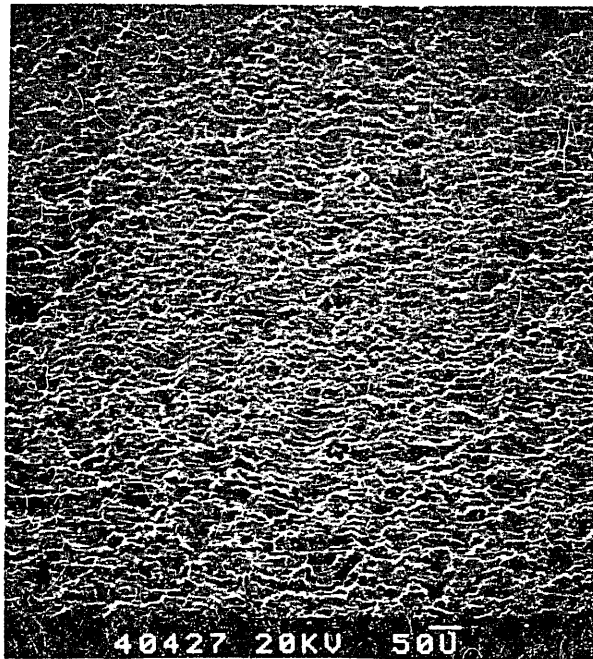


a)



b)

Figure 46 a), b): Pyrocarbon Pfizer Pyroid (II)
a): unirradiated material
b): pulse length 321 ms, power density 102 MW/m^2



a)

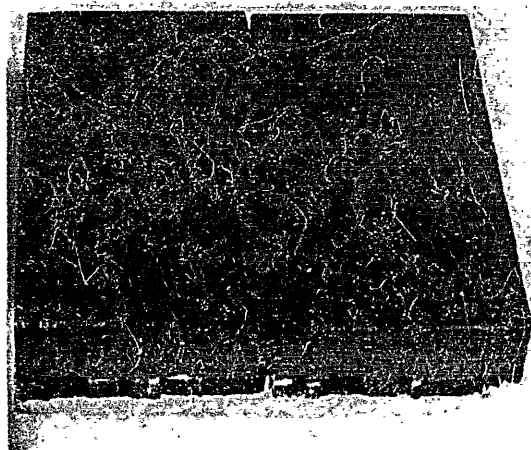


b)

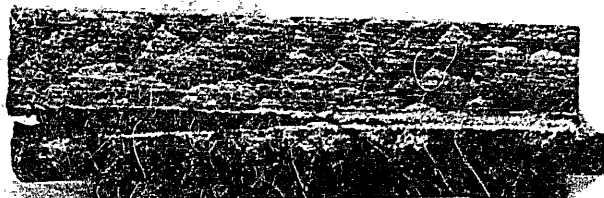


c)

Figure 47 a) - c): Pyrocarbon Carbone Lorraine ("normale") (II)
a): unirradiated material
b), c): pulse length 283 ms, power density 111 MW/m^2
c): large magnification of the crack from b)



2 cm



2 cm



2 cm

Figure 48: Pyrocarbon Pfizer Pyroid brazed to copper base plate
pulse length 416 ms, power density 106 MW/m^2

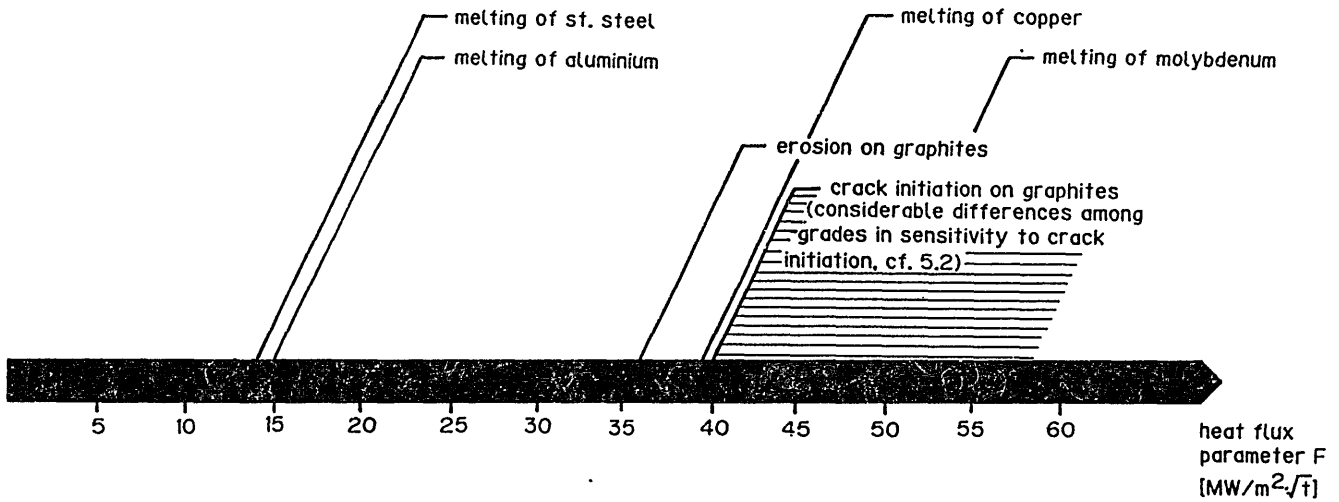


Figure 49: Thresholds for melting of stainless steel, aluminium, copper, and molybdenum and thresholds for erosion and crack initiation on graphites as function of the heat flux parameter F (cf. 5.3.1)

LIST OF IPPJ-AM REPORTS

- IPPJ-AM-1* "Cross Sections for Charge Transfer of Hydrogen Beams in Gases and Vapors in the Energy Range 10 eV–10 keV"
H. Tawara (1977) [Published in Atomic Data and Nuclear Data Tables 22, 491 (1978)]
- IPPJ-AM-2* "Ionization and Excitation of Ions by Electron Impact –Review of Empirical Formulae–"
T. Kato (1977)
- IPPJ-AM-3 "Grotrian Diagrams of Highly Ionized Iron FeVIII-FeXXVI"
K. Mori, M. Otsuka and T. Kato (1977) [Published in Atomic Data and Nuclear Data Tables 23, 196 (1979)]
- IPPJ-AM-4 "Atomic Processes in Hot Plasmas and X-Ray Emission"
T. Kato (1978)
- IPPJ-AM-5* "Charge Transfer between a Proton and a Heavy Metal Atom"
S. Hiraide, Y. Kigoshi and M. Matsuzawa (1978)
- IPPJ-AM-6* "Free-Free Transition in a Plasma –Review of Cross Sections and Spectra–"
T. Kato and H. Narumi (1978)
- IPPJ-AM-7* "Bibliography on Electron Collisions with Atomic Positive Ions: 1940 Through 1977"
K. Takayanagi and T. Iwai (1978)
- IPPJ-AM-8 "Semi-Empirical Cross Sections and Rate Coefficients for Excitation and Ionization by Electron Collision and Photoionization of Helium"
T. Fujimoto (1978)
- IPPJ-AM-9 "Charge Changing Cross Sections for Heavy-Particle Collisions in the Energy Range from 0.1 eV to 10 MeV I. Incidence of He, Li, Be, B and Their Ions"
Kazuhiko Okuno (1978)
- IPPJ-AM-10 "Charge Changing Cross Sections for Heavy-Particle Collisions in the Energy Range from 0.1 eV to 10 MeV II. Incidence of C, N, O and Their Ions"
Kazuhiko Okuno (1978)
- IPPJ-AM-11 "Charge Changing Cross Sections for Heavy-Particle Collisions in the Energy Range from 0.1 eV to 10 MeV III. Incidence of F, Ne, Na and Their Ions"
Kazuhiko Okuno (1978)
- IPPJ-AM-12* "Electron Impact Excitation of Positive Ions Calculated in the Coulomb-Born Approximation –A Data List and Comparative Survey–"
S. Nakazaki and T. Hashino (1979)
- IPPJ-AM-13 "Atomic Processes in Fusion Plasmas – Proceedings of the Nagoya Seminar on Atomic Processes in Fusion Plasmas Sept. 5-7, 1979"
Ed. by Y. Itikawa and T. Kato (1979)
- IPPJ-AM-14 "Energy Dependence of Sputtering Yields of Monatomic Solids"
N. Matsunami, Y. Yamamura, Y. Itikawa, N. Itoh, Y. Kazumata, S. Miyagawa, K. Morita and R. Shimizu (1980)

- IPPJ-AM-15 "Cross Sections for Charge Transfer Collisions Involving Hydrogen Atoms"
Y. Kaneko, T. Arikawa, Y. Itikawa, T. Iwai, T. Kato, M. Matsuzawa, Y. Nakai,
K. Okubo, H. Ryufuku, H. Tawara and T. Watanabe (1980)
- IPPJ-AM-16 "Two-Centre Coulomb Phaseshifts and Radial Functions"
H. Nakamura and H. Takagi (1980)
- IPPJ-AM-17 "Empirical Formulas for Ionization Cross Section of Atomic Ions for Elec-
tron Collisions –Critical Review with Compilation of Experimental Data–"
Y. Itikawa and T. Kato (1981)
- IPPJ-AM-18 "Data on the Backscattering Coefficients of Light Ions from Solids"
T. Tabata, R. Ito, Y. Itikawa, N. Itoh and K. Morita (1981) [Published in
Atomic Data and Nuclear Data Tables 28, 493 (1983)]
- IPPJ-AM-19 "Recommended Values of Transport Cross Sections for Elastic Collision and
Total Collision Cross Section for Electrons in Atomic and Molecular Gases"
M. Hayashi (1981)
- IPPJ-AM-20 "Electron Capture and Loss Cross Sections for Collisions between Heavy
Ions and Hydrogen Molecules"
Y. Kaneko, Y. Itikawa, T. Iwai, T. Kato, Y. Nakai, K. Okuno and H. Tawara
(1981)
- IPPJ-AM-21 "Surface Data for Fusion Devices – Proceedings of the U.S.–Japan Work-
shop on Surface Data Review Dec. 14-18, 1981"
Ed. by N. Itoh and E.W. Thomas (1982)
- IPPJ-AM-22 "Desorption and Related Phenomena Relevant to Fusion Devices"
Ed. by A. Koma (1982)
- IPPJ-AM-23 "Dielectronic Recombination of Hydrogenic Ions"
T. Fujimoto, T. Kato and Y. Nakamura (1982)
- IPPJ-AM-24 "Bibliography on Electron Collisions with Atomic Positive Ions: 1978
Through 1982 (Supplement to IPPJ-AM-7)"
Y. Itikawa (1982) [Published in Atomic Data and Nuclear Data Tables 31,
215 (1984)]
- IPPJ-AM-25 "Bibliography on Ionization and Charge Transfer Processes in Ion-Ion
Collision"
H. Tawara (1983)
- IPPJ-AM-26 "Angular Dependence of Sputtering Yields of Monatomic Solids"
Y. Yamamura, Y. Itikawa and N. Itoh (1983)
- IPPJ-AM-27 "Recommended Data on Excitation of Carbon and Oxygen Ions by Electron
Collisions"
Y. Itikawa, S. Hara, T. Kato, S. Nakazaki, M.S. Pindzola and D.H. Crandall
(1983) [Published in Atomic Data and Nuclear Data Tables 33, 149 (1985)]
- IPPJ-AM-28 "Electron Capture and Loss Cross Sections for Collisions Between Heavy
Ions and Hydrogen Molecules (Up-dated version of IPPJ-AM-20)
H. Tawara, T. Kato and Y. Nakai (1983) [Published in Atomic Data and
Nuclear Data Tables 32, 235 (1985)]

- IPPJ-AM-29 “Bibliography on Atomic Processes in Hot Dense Plasmas”
T. Kato, J. Hama, T. Kagawa, S. Karashima, N. Miyanaga, H. Tawara, N. Yamaguchi, K. Yamamoto and K. Yonei (1983)
- IPPJ-AM-30 “Cross Sections for Charge Transfers of Highly Ionized Ions in Hydrogen Atoms (Up-dated version of IPPJ-AM-15)”
H. Tawara, T. Kato and Y. Nakai (1983) [Published in Atomic Data and Nuclear Data Tables 32, 235 (1985)]
- IPPJ-AM-31 “Atomic Processes in Hot Dense Plasmas”
T. Kagawa, T. Kato, T. Watanabe and S. Karashima (1983)
- IPPJ-AM-32 “Energy Dependence of the Yields of Ion-Induced Sputtering of Monatomic Solids”
N. Matsunami, Y. Yamamura, Y. Itikawa, N. Itoh, Y. Kazumata, S. Miyagawa, K. Morita, R. Shimizu and H. Tawara (1983) [Published in Atomic Data and Nuclear Data Tables 31, 1 (1984)]
- IPPJ-AM-33 “Proceedings on Symposium on Atomic Collision Data for Diagnostics and Modelling of Fusion Plasmas, Aug. 29 – 30, 1983”
Ed. by H. Tawara (1983)
- IPPJ-AM-34 “Dependence of the Backscattering Coefficients of Light Ions upon Angle of Incidence”
T. Tabata, R. Ito, Y. Itikawa, N. Itoh, K. Morita and H. Tawara (1984)
- IPPJ-AM-35 “Proceedings of Workshop on Synergistic Effects in Surface Phenomena Related to Plasma-Wall Interactions, May 21 – 23, 1984”
Ed. by N. Itoh, K. Kamada and H. Tawara (1984) [Published in Radiation Effects 89, 1 (1985)]
- IPPJ-AM-36 “Equilibrium Charge State Distributions of Ions ($Z_1 \geq 4$) after Passage through Foils – Compilation of Data after 1972”
K. Shima, T. Mikumo and H. Tawara (1985) [Published in Atomic Data and Nuclear Data Tables 34, 357 (1986)]
- IPPJ-AM-37 “Ionization Cross Sections of Atoms and Ions by Electron Impact”
H. Tawara, T. Kato and M. Ohnishi (1985)
- IPPJ-AM-38 “Rate Coefficients for the Electron-Impact Excitations of C-like Ions”
Y. Itikawa (1985)
- IPPJ-AM-39 “Proceedings of the Japan-U.S. Workshop on Impurity and Particle Control, Theory and Modeling, Mar. 12 – 16, 1984”
Ed. by T. Kawamura (1985)
- IPPJ-AM-40 “Low-Energy Sputterings with the Monte Carlo Program ACAT”
Y. Yamamura and Y. Mizuno (1985)
- IPPJ-AM-41 “Data on the Backscattering Coefficients of Light Ions from Solids (a Revision)”
R. Ito, T. Tabata, N. Itoh, K. Morita, T. Kato and H. Tawara (1985)

- IPPJ-AM-42 "Stopping Power Theories for Charged Particles in Inertial Confinement Fusion Plasmas (Emphasis on Hot and Dense Matters)"
S. Karashima, T. Watanabe, T. Kato and H. Tawara (1985)
- IPPJ-AM-43 "The Collected Papers of Nice Project/IPP, Nagoya"
Ed. by H. Tawara (1985)
- IPPJ-AM-44 "Tokamak Plasma Modelling and Atomic Processes"
Ed. by T. Kawamura (1986)
- IPPJ-AM-45 Bibliography of Electron Transfer in Ion-Atom Collisions
H. Tawara, N. Shimakura, N. Toshima and T. Watanabe (1986)
- IPPJ-AM-46 "Atomic Data Involving Hydrogens Relevant to Edge Plasmas"
H. Tawara, Y. Itikawa, Y. Itoh, T. Kato, H. Nishimura, S. Ohtani, H. Takagi, K. Takayanagi and M. Yoshino (1986)
- IPPJ-AM-47 "Resonance Effects in Electron-Ion Collisions"
Ed. by H. Tawara and G. H. Dunn (1986)
- IPPJ-AM-48 "Dynamic Processes of Highly Charged Ions (Proceedings)"
Ed. by Y. Kanai and S. Ohtani (1986)
- IPPJ-AM-49 "Wavelengths of K X-Rays of Iron Ions"
T. Kato, S. Morita and H. Tawara (1987)
- IPPJ-AM-50 "Proceedings of the Japan-U.S. Workshop P-92 on Plasma Material Interaction/High Heat Flux Data Needs for the Next Step Ignition and Steady State Devices, Jan. 26 – 30, 1987"
Ed. by A. Miyahara and K. L. Wilson (1987)
- IPPJ-AM-51 "High Heat Flux Experiments on C-C Composite Materials by Hydrogen Beam at the 10MW Neutral Beam Injection Test Stand of the IPP Nagoya"
H. Bolt, A. Miyahara, T. Kuroda, O. Kaneko, Y. Kubota, Y. Oka and K. Sakurai (1987)
- IPPJ-AM-52 "Energy Dependence of Ion-Induced Sputtering Yields of Monatomic Solids in the Low Energy Region"
N. Matsunami, Y. Yamamura, N. Itoh, H. Tawara and T. Kawamura (1987)
- IPPJ-AM-53 "Data Base on the High Heat Flux Behaviour of Metals and Carbon Materials for Plasma Facing Components – Experiments at the 10 MW Neutral Beam Injection Test Stand of the IPP Nagoya"
H. Bolt, C. D. Croessmann, A. Miyahara, T. Kuroda and Y. Oka (1987)

Available upon request to Research Information Center, Institute of Plasma Physics, Nagoya University, Nagoya 464, Japan, except for the reports noted with*.